

184-31464

NASA CR-174670

cy 30

REFLECTOR ANTENNAS WITH LOW SIDELOBES,  
LOW CROSS POLARIZATION, AND  
HIGH APERTURE EFFICIENCY

by

I. M. Faigen, C. F. Reichert,  
C. J. Sletten, and R. A. Shore

CHU ASSOCIATES, INC. & SOLAR ENERGY TECHNOLOGY, INC.

Prepared for

NATIONAL AERONAUTICS AND SPACE ADMINISTRATION

NASA Lewis Research Center

Contract NAS 3-22343

**Chu**

|   |  |  |  |  |            |
|---|--|--|--|--|------------|
| 1. Report No.<br>NASA CR174670  |  | 2. Government Accession No.                          |  | 3. Recipient's Catalog No.                                 |            |
| 4. Title and Subtitle<br>Reflector Antennas with Low Sidelobes, Low Cross Polarization,<br>and High Aperture Efficiency   |  |  |  | 5. Report Date   |            |
|   |  |  |  | 6. Performing Organization Code                            |            |
| 7. Author(s)<br>I. M. Faigen, Charles F. Reichert, C. J. Sletten, and R.A. Shore  |  |  |  | 8. Performing Organization Report No.                      |            |
| 9. Performing Organization Name and Address   |  |  |  | 10. Work Unit No.  |            |
|   |  |  |  | 11. Contract or Grant No.<br>NAS3-22343                    |            |
| 12. Sponsoring Agency Name and Address<br>National Aeronautics & Space Administration<br>Washington, DC 20546   |  |  |  | 13. Type of Report and Period Covered<br>Contractor Report |            |
|   |  |  |  | 14. Sponsoring Agency Code                                 |            |
| 15. Supplementary Notes<br>Technical Manager, Jerry Smetana, Space Communications Division<br>NASA Lewis Research Center, Cleveland, Ohio 44135   |  |  |  |  |            |
| 16. Abstract<br><br>A satellite communication antenna design is described for an offset fed 2.44 meter diameter paraboloid operating in the 12 GHz band to produce -30 db to -40 db sidelobe levels with aperture efficiencies of approximately 75%. Using an optimally titled dual reflector configuration, a shaped Gregorian subreflector is fed by a corrugated conical horn to realize low cross polarization and wide pattern and impedance bandwidth characteristics. Report presents new techniques for wide angle scanning of multibeams by varying horn locations, for shaping subreflectors to compensate for horn feed aberrations, and for computing conical horn near-field and antenna far-field patterns. |  |  |  |  |            |
| 17. Key Words (Suggested by Author(s))<br>offset dual reflectors, corrugated conical<br>horns, focal surfaces, diffraction patterns   |  |  | 18. Distribution Statement<br><br>Unclassified-Unlimited |  |            |
| 19. Security Classif. (of this report)<br>Unclassified  |  | 20. Security Classif. (of this page)<br>Unclassified |  | 21. No. of Pages<br>115                                    | 22. Price* |

\* For sale by the National Technical Information Service, Springfield, Virginia 22161

REFLECTOR ANTENNAS WITH LOW SIDELOBES,  
LOW CROSS POLARIZATION, AND  
HIGH APERTURE EFFICIENCY

Submitted to

NASA Lewis Research Center  
21000 Brookpark Road  
Cleveland, Ohio 44135

Under Contract NAS 3-22343

March 1984

CHU ASSOCIATES, INC.  
Littleton, Massachusetts, 01460

## TABLE OF CONTENTS

1. SUMMARY
2. INTRODUCTION
3. ANALYSIS
  - 3.1 Choosing the Components
  - 3.2 Configuring the Dual Reflector Antenna
  - 3.3 Antenna Sidelobe Levels vs. Aperture Efficiencies
  - 3.4 Analysis and Computation of Corrugated Conical Horn Near Zone Patterns
  - 3.5 Design of the Corrugated Conical Horn
  - 3.6 Theoretical Patterns of Antenna Fed by the Corrugated Conical Horn
  - 3.7 Correcting for Center-of-Phase Change on Corrugated Conical Horn
  - 3.8 The Subreflector Shaping Technique to Correct for Horn Phase Errors
  - 3.9 Finding the Best Focal Curves
  - 3.10 Effect of Near-Zone Diffraction of the 2.44 Meter Aperture
4. DESIGN AND FABRICATION
  - 4.1 Geometrical Configuration
  - 4.2 Mechanical Design
  - 4.3 Tooling and Fabrication
  - 4.4 Assembly Procedure
5. RESULTS AND CONCLUSIONS
6. REFERENCES

## LIST OF FIGURES

| <u>FIGURE NO.</u> | <u>DESCRIPTION</u>  |
|-------------------|---|
| 3.1               | Offset Dual Reflector Geometry for Reference Surfaces   |
| 3.2               | Cross Sectional View of Model Antenna   |
| 3.3               | Front View of Model Antenna   |
| 3.4               | Design Parameter Tradeoffs  |
| 3.5               | Kouznetsov Low Sidelobe Circular Aperture Illumination  |
| 3.6               | Minimum Spreading Factor Functions  |
| 3.7               | Idealized Horn Geometry   |
| 3.8               | Amplitude Function of 68.58 cms (27") 12° Corrugated Horn   |
| 3.9               | Conical Horn Phase Curve for 76.2 cms Horn  |
| 3.10              | Cross Sectional View of Corrugated Conical Horn   |
| 3.11              | Illumination of Circular Aperture by 76.2 cms Corrugated Horn   |
| 3.12              | Diffraction Patterns of Circular Aperture Illuminated by a 76.2 cm, 12° Corrugated Horn - No Phase Error      |
| 3.13              | Diffraction Pattern of Circular Aperture Illuminated by a 76.2 cm, 12° Corrugated Horn - Phase Error Included |
| 3.14              | Analytical Refocusing to Correct Horn Phase   |
| 3.15              | Correcting Horn Edge Rays by Increasing Eccentricity  |
| 3.16              | Template Contour (y-cut) Through Middle of Shaped Subreflector  |
| 3.17              | Front View of Subreflector  |
| 3.18              | Best Elevation Plane Focal Curve  |
| 3.19A             | Traces of the Dish Rim Rays on the "Screen" for Azimuth Scan at 3°  |

LIST OF FIGURES - continued...

- 3.19B Traces of the Dish Rim Rays on the "Screen" for Elevation Scan at  $3^\circ$
- 3.19C Traces of the Dish Rim Rays on the "Screen" for Beam at Elevation Angle  $2^\circ$ , Azimuth Angle  $2^\circ$
- 3.20 X-Y Plot of Focal Surfaces
- 3.21 A "Footprint" of Dish Edge on Ellipsoid Surface
- 3.22 Focal Region Comparisons, Elevation Scan
- 3.23 Coordinate System for Circular Aperture Diffraction Patterns
- 3.24 Diffraction Pattern Scanned  $3^\circ$  in Azimuth Focused at Best Azimuth Focus
- 3.25 Diffraction Pattern Scanned  $3^\circ$  in Elevation Focused at Best Elevation Focus
- 3.26 Coordinate Systems Used in Describing Dish Near-Field Diffraction Patterns (X-Axis Points out of Plane of the Paper)
- 3.27A Amplitude and Phase of Focal Region Tangential Electric Field of a Tapered Plane Wave Scattered from a Paraboloidal Aperture
- 4.1 Positioning Schematic Improved SATCOM Antenna
- 4.2 SATCOM Antenna Assembly
- 4.3 Reflector Assembly, SATCOM Antenna
- 4.4 Subreflector Assembly
- 4.5 Feed Horn External Configuration
- 4.6A Feed Support Device
- 4.6B Feed Support Device
- 4.7A Platform
- 4.7B Platform

LIST OF FIGURES - Continued...

|      |                          |
|------|--------------------------|
| 4.8  | Reflector Mold           |
| 4.9A | Sweep Arm                |
| 4.9B | Sweep Arm                |
| 4.10 | Outboard Support Mold    |
| 4.11 | Kingpost Mold            |
| 4.12 | Subreflector Mold        |
| 4.13 | Horn Positioning Fixture |

## LIST OF TABLES

| <u>TABLE NO.</u> | <u>DESCRIPTION</u>  |
|------------------|---|
| 3.1              | Aperture Efficiency, Half-Power Beamwidth and Sidelobes for Different Aperture Illumination Functions (Key to Illumination Functions) |
| 5.1              | Dimensions - Corrugated Conical Horn  |
| 9.1              | Focal Plane Data  |

## 1.0 SUMMARY

Ideal paraboloidal dish illuminations for -30 to -40 db sidelobe levels with 70 to 80% aperture efficiencies can be realized using either Cassegrain or ellipsoidal offset subreflectors fed by conical corrugated horns. All antennas are optimally tilted by the Japanese criteria for symmetric beams, low cross polarization, and no aperture blocking. New techniques for computing the horn near-field patterns on the subreflectors and for correcting the phase center errors of the horn pattern by shaping the subreflector surface are reported.

For generating or scanning multibeam by horn motion the best focal surfaces of the offset dual reflector systems are computed for best azimuth, best elevation and best compromise patterns. These dual reflector systems with high magnifications can produce multibeam with -30 db sidelobe levels over more than  $+ 8^\circ$  beamwidth intervals. Techniques for computing the diffraction patterns for scanned beams are described. Also, the effects of dish aperture diffraction on pattern bandwidth are presented.

A model antenna consisting of reflector, shaped subreflector and corrugated feed horn was designed. The reflector is a 2.44 meter circular aperture operating in the 12 GHz satellite communications band. A  $12^\circ$  conical corrugated horn and a shaped Gregorian subreflector about 76 cms in diameter, which it is to illuminate, were designed and built.

## 2.0 INTRODUCTION

The stringent specifications of this contract were written to extend the state-of-the art of antenna design for satellite communications by improving sidelobe and cross polarization performance without sacrificing aperture efficiency for multibeam, frequency reuse applications. Based on approaches outlined in the original proposal, the job was to derive a solid analytical base for such performance using optimized dual reflector antennas fed by conical corrugated horns and to build a prototype antenna to verify the analysis.

The analytical task which was performed by SET, Inc. brings to bear current world design knowledge on reflector antenna systems and includes many original analytic contributions for shaping subreflector surfaces, determining the antenna focal fields for multibeam generation, and by complex diffraction analysis, computing the theoretical antenna patterns and performance expected from the design. The analytic task also provides the necessary design and dimension information for construction of the conical corrugated horn and the reflector surfaces. The conical horn, the shaped Gregorian subreflector and the 2.44 meter offset paraboloid must be carefully aligned and structurally mounted without aperture blocking providing focusing variations for the radiation pattern measurements.

The contract's performance specifications set requirement goals of -30 db for first and second sidelobe, and -40 db for third and higher sidelobe levels with an attendant 80% aperture efficiency. This is the most difficult specification to achieve. As is shown by a comprehensive analytical study, this sidelobe level vs. aperture efficiency specification is at the edge of the theoretically possible for circular aperture reflectors. The cross polarization isolation specification of 30 db means that the offset reflector geometry must be selected using Japanese criteria<sup>(1,2)</sup> to avoid introducing geometrically caused cross polarization and that the conical corrugated horn must also be free of cross polarization. In addition, the illuminated portion of the subreflector must be at least 15 wavelengths in diameter to avoid increasing cross polarization levels due to diffraction<sup>(3)</sup>.

The beam scanning requirement of  $3^\circ$  from boresight means that the wide angle scanning characteristics of the dual reflector antenna must be investigated. Interest in main reflector diameters in the range of 1 to 4.5 meters is expressed in the work statement. A reflector diameter of 2.4384 meters (8 feet) was chosen. For larger dishes the cost of construction and diffraction computations becomes expensive. For smaller dishes the  $15\lambda$  diameter subreflector is relatively large in comparison with the diameter of the main reflector.

A general bandwidth specification of 1% is given in the work statement. However, each frequency band of interest in the specification requires 500 MHz bandwidths which is a 4.2% bandwidth for the 12 GHz band emphasized for the project. Actually, the baseline antenna should work quite well over both the 11.7 to 12.2 GHz reception band and the 14 to 14.5 GHz transmission band for ground station operations which is a bandwidth of approximately 21%. The optical design techniques used in the reflector configuration and subreflector shaping are very broadband. Also, the conical corrugated horn pattern and impedance bandwidths are also quite wide although higher modes can exist in circular waveguide feeding the horn in the 14 to 14.5 GHz band. However, main reflector diffraction effects are quite narrow band and sidelobe levels are expected to vary somewhat outside the specified 12 GHz frequency band. The antenna beamwidths depend on frequency being about  $\theta_{1/2} \text{ pwr.} = 1/28 \lambda / D$  in radians where  $\lambda$  is wavelength and D is the diameter of the main reflector. Also, antenna gain is about  $G = .8 (2\pi R/\lambda)^2$  where R is radius of dish aperture. The 2.44 meter (8 feet) diameter base line antenna is designed for best performance in the 11.7 to 12.2 GHz band centered on 12 GHz.

All elements of the antenna system were mechanically designed in order to provide a high tolerance antenna system capable of providing the vernier adjustments necessary for a research and development effort and of yielding the desired theoretical performance of Section 3. The major elements of the antenna system consist of the paraboloidal reflector, the shaped Gregorian subreflector and the  $12^\circ$  corrugated feed horn. These major subassemblies are mounted on a platform specifically designed to maintain the geometrical relationships required for the desired antenna performance. A feed support device permits angular and axial motion of the feed horn into the shaped subreflector which is held fixed in its' desired attitude at the further end of the platform.

As part of NASA contract NAS 3-22343, the corrugated feed horn, subreflector, and rough mold for the paraboloidal reflector were constructed. The subreflector was verified dimensionally to assure that tolerances were maintained. The feed horn was phase and amplitude tested in order to obtain the data necessary for shaping the Gregorian subreflector and mathematically designing the balance of the antenna system.

### 3.0 ANALYSIS AND ANTENNA PARAMETER COMPUTATIONS

The antenna configuration chosen was an offset fed dual reflector system. The advantages of this reflector geometry, when Japanese optimized tilt relations are: 1) zero blocking of the dish aperture by feed or support structures to prevent increased sidelobes due to blockage, 2) very low reflector or subreflector caused cross polarization levels, 3) symmetric aperture illumination giving symmetrical beam and sidelobe patterns when a  $HE_{11}$  mode conical corrugated horn is used as exciter of the subreflector, and 4) no VSWR increases at the horn input due to subreflector or main reflector reflections. Based on reasons to be explained more fully later, it was decided to construct a dual reflector antenna of the Gregorian type fed by a conical corrugated horn whose general characteristics are reported by Clarricoats<sup>(5)</sup>. Figure 3.1 illustrates in cross section, optimized offset dual reflector antenna geometry.

Given these choices, the analytical and design tasks were to configure and shape as necessary, the dual reflector surfaces, design the conical corrugated horn and to compute the near field radiation patterns of the conical horn on the subreflector and the far-field pattern of the main reflector for the scanning intervals of interest.

### 3.2 Configuring the Dual Reflector Antenna

References 1) and 2) report antenna pattern and polarization results of Japanese work on optimally tilted dual reflector antennas. References 4) and 5) provide a useful set of design equations for dual reflector systems used in a new subreflector synthesis technique. The actual proof of the optimum orientation of a conic section subreflector confocal with an offset paraboloid section is lengthy but the main design equations are given here and in Reference 5). Figure 3.2 provides

a cross sectional view (y-z plane) of the demonstration model antenna. Fig. 3.3 shows a front view of the demonstration model antenna.

The design procedure for configuring a dual reflector antenna using the Japanese criteria begins by selecting the diameter of the circular main paraboloidal section and its offset relative to the paraboloid vertex. The dish diameter,  $D$ , and wavelength,  $\lambda$ , establish approximately the antenna gain and beamwidth. Ideally we would like to obtain

$$BW_{\frac{1}{2} \text{ pwr}} \cong 1.2 \lambda/D \text{ radians}$$

and

$$G \cong 0.8 \left( \frac{2\pi R}{\lambda} \right)^2$$

which conditions for -30 dB to -40 dB sidelobe levels are at the border of realizability with perfect antenna design (see section 3.0).

We will follow Japanese analytic procedures to optimized orientation of horn and subreflector to the main reflector and use the coordinate system shown in Fig. 3.1. The 244 cm diameter paraboloidal section is offset such that its (see Fig. 3.2) center point is 157.48 cms (62") above the z-axis and the lower rim of the dish 35.56 cms (14") above the z-axis. This lifting of the dish is to allow the subreflector to be large enough to scan  $3^\circ$  in elevation without aperture blocking and to also provide room for the horn apex and holder for elevation angle acanning.

For wide angle scanning the focal length,  $f$ , should be as large as practical given that increasing the length of the antenna structure (by increasing  $f$ ) generally increases its cost. A value of focal length,  $f = 177.8$  cms (70 inches), was selected.

Either a Cassegrain (hyperboloid) or Gregorian (ellipsoid) subreflector surface can be used. From a geometrical optics point of view they give identical performance. However, mechanically the Cassegrain design results in a taller antenna with larger offset and generally a tighter turning radius for azimuth plane scanning by antenna rotation. When diffraction is considered the ellipsoid design offers several advantages. The concave shaped subreflector more nearly approximates the spherical wave radiated by the conical horn. A more symmetrical pattern (equal E and H plane patterns) is, therefore, to be expected because the amplitude of the near-field horn pattern varies in a complicated manner with distance between the horn and the subreflector surface. Of more importance, however, is the influence of the shifting center-of-phase of the horn pattern toward the subreflector with increasing horn pattern

polar angle,  $\theta$ . On the ellipsoid this effect tends to reflect the edge rays of the horn pattern toward the center of the main dish aperture. The Cassegrain subreflector behaves oppositely spreading the horn edge rays off the rim of the main reflector. Because the Gregorian geometry gives a higher dish taper, it results in lower sidelobes and lower spillover losses.

In the following paragraphs, with the aid of Fig. 3.1, the analytical steps for relating dish, subreflector and horn parameters according to the optimized Japanese criteria are presented.

Having chosen  $Y_0 = -157.48$  cms the center point of the paraboloid with focal length 177.8 cms, we can determine the eccentricity,  $e$ , of the ellipsoidal subreflector surface and the optimum tilt angle  $\beta$  between the axis of the ellipsoid and the z-axis of the paraboloid from equation (2.1).

$$(2.1) \quad |y_e| = \frac{4fe \sin \beta}{1 + e^2 - 2e \cos \beta}$$

We want to solve for  $e$  and  $\beta$  to make the horn and sub-reflector parameters optimum for the low sidelobe, low cross-polarization, and high aperture efficiency specifications of this project. Equation (2.1) is quadratic in  $e$  or  $\sin \beta$  and the roots can be easily found when, for example,  $e$  is assigned and  $\sin \beta$  determined. Several additional analytical relations are needed before we can make a judgment about the "best"  $e$  or  $\beta$ , however. The tilt angle between the horn axis and the ellipsoid axis is given by the equation

$$(2.2) \quad \tan \alpha = \frac{(1 - e)^2 \sin \beta}{(1 + e)^2 \cos \beta - 2e}$$

It is convenient to use two coordinate origins, one at each foci,  $F_0$  and  $F_1$  of the ellipsoid. In terms of the rectangular coordinates at the confocal focus  $F_0$  shown in Fig. 3.1 the paraboloid surface is given by

$$(2.3) \quad x^2 + y^2 = 4f^2 - 4fz$$

Referred to  $x, y, z$  coordinates at  $F_0$  origin the ellipsoidal surface is given by

$$(2.3A) \quad x^2 + y^2 + z^2 = e^2(z \cos \beta - y \sin \beta + d)^2$$

Where  $d$  is given by

$$(2.4) \quad d = \frac{c(1-e^2)}{2e^2}$$

and  $c$  is the distance between foci of the ellipsoid,  $c$  can be called the expansion parameter because it can be made any length without changing the angles  $\varphi$ ,  $\beta$  and  $\theta_H$ .

Two parameters,  $\theta_H$  the semiflare angle of the horn and  $M$  the dual reflector magnification factor, have important effects on the performance of the antenna. When the semiflare angle,  $\theta_H$ , is greater than  $30^\circ$  the phase center of the conical corrugated horn remains nearly constant<sup>(6)</sup> over the conical horn pattern  $G(\theta_0, \varphi_0)$  (which pattern generally has no  $\varphi_0$  dependence) for variations in  $\theta_0$ . However, for smaller values of  $\theta_H$  the phase center of the horn changes with  $\theta$ . The magnification factor  $M$  should be large if the angular sector to be scanned by horn feed motion is to be large. The factor  $M$  can be interpreted to mean that the equivalent prime focus fed paraboloid<sup>(7)</sup> would have a focal length  $f' = Mf$ . For large  $M$  the semiflare angle should be small. In any case  $c$ ,  $e$  and  $\beta$  must be set so that the illuminated area of the subreflector is  $15\lambda$  or greater to keep the level of diffraction generated crosspolarization low.<sup>(3)</sup>

Proceeding, then, to develop relations for  $\theta_H$  and  $M$ , we can write

$$(2.5) \quad \tan \frac{\theta_H}{2} = \frac{R(1+e^2-2e\cos\beta)}{2f(1-e^2)}$$

where  $R$  is the circular paraboloid radius.

$$(2.6) \quad M = \frac{(1-e^2)}{1+e^2-2e\cos\beta}$$

Because the horn pattern is usually known in spherical coordinates  $(r, \theta_0, \varphi_0)$  with origin at  $F_1$  of Fig. 3.1, it is useful to write equations for the ellipsoid at  $F_1$  in both rectangular and spherical coordinates as

$$(2.7) \quad x_0^2 + y_0^2 + z_0^2 = e^2(z_0 \cos\alpha - y_0 \sin\alpha + d)^2$$

$$(2.8) \quad r = \frac{ed}{1 - e\cos\alpha \cos\theta_0 + e\sin\alpha \sin\theta_0 \sin\varphi_0}$$

$$x_0 = r \sin\theta_0 \cos\varphi_0$$

$$y_0 = r \sin\theta_0 \sin\varphi_0$$

$$z_0 = r \cos\theta_0$$

where  $\theta_H = \theta_{\max}$  defining illuminated edge of subreflector.

To transform coordinates from origin at  $F_1$  to  $F_0$  write

$$(2.9) \quad \begin{aligned} x_0 &= x \\ y_0 &= -y \cos \gamma + z \sin \gamma - e \sin \alpha \\ z_0 &= -y \sin \gamma - z \cos \gamma + e \cos \alpha \end{aligned}$$

where  $\gamma = \alpha - \beta$

The procedure for setting  $e$  and  $\beta$  is then to choose or value  $\theta_H$  and using equations (1) and (5) solve for  $\beta$  and then  $e$  from equation (2).

The aperture coordinates  $(x, y)$  in a plane in front of the paraboloid section can be related to the spherical angle coordinates of the horn pattern  $G(\theta_0, \phi_0)$  using the above equations and other Japanese criteria transforms to get

$$(2.10) \quad \begin{aligned} x &= -B \tan \theta_0 \cos \phi_0 \\ y &= y_c - B \tan \theta_0 \sin \phi_0 \end{aligned}$$

where

$$B = \frac{2f(1-e^2)^2}{1+e^2-2e \cos \beta}$$

In Fig. 3.4 the effect of varying  $e$  and  $\beta$  on  $\theta_1 = \theta_H$  the semiflare angle and  $M$  the Magnification can be seen. Also, the expansion factor  $c$  is shown for two values, 88.9 cms (35") and 177.8 cms (70"). In all cases the parameters,  $e, \alpha, \beta$ , are optimized according to the Japanese criteria. The illuminated portions of the ellipsoidal subreflectors shown in the  $y-z$  plane all have diameters greater than  $15\lambda$  where here  $\lambda = 2.54$  cms. We see that for an eccentricity of  $e = 0.6$  the semiflare angle is  $\theta_1 = 9.9^\circ$ . On the demonstration model  $e$  was selected as 0.538 making a semiflare angle for the horn of about  $12^\circ$  and the diameter of the illuminated portion of the subreflector is greater than 38 cms with  $c = 88.9$  cms. In order to attain a larger Magnification factor  $M$ , a value of  $e = 0.66$  was chosen. Now  $M = 4.84$  and  $\theta_1 = 8.1^\circ$ .  $c$  must be increased to about 177.8 cms to make the subreflector large enough for low cross-polarization. The horn subreflectors for the demonstration model with  $e = .538$  and  $\theta_1 = 12^\circ$  will be compared with scanning characteristics of the  $e = .66, \theta_1 = 8.10$  system later in the report when scanning by feed motion is investigated.

#### Considerations in Constructing the Ellipsoidal Subreflector:

The subreflector surface given by equations (2.7) and (2.8) are ellipsoids of revolution tilted by  $\alpha$ . To build the surface using a lathe the equations for a "swept" surface of revolution about the axis of the ellipsoid are desired. Using the relations:

$$(2.11) \quad \begin{aligned} x_1 &= x_0 \\ y_1 &= y_0 \cos \alpha + z_0 \sin \alpha \\ z_1 &= -y_0 \sin \alpha + z_0 \cos \alpha \\ R_1^2 &= x_1^2 + y_1^2 \end{aligned}$$

Equation (2.7) is now written:

$$(2.12) \quad R_1^2 = d^2 e^2 + z e^2 dz - z^2 (1 - e^2)$$

When values  $x_0, y_0, z_0$  from (8) for  $\theta_0 = \theta_H$  are put into equation (2.11) then the radius,  $R_1$ , for turning the lathe can be found for points  $z_1$  along the ellipsoid axis. The values  $x_1$  and  $y_1$  define the subreflector edges or the end points to turn the lathe on the radius  $R_1$ .

Because the surface of the subreflector actually constructed for the demonstration model is not a true ellipsoid but was shaped to correct for phase errors of the conical horn this lathe or swept construction cannot be used but rather templates cut in the  $x_0, y_0, z_0$  coordinates and a reflecting surface stretched over the templates form the continuous subreflector surface.

### 3.3 Antenna Sidelobe Levels vs Aperture Efficiencies

Unlike for linear antenna arrays, a rigorous proof of the best sidelobe levels possible for a given antenna aperture efficiency (or gain) is not available for the (continuous) circular aperture reflector antenna. The problem, however, has been investigated by some able workers<sup>(8,9,10)</sup> and their best estimates for circular aperture distributions have been studied and extended by introducing new functions by authors of this paper. In the analysis to follow the numerical integration procedure to compute and evaluate the antenna patterns, beamwidths, aperture efficiencies and the first 5 sidelobe levels is presented.

Analytical Procedure for Antenna Pattern Computations:

The far field of a circular aperture in spherical coordinates is given by (11)

$$(3.1) \quad g(\theta, \phi) = \int_0^{2\pi} \int_0^a F(\rho', \phi') e^{j k \rho \sin \theta \cos(\phi - \phi')} \rho d\rho d\phi'$$

where

$a$  = radius of the aperture,

$F(\rho', \phi')$  = aperture illumination function,

$\theta, \phi$  = angular coordinates of its field point

and

$$h = 2\pi/\lambda$$

letting

$$r = \rho/a$$

$$u = \frac{2\pi a}{\lambda} \sin \theta$$

the pattern is given by

$$(3.2) \quad g(u, \phi) = a^2 \int_0^{2\pi} \int_0^1 f(r, \phi') e^{j u r \cos(\phi - \phi')} r dr d\phi'$$

where it is assumed that  $f(r, \phi')$  is normalized to unity. For aperture illuminations which are functions of the radius only,  $f(r, \phi') = f(r)$ , the integration with respect to  $\phi'$  can be performed exactly and we obtain

$$(3.3) \quad g(u) = 2\pi a^2 \int_0^1 f(r) r J_0(ur) dr$$

The integration with respect to  $r$  can be performed numerically for any given aperture illumination taper,  $f(r)$ . In the calculations performed here to investigate its location and magnitude of the sidelobe maximum corresponding to various illumination tapers, the numerical integration was performed using the IBM Scientific Software Package (SSP) subroutine QATR which integrates a given function by the trapezoidal rule together with Romberg's extrapolation method. The Bessel function was calculated with the IBM SSP subroutine BESJ.

The aperture efficiency  $E$  is defined as the ratio of the directive gain along the axis of the aperture,  $G_D$ , to the gain,  $G_0$ , for a uniformly illuminated aperture:

$$(3.4) \quad E = \frac{G_D}{G_0}$$

$$E = \frac{\left[ \frac{4\pi}{\lambda^2} \left| \int_A F(\xi, \eta) d\xi d\eta \right|^2 \right]}{\int_A |G(\xi, \eta)|^2 d\xi d\eta} \bigg/ \frac{4\pi A}{\lambda^2}$$

For a radially varying illumination function  $f(r)$  and aperture radius of unity,

$$G_D = \frac{4\pi}{\lambda^2} \frac{(2\pi)^2 \left| \int_0^1 r f(r) dr \right|^2}{2\pi \int_0^1 r |f^2(r)| dr}$$

$$G_0 = 4\pi^2 / \lambda^2$$

and

$$E = \frac{2 \left| \int_0^1 r f(r) dr \right|^2}{\int_0^1 r |f^2(r)| dr}$$

For most of the illumination function investigated it was straightforward to perform the two integrations involved in calculating the efficiency in closed form. The efficiencies for a circular aperture illuminated by a 76.2 cm,  $12^\circ$  corrugated horn and by the Japanese transform for dual reflector antennas were calculated using the IBM SSP subroutine QATR.

The results of the pattern and efficiency calculations are summarized in Table 3.1 which shows efficiency, half-power beamwidth, and sidelobe levels and locations for the various illumination functions studied and listed under "Key to Illumination Functions." Figs. 3.5 and 3.6 show plots of representative radial amplitude distributions investigated and summarized in Table 3.1. Note that the shape of the radial curves and the favorable edge illuminations are very similar for all the "ideal" aperture distributions. The first derivatives of the radial functions are all zero to reduce Gibbs' phenomena.

### 3.4 Analysis and Computation of Corrugated Conical Horn Near-Zone Patterns

An expression for the electric field on a spherical surface of Radius  $R_1$  from the apex of a corrugated conical horn of length  $R_0$  (see Fig. 3.7) has been obtained by Clarricoats<sup>(12)</sup>,

$$(4.1) \quad E(R_1, \theta) = \sum_{n=1}^N C_n h_n^{(2)}(k R_1) f_n'(\theta) \\ \text{(Series 1)}$$

where

$$(4.2) \quad C_n = \frac{\exp(-j k R_0)}{R_0} \frac{2n+1}{2n^2(n+1)^2 h_n^{(2)}(k R_0)} \int_0^{\theta_1} f_n'(\theta) f_n'(\theta) \sin \theta d\theta \\ \text{(Eqn. 2)}$$

Here

$$(4.3) \quad f_n'(\theta) = \frac{P_n'(\cos \theta)}{\sin \theta} + \frac{d P_n'(\cos \theta)}{d \theta}$$

$P_n'(\cos \theta)$  is the associated Legendre function of the first kind of degree  $n$  and order 1,

$h_n^{(2)}(x)$  is the spherical Hankel function of the second kind of order  $n$ ,

$k$  is the wave number,  $2\pi/\lambda$ ,

$\theta$  is the angle between the horn axis and the line from the horn apex to the field point,

$\theta_1$  is the horn semiflare angle,

$\nu$  is given by the smallest solution of the equation

$$(4.4) \quad f_n'(\theta) = 0$$

and  $N$  is sufficiently large so that further terms in the sum (1) can be neglected. The purpose here is to describe in detail the numerical evaluation of  $E(R_1, \theta)$ .

We begin with the evaluation of  $f'_\nu(\theta)$ ,

$$(4.3) \quad f'_\nu(\theta) = \frac{P'_\nu(\cos\theta)}{\sin\theta} + \frac{d P'_\nu(\cos\theta)}{d\theta}$$

The second term on the R.H.S. of (4.3) can be written

$$\begin{aligned} \frac{d P'_\nu(\cos\theta)}{d\theta} &= \frac{d P'_\nu(\cos\theta)}{d(\cos\theta)} \frac{d(\cos\theta)}{d\theta} \\ &= -\sin\theta \left. \frac{d P'_\nu(x)}{dx} \right|_{x=\cos\theta} \\ &= -\sin\theta P'_\nu(\cos\theta) \end{aligned}$$

so that

$$(4.5) \quad f'_\nu(\theta) = \frac{P'_\nu(\cos\theta)}{\sin\theta} - \sin\theta P'_\nu(\cos\theta)$$

Using the relation<sup>(13)</sup>

$$(4.6) \quad (x^2-1) P''_\nu(x) = \nu x P'_\nu(x) - (\nu+1) P'_{\nu-1}(x)$$

with  $x = \cos\theta$ , we have

$$-\sin^2\theta P''_\nu(\cos\theta) = \nu \cos\theta P'_\nu(\cos\theta) - (\nu+1) P'_{\nu-1}(\cos\theta)$$

or

$$(4.7) \quad -\sin\theta P'_\nu(\cos\theta) = \nu \cos\theta \frac{P'_\nu(\cos\theta)}{\sin\theta} - (\nu+1) \frac{P'_{\nu-1}(\cos\theta)}{\sin\theta}$$

Substituting (4.7) in (4.5) then yields

$$(4.8) \quad f'_\nu(\theta) = (1+\nu) \cos\theta \frac{P'_\nu(\cos\theta)}{\sin\theta} - (\nu+1) \frac{P'_{\nu-1}(\cos\theta)}{\sin\theta}$$

Now we make use of the following recursion relation<sup>(14)</sup> to reduce the evaluation of  $f'_\nu(\theta)$  to the evaluation of  $P'_\nu(\cos\theta)$

$$\text{for } -1 \leq \nu \leq 1: \quad \nu P'_{\nu+1}(x) = (2\nu+1)x P'_\nu(x) - (\nu+1) P'_{\nu-1}(x)$$

or, equivalently,

$$(4.9) \quad \nu \frac{P'_{\nu+1}(\cos\theta)}{\sin\theta} = (2\nu+1) \cos\theta \frac{P'_\nu(\cos\theta)}{\sin\theta} - (\nu+1) \frac{P'_{\nu-1}(\cos\theta)}{\sin\theta}$$

Let\*

$$\bar{\nu} = \nu - \text{Int}(\nu)$$

\* We need only be concerned with positive  $\bar{\nu}$  since  $\nu$  is given by the zero of  $f_\nu(\theta) = 0$  and is positive<sup>(15)</sup>.

where  $\text{Int}(\nu)$  is the integer value of  $\nu$  (i.e., the largest integer less than or equal to  $\nu$ ).

$$\text{Then} \quad 0 \leq \bar{\nu} < 1$$

$$\text{and} \quad -1 \leq \bar{\nu} - 1 < 0$$

Thus, if we can calculate  $P_{\nu}'(\cos \theta)/\sin \theta$  for  $-1 \leq \nu \leq 1$  we can, given any positive value of  $\nu$ , first calculate  $P_{\bar{\nu}}'(\cos \theta)/\sin \theta$  and  $P_{\bar{\nu}-1}'(\cos \theta)/\sin \theta$ . If  $\bar{\nu} = \nu$  then  $f_{\nu}'(\theta)$  is given by (4.8). Otherwise we use the recursion relation (4.9) repeatedly until we arrive at the given value of  $\nu$ .

An example may be worthwhile at this point. Suppose we wish to evaluate  $f_{\nu}'(\theta)$  for  $\nu = 3.5$ . We have  $\text{Int}(3.5) = 3$  so that  $\bar{\nu} = 3.5 - 3 = 0.5$  and  $\bar{\nu} - 1 = -0.5$ . Assuming we can evaluate  $P_{\nu}'(\cos \theta)/\sin \theta$  for  $-1 \leq \nu \leq 1$ , we start with  $P_{0.5}'(\cos \theta)/\sin \theta$  and  $P_{-0.5}'(\cos \theta)/\sin \theta$ . Then

$$(4.10a) \quad \frac{P_{1.5}'(\cos \theta)}{\sin \theta} = [2(0.5)+1] \cos \theta \frac{P_{0.5}'(\cos \theta)}{\sin \theta} - (0.5+1) \frac{P_{-0.5}'(\cos \theta)}{\sin \theta},$$

$$(4.10b) \quad \frac{P_{2.5}'(\cos \theta)}{\sin \theta} = [2(1.5)+1] \cos \theta \frac{P_{1.5}'(\cos \theta)}{\sin \theta} - (1.5+1) \frac{P_{0.5}'(\cos \theta)}{\sin \theta},$$

and

$$(4.10c) \quad \frac{P_{3.5}'(\cos \theta)}{\sin \theta} = [2(2.5)+1] \cos \theta \frac{P_{2.5}'(\cos \theta)}{\sin \theta} - (2.5+1) \frac{P_{1.5}'(\cos \theta)}{\sin \theta}$$

We now have values for both  $P_{3.5}'(\cos \theta)/\sin \theta$  and  $P_{2.5}'(\cos \theta)/\sin \theta$  and we can evaluate  $f_{3.5}'(\theta)$  using Eq. (4.8).

The associated Legendre function of the first kind of degree  $\nu$  and order 1,  $P_{\nu}'(x)$ , is defined in terms of the (ordinary) Legendre function of the first kind of degree  $\nu$ ,  $P_{\nu}(x)$ , by

$$(4.11) \quad P_{\nu}'(x) = (1-x^2)^{1/2} \frac{dP_{\nu}(x)}{dx}$$

(It is important to note here that the definitive

$$(4.11a) \quad P_{\nu}'(x) = -(1-x^2)^{1/2} \frac{dP_{\nu}(x)}{dx}$$

is also used by some authors (16). However, we will use (4.11) rather than (4.11a) so that our results will be consistent with tables of  $P_{\nu}'(\cos \theta)/\sin \theta$  and  $dP_{\nu}'(\cos \theta)/d\theta$  prepared by Clarricoats. The definition (11a) could just as well be used with no effect on the evaluation of  $E(R_1, \theta)$  since only the sign of  $f_{\nu}'(\theta)$  is changed and  $f_{\nu}'(\theta)$  enters into the calculation of  $E(R_1, \theta)$

via the product  $f_{\nu}'(\theta) f_{\nu}'(\theta)$  in Eq. (4.2).) Combining (4.11) with the relation (13).

$$(4.12) \quad (1-x^2) \frac{dP_{\nu}(x)}{dx} = \nu P_{\nu-1}(x) - \nu x P_{\nu}(x)$$

we have

$$(4.13) \quad P_{\nu}'(x) = \frac{\nu P_{\nu-1}(x)}{(1-x^2)^{1/2}} - \frac{\nu x P_{\nu}(x)}{(1-x^2)^{1/2}}$$

Letting  $x = \cos \theta$  in (4.13),

$$P_{\nu}'(\cos \theta) = \nu \frac{P_{\nu-1}(\cos \theta)}{\sin \theta} - \nu \cos \theta \frac{P_{\nu}(\cos \theta)}{\sin \theta}$$

or

$$(4.14) \quad \frac{P_{\nu}'(\cos \theta)}{\sin \theta} = \nu \frac{P_{\nu-1}(\cos \theta)}{\sin^2 \theta} - \nu \cos \theta \frac{P_{\nu}(\cos \theta)}{\sin^2 \theta}$$

Now the Legendre function of the first kind of degree  $\nu$ ,  $P_{\nu}(z)$ , has the hypergeometric series representation (17)

$$(4.15) \quad \begin{aligned} P_{\nu}(z) &= F(-\nu, \nu+1; 1; \frac{1-z}{2}) \\ &= \sum_{h_2=0}^{\infty} \frac{(-\nu)_{h_2} (\nu+1)_{h_2}}{(h_2!)^2} \left(\frac{1-z}{2}\right)^{h_2} \end{aligned}$$

where  $(\nu)_{h_2}$  is defined by

$$(4.16) \quad \begin{cases} (\nu)_0 = 1 \\ (\nu)_n = \nu(\nu+1)\dots(\nu+n-1) \end{cases}$$

Letting  $z = \cos \theta$  and noting the trigonometric identity

$$(4.17) \quad \frac{1-\cos \theta}{2} = \sin^2 \frac{\theta}{2}$$

we have

$$(4.18) \quad P_{\nu}(\cos \theta) = \sum_{h_2=0}^{\infty} \frac{(-\nu)_{h_2} (\nu+1)_{h_2}}{(h_2!)^2} \sin^{2h_2} \frac{\theta}{2}$$

Combining (4.18) and 4.14),

$$\begin{aligned} \frac{P_{\nu}'(\cos \theta)}{\sin \theta} &= \frac{\nu}{\sin^2 \theta} \sum_{h_2=0}^{\infty} \frac{[-(\nu-1)]_{h_2} (\nu)_{h_2}}{(h_2!)^2} \sin^{2h_2} \frac{\theta}{2} \\ &\quad - \frac{\nu \cos \theta}{\sin^2 \theta} \sum_{h_2=0}^{\infty} \frac{(-\nu)_{h_2} (\nu+1)_{h_2}}{(h_2!)^2} \sin^{2h_2} \frac{\theta}{2} \end{aligned}$$

Writing the  $k = 0$  term of the sums separately then yields

$$(4.19) \quad \frac{P'_\nu(\cos\theta)}{\sin\theta} = \nu \frac{(1-\cos\theta)}{\sin^2\theta} + \frac{\nu}{\sin^2\theta} \sum_{k=1}^{\infty} \frac{[-(\nu-k)]_{k_2} (\nu)_{k_2}}{(k_2!)^2} \sin^{2k_2} \frac{\theta}{2} \\ - \frac{\nu \cos\theta}{\sin^2\theta} \sum_{k_2=1}^{\infty} \frac{(-\nu)_{k_2} (\nu+1)_{k_2}}{(k_2!)^2} \sin^{2k_2} \frac{\theta}{2}$$

The  $\sin^2\theta$  in the denominator of the RHS of (4.19) seems to present a singularity at  $\theta = 0$ . However this "singularity" is only apparent. Noting

$$\sin^2\theta = \sin^2\left(2\frac{\theta}{2}\right) = \left(2\sin\frac{\theta}{2}\cos\frac{\theta}{2}\right)^2 = 4\cos^2\frac{\theta}{2}\sin^2\frac{\theta}{2}$$

and

$$\frac{1-\cos\theta}{\sin^2\theta} = \frac{2\sin^2\frac{\theta}{2}}{4\cos^2\frac{\theta}{2}\sin^2\frac{\theta}{2}} = \frac{1}{2\cos^2\frac{\theta}{2}}$$

(4.19) becomes

$$(4.20) \quad \frac{P'_\nu(\cos\theta)}{\sin\theta} = \frac{\nu}{2\cos^2\frac{\theta}{2}} \left[ 1 + \frac{1}{2} \left\{ \sum_{k_2=1}^{\infty} \frac{[-(\nu-k)]_{k_2} (\nu)_{k_2}}{(k_2!)^2} \sin^{2(k_2-1)} \frac{\theta}{2} \right. \right. \\ \left. \left. - \cos\theta \sum_{k_2=1}^{\infty} \frac{(-\nu)_{k_2} (\nu+1)_{k_2}}{(k_2!)^2} \sin^{2(k_2-1)} \frac{\theta}{2} \right\} \right]$$

Hence there is no difficulty in evaluating  $P'_\nu(\cos\theta)/\sin\theta$  for  $\theta = 0$ . In fact, letting  $\theta = 0$  in (4.20), we have

$$(4.21) \quad \frac{P'_\nu(\cos\theta)}{\sin\theta} \Big|_{\theta=0} = \frac{\nu}{2} \left[ 1 + \frac{1}{2} \left\{ -(\nu-1)\nu - (-\nu)(\nu+1) \right\} \right] \\ = \frac{\nu}{2} \left[ 1 + \frac{1}{2} \left\{ -\nu^2 + \nu + \nu^2 + \nu \right\} \right] = \frac{\nu(\nu+1)}{2}$$

We first consider the expression for  $P'_\nu(\cos\theta)/\sin\theta$  given by (4.20) when  $\nu$  is an integer. We need treat only  $\nu = 0$  and  $\nu = 1$  since the recursion relation (4.9) can be used to calculate  $P'_\nu(\cos\theta)/\sin\theta$  for  $\nu$  any integer greater than one starting with  $P'_0(\cos\theta)/\sin\theta$  and  $P'_1(\cos\theta)/\sin\theta$ . For  $\nu = 0$ , it follows from (4.20) that

$$P'_0(\cos\theta)/\sin\theta = 0$$

while for  $\nu = 1$  only the  $k = 1$  term of the second sum of the

RHS of (4.20) is non-zero so that

$$(4.22) \quad \frac{P'_1(\cos \theta)}{\sin \theta} = \frac{1}{2 \cos^2 \frac{\theta}{2}} \left[ 1 - \frac{\cos \theta}{2} \frac{(-1)(2)}{1} \right]$$

$$= \frac{1}{2 \cos^2 \frac{\theta}{2}} (1 + \cos \theta) = \frac{1 + \cos^2 \frac{\theta}{2} - \sin^2 \frac{\theta}{2}}{2 \cos^2 \frac{\theta}{2}} = 1$$

These values are consistent with the definition (4.11) since  $P_0(x) = 1$  and  $P_1(x) = x$  so that  $P'_0(x) = 0$  and  $P'_1(x) = (1-x^2)^{-\frac{1}{2}}$  or  $P'_1(\cos \theta) = \sin \theta$ .

Next, we examine the convergence of the sums in (4.20) when  $\nu$  is not an integer. As shown above we can restrict attention to  $\nu$  in the range  $-1 < \nu < 1$ . Let us first consider the first sum in (4.20)

$$(4.23) \quad S_1 = \frac{1}{2} \sum_{k=1}^{\infty} \frac{[-(\nu-1)_k (\nu)_k]}{(k!)^2} \sin^{2(k-\nu)} \frac{\theta}{2}$$

$$= \frac{1}{2} \left[ \frac{(1-\nu)\nu}{1^2} + \frac{(1-\nu)(2-\nu)\nu(\nu+1)}{(1 \cdot 2)^2} \sin^2 \frac{\theta}{2} + \frac{(1-\nu)(2-\nu)(3-\nu)\nu(\nu+1)(\nu+2)}{(1 \cdot 2 \cdot 3)^2} \sin^4 \frac{\theta}{2} + \dots \right]$$

If we let the successive terms of the sum be denoted by  $T_1, T_2, \dots$ , it is seen that

$$T_{n+1} = \frac{T_n (n+1-\nu)(\nu+n)}{(n+1)^2} \sin^2 \frac{\theta}{2}, \quad n=1, 2, \dots$$

Since

$$\frac{(n+1-\nu)(\nu+n)}{(n+1)^2} = \frac{(n+1-\nu)(n+1+\nu-1)}{(n+1)^2}$$

$$= \frac{(n+1)^2 - (n+1-\nu)(\nu-1)}{(n+1)^2} = 1 - \frac{1}{n+1} - \frac{\nu(\nu-1)}{(n+1)^2},$$

$$0 < \frac{(n+1-\nu)(\nu+n)}{(n+1)^2} < 1$$

and

$$\left| \frac{T_{n+1}}{T_n} \right| < \sin^2 \frac{\theta}{2}$$

Also, all the terms of  $S_1$  are positive or negative according as  $\nu$  is positive or negative respectively. Letting

$$r = \sin^2 \frac{\theta}{2}$$

we see that

$$(4.24) \quad |S_1| < \frac{1}{2} |T_1| (1 + r + r^2 + \dots)$$

If we let the sum of the first  $N$  terms of  $S_1$  be denoted by  $S_{1N}$  and the sum of the remaining terms be denoted by  $R_{1N}$  then

$$(4.25) \quad |S_1| = |S_{1N}| + |R_{1N}|$$

where

$$\begin{aligned} |R_{1N}| &< \frac{1}{2} |T_1| (r^N + r^{N+1} + \dots) \\ &= \frac{1}{2} |T_1| \left( \frac{1}{1-r} - \frac{1-r^N}{1-r} \right) \\ &= \frac{1}{2} |T_1| \frac{r^N}{1-r} \end{aligned}$$

But  $|T_1| < 2$

so that  $|R_{1N}| < \frac{r^N}{1-r}$

It is now a simple matter to find  $N$  such that  $|R_{1N}| < \epsilon$  when  $\epsilon$  is some small constant. For the requirement that

$$(4.26) \quad \frac{r^N}{1-r} \leq \epsilon,$$

or

$$r^N \leq \epsilon(1-r),$$

is equivalent to  $N \ln r \leq \ln \epsilon + \ln(1-r)$

so that we can choose

$$(4.27) \quad N = \text{Int} \left[ \frac{\ln \epsilon + \ln(1-r)}{\ln r} \right] + 1,$$

$$r = \sin^2 \frac{\theta}{2}$$

The second sum in (4.20) is similarly treated. Let

$$\begin{aligned} (4.28) \quad S_2 &= \frac{1}{2} \sum_{l_2=1}^{\infty} \frac{(-\nu)_{l_2} (\nu+1)_{l_2}}{(l_2!)^2} \sin^{2(l_2-1)} \frac{\theta}{2} \\ &= \frac{1}{2} \left[ \frac{-\nu(\nu+1)}{1^2} + \frac{(-\nu)(-\nu+1)(\nu+1)(\nu+2)}{(1 \cdot 2)^2} \sin^2 \frac{\theta}{2} + \frac{(-\nu)(-\nu+1)(-\nu+2)(\nu+1)(\nu+2)(\nu+3)}{(1 \cdot 2 \cdot 3)^2} \sin^4 \frac{\theta}{2} \right. \\ &\quad \left. + \dots \right] \end{aligned}$$

Letting the successive terms of the sum again be denoted by  $T_1, T_2, \dots$ , we have

$$(4.29) \quad T_{n+1} = T_n \frac{(n-\nu)(n+1+\nu)}{(n+1)^2} \sin^2 \frac{\theta}{2}, \quad n=1, 2, \dots$$

Since

$$\begin{aligned} \frac{(n-\nu)(n+1+\nu)}{(n+1)^2} &= \frac{[(n+1)-(\nu+1)](n+1+\nu)}{(n+1)^2} \\ &= \frac{(n+1)^2 - (n+1) - \nu(\nu+1)}{(n+1)^2} = 1 - \frac{1}{n+1} - \frac{\nu(\nu+1)}{(n+1)^2}, \end{aligned}$$

$$0 < \frac{(n-\nu)(n+1+\nu)}{(n+1)^2} < 1$$

as before, and the remaining discussion applies unchanged to  $S_2$ .

The two sums converge very rapidly. If, for example, we set  $\epsilon = 10^{-9}$  then for  $\theta = 1^\circ$  at most 2 terms are required; for  $\theta = 10^\circ$  at most 4 terms are required, and for  $\theta = 20^\circ$  at most 6 terms are required.

The programming to calculate  $f'_\nu(\theta)$  is straightforward following the analysis described above. A check on the computer program is provided by the table of the associated Legendre functions prepared by Clarricoats (18). As shown above,  $f'_\nu(\theta)$  is given by a simple combination of  $P'_\nu(\cos \theta)/\sin \theta$  and  $P'_{\nu-1}(\cos \theta)/\sin \theta$ . The program to calculate  $f'_\nu(\theta)$  can print our intermediate values of  $P'_\nu(\cos \theta)/\sin \theta$  and  $P'_{\nu-1}(\cos \theta)/\sin \theta$ . Values thus obtained were found to be in perfect agreement with those given in Clarricoats' table.

Now that the calculation of  $f'_\nu(\theta)$  has been discussed, we turn our attention to the calculation of the integrals

$$(4.30) \quad I_n = \int_0^{\theta_1} f'_\nu(\theta) f'_n(\theta) \sin \theta \, d\theta, \quad n=1, 2, \dots$$

which appears in the expression for  $C_n$  in (4.2). Given  $\theta_1$ , the horn semiflare angle, the integrals can be calculated independently of the horn length. The value of the integrals can be stored and used to calculate the field of horns of any length provided that they have the same semiflare angle  $\theta_1$ . This is fortunate since the calculation of the  $I_n$  is the most time consuming and costly part of the calculation of the horn field. The value of  $\nu$ , as stated earlier, is the lowest root of the equation

$$f'_\nu(\theta_1) = 0$$

Clarricoats' graph and table<sup>(4)</sup> of the first root  $\nu$  of  $f'_\nu(\theta_1) = 0$  for the  $HE_{11}$  spherical mode can be used to obtain an approximate

value for  $\nu$ , and this value can then be refined using an iterative procedure for finding the zero of a non-linear equation. We made use of this program ZEROIN<sup>(19)</sup> which requires as inputs the left and right endpoints of an initial interval within which the zero lies, a specified tolerance, and a function sub-program for evaluating  $f_p'(\theta_1)$  as a function of  $\nu$ . For  $\theta = 11.997^\circ$ ,  $\nu$  we found to be 11.02500.

As far as the method of numerical integration is concerned, it is recommended that an adaptive quadrature routine be used. An adaptive quadrature algorithm employs different mesh sizes in different parts of the integration interval. A relatively coarse mesh can be used where the integral is smooth or slowly varying, and a finer mesh used in places where the integral varies rapidly. In this way the number of function evaluations required to yield a desired accuracy can be considerably smaller than for an algorithm employing a uniform mesh size. The algorithm used in evaluating the integrals  $I_n$  was the subroutine QUANC8<sup>(20)</sup>. (The name is derived from Quadrature, Adaptive, Newton-Cotes' 8-panel.) No difficulty was encountered using QUANC8 to evaluate  $I_n$  for  $n$  from 1 to 225 (the highest value of  $n$  for which  $I_n$  was calculated). The number of integral evaluations required by QUANC8 to calculate  $I_n$  to within a specified accuracy (a relative error criterion of  $10^{-9}$  was used) was examined functional over a range of  $n$  for  $n$  from 1 to 225;  $\theta_1$  was  $11.997^\circ$  and  $\nu$  was equal to 11.02500. It appears that on the whole the number of integrand evaluations increases linearly with  $n$  although the detailed behavior is quite irregular. Since the number of terms in the series (1) required for convergence is of the order of  $k R_0$  ( $k = 2\pi/\lambda$ ,  $R_0 =$  horn length), it follows that the computation time and cost to calculate the electric field of a corrugated horn increases approximately as the square of the length of the horn.

As a check on the integration, the values of the integrals obtained using QUANC8 were compared for several values of  $n$  with those obtained using the non-adaptive Romberg integration method DQATR<sup>(21)</sup>. It was found that when DQATR was able to evaluate  $I_n$  the result agreed with that obtained with QUANC8, but that for some values of  $n$  DQATR was unable to evaluate  $I_n$  to within the specified accuracy because of rounding errors.

The values of the integrals  $I_n$  were investigated against  $n$  for  $n$  from 0 to 225. A slowly damped oscillatory behavior was apparent. The value of zero for  $n = 0$  was obtained analytically. From (4.8)

$$(4.31) \quad f_0'(\theta) = \frac{P_0'(\cos \theta)}{\sin \theta} - \frac{P_{-1}'(\cos \theta)}{\sin \theta}$$

As we have seen earlier,  $P_0'(x) = 0$ , while  $P_{-1}'(x) = P_0'(x) = 0$ ,

a special case of the general relation<sup>(22)</sup>

$$(4.32) \quad P_{-1}^{\mu}(x) = P_{\nu}^{\mu}(x)$$

We now turn our attention to the calculation of the spherical Hankel functions of the second kind,  $h_n^{(2)}(x)$ , which appears in (4.1) and (4.2). The spherical Hankel function is given by

$$(4.33) \quad h_n^{(2)}(x) = j_n(x) - i y_n(x)$$

where

$$j_n(x) = \left(\frac{\pi}{2x}\right)^{1/2} J_{n+1/2}(x)$$

and

$$y_n(x) = \left(\frac{\pi}{2x}\right)^{1/2} Y_{n+1/2}(x)$$

are the spherical Bessel functions of the first and second kind respectively. The method of calculation used<sup>(23)</sup> is the following: Let  $M$  be an integer somewhat larger than the maximum of  $n$  and  $x$ . Assume  $F_M(x) = 0$ ,  $F_{M-1}(x) = 1$  and using the recursion relation<sup>(24)</sup>

$$(4.34) \quad F_I(x) = \frac{2I+3}{x} F_{I+1}(x) - F_{I+2}(x)$$

satisfied by all the spherical Bessel functions, calculate  $F_I(x)$  for  $I$  from  $M-2$  to  $-(n+1)$ . Provided that  $M$  was chosen sufficiently large the value of  $F_I(x)$  will be proportional to  $j_I(x)$  for  $I$  from  $-(n+1)$  to  $n$ . The constant of proportionality,  $P$ , is readily calculated since

$$(4.35) \quad P = \frac{j_0(x)}{F_0(x)}$$

and  $j_0(x)$  is simply equal to  $\sin(x)/x$ . Then

$$j_I(x) = P F_I(x), \quad I = 1, 2, \dots, n$$

and since<sup>(25)</sup>

$$y_I(x) = (-1)^{I+1} j_{-I-1}(x)$$

we have

$$y_I(x) = (-1)^{I+1} P F_{-(I+1)}(x), \quad I = 1, 2, \dots, n$$

The proper choice of  $M$  in the above algorithm must be clarified a little. Clearly  $M$  must be larger than  $n$  otherwise the backward recursion relation (4.22) starting with  $F_M(x) = 0$  and  $F_{M-1}(x) = 1$  will not be able to develop a sufficient number of significant figures by the time  $M = n$  is reached. In addition, if  $x$  is considerably larger than  $n$  and  $M$  is not chosen larger than  $x$  the algorithm will not yield correct values for  $j_n(x)$  and  $y_n(x)$ . On the other hand, choosing  $M$  unnecessarily large adds to the computational cost and serves no useful purpose. A little trial and error appears to be the last method for determining  $M$ : Start with a tentative guess and calculate

$j_n(x)$  and  $y_n(x)$ . Then increase  $M$  and recalculate  $j_n(x)$  and  $y_n(x)$ . If the two sets of values agree to within the desired number of significant figures, the first value of  $M$  was large enough. Otherwise increase  $M$  and try again. In our calculation here it was found that choosing  $M$  equal to the larger of  $n$  and  $x$  plus 20 gave excellent results.

It will be noted that the backwards recursion method, when used to calculate  $j_n(x)$  and  $y_n(x)$ , simultaneously yields values of  $j_I(x)$  and  $y_I(x)$  for all  $I$  from 0 to  $n$ . This fact can be put to good use in calculating the electric field of the horn from (4.1) and (4.2) since what is needed there are the values of  $h_n^{(2)}(kR_0)$  and  $h_n^{(2)}(kR_1)$  for  $n$  from 1 to  $N$ . Given  $N$  these values can all be generated in just two operations (one for the  $h_n^{(2)}(kR_0)$  and one for the  $h_n^{(2)}(kR_1)$ ) and then stored for use as needed in calculating the individual terms of the series.

The one key point in using (4.1) and (4.2) to calculate the horn electric field that has not yet been treated is the choice of the number of terms of the series,  $N$ . How large should  $N$  be so that the sum of further terms in the series can be neglected? Since this question is most easily answered for the case of the far field horn pattern (i.e.,  $kR_1 \rightarrow \infty$ ), we will first examine the convergence of the series (1) in the far field case and then consider convergence for the near field pattern.

Since

$$(4.36) \quad h_n^{(2)}(kR_1) = \left( \frac{\pi}{2kR_1} \right)^{1/2} H_{n+1/2}^{(2)}(kR_1)$$

and  $H_\nu^{(2)}(z)$  has the asymptotic form for  $\nu$  fixed and  $|z| \rightarrow \infty$  <sup>(26)</sup>

$$H_\nu^{(2)}(z) \sim \left( \frac{2}{\pi z} \right)^{1/2} e^{-i \left[ z - \left( \frac{1}{2} \nu + \frac{1}{4} \right) \pi \right]}$$

the magnitude of  $h_n^{(2)}(kR_1)$  is asymptotically equal to

$$\left( \frac{\pi}{2kR_1} \right)^{1/2} \left( \frac{2}{\pi kR_1} \right)^{1/2} = \frac{1}{kR_1}$$

and is independent of  $n$ . Likewise the constant  $\exp(-jkR_0/R_0)$  in  $C_n$  has no influence on convergence. The integrals

$$I_n = \int_0^{\theta_1} f_\nu'(\theta) f_n'(\theta) \sin \theta d\theta$$

have been discussed earlier and found to display a slowly damped oscillatory behavior which cannot contribute to the rapid convergence of the series. This means that, in the

far field case it is sufficient to examine the behavior of the combination

$$(4.37) \quad P_n \equiv \frac{(2n+1) f_n'(0)}{2n^2(n+1)^2 h_n^{(2)}(kR_0)}$$

(We have written  $f_n'(0)$  rather than  $f_n'(\theta)$  because the horn pattern is maximum on or close to the horn axis,  $\theta = 0$ .)

It is easy to show that

$$(4.38) \quad f_n'(0) = n(n+1)$$

since, from (4.8)

$$(4.39) \quad f_n'(0) = (1+n) P_n'(\cos\theta) \Big|_{\theta=0} - (n+1) P_{n-1}'(\cos\theta) \Big|_{\theta=0}$$

so that, with (4.21),

$$(4.40) \quad \begin{aligned} f_n'(0) &= (n+1) \frac{n(n+1)}{2} - (n+1) \frac{(n-1)n}{2} \\ &= \frac{n(n+1)}{2} [(n+1) - (n-1)] = n(n+1) \end{aligned}$$

$$\text{Thus} \quad \frac{(2n+1)}{2n^2(n+1)^2} f_n'(0) = \frac{2n+1}{2n(n+1)}$$

which decreases only as  $1/n$  and so cannot account for the convergence of the series for the horn electric field. The real force for convergence comes from the  $h_n^{(2)}(kR_0)$  in the denominator of  $P_n$ . To show this, we write

$$(4.41) \quad \begin{aligned} h_n^{(2)}(kR_0) &= f_n(kR_0) - i y_n(kR_0) \\ &= \left( \frac{\pi}{2kR_0} \right)^{1/2} \left[ J_{n+1/2}(kR_0) - i Y_{n+1/2}(kR_0) \right] \end{aligned}$$

and make use of the following asymptotic relations valid for large  $\nu$ , (27)

$$(4.42) \quad \begin{aligned} J_\nu(\nu \sec\beta) &\sim \left( \frac{2}{\pi \nu \tan\beta} \right)^{1/2} \cos \Psi \\ Y_\nu(\nu \sec\beta) &\sim \left( \frac{2}{\pi \nu \tan\beta} \right)^{1/2} \sin \Psi \end{aligned}$$

$$0 < \beta < \frac{\pi}{2}$$

$$\Psi = \nu(\tan\beta - \beta) - \frac{\pi}{4}$$

and

$$J_{\nu}(\nu \operatorname{sech} \alpha) \sim \frac{e^{\nu(\tanh \alpha - \alpha)}}{(2\pi\nu \tanh \alpha)^{1/2}}$$

$$Y_{\nu}(\nu \operatorname{sech} \alpha) \sim -\frac{e^{\nu(\alpha - \tanh \alpha)}}{(\frac{\pi\nu}{2} \tanh \alpha)^{1/2}}$$

$$\alpha > 0$$

Using standard trigonometric and hyperbolic function identities and letting  $\nu = n + \frac{1}{2}$  these asymptotic relations can be written as

$$(4.43a) \quad J_{n+\frac{1}{2}}(u(n+\frac{1}{2})) \sim \left\{ \frac{2}{\pi(n+\frac{1}{2})(u^2-1)^{1/2}} \right\}^{1/2} \cos \Psi$$

$$(4.43b) \quad Y_{n+\frac{1}{2}}(u(n+\frac{1}{2})) \sim \left\{ \frac{2}{\pi(n+\frac{1}{2})(u^2-1)^{1/2}} \right\}^{1/2} \sin \Psi$$

$$u > 1$$

$$\Psi = (n+\frac{1}{2}) \left[ (u^2-1)^{1/2} - \tan^{-1}(u^2-1)^{1/2} \right] - \frac{\pi}{4}$$

and

$$(4.44a) \quad J_{n+\frac{1}{2}}(u(n+\frac{1}{2})) \sim e^{\frac{-(n+\frac{1}{2})[\tanh^{-1}(1-u^2)^{1/2} - (1-u^2)^{1/2}]}{[2\pi(n+\frac{1}{2})(1-u^2)^{1/2}]^{1/2}}}$$

$$(4.44b) \quad Y_{n+\frac{1}{2}}(u(n+\frac{1}{2})) \sim e^{\frac{(n+\frac{1}{2})[\tanh^{-1}(1-u^2)^{1/2} - (1-u^2)^{1/2}]}{[\frac{\pi(n+\frac{1}{2})}{2}(1-u^2)^{1/2}]^{1/2}}}$$

$$u < 1$$

Relating (4.23 a,b) and (4.24 a,b) to the asymptotic behavior of  $j_n(kR_0)$  and  $y_n(kR_0)$ , it is apparent that (4.23 a,b) apply for  $n + \frac{1}{2} > kR_0$ . Hence, as  $n + \frac{1}{2}$  increases past  $kR_0$ , the dominant behavior of  $j_n(kR_0)$  and  $y_n(kR_0)$  viewed as functions of  $n$  changes from oscillatory to exponential. Thus the number of terms of the series (1) required for convergence,  $N$ , must be at least as large as  $kR_0$  and we can restrict our attention to the behavior of the terms of the series for  $n > kR_0$ .

We plotted the function

$$(4.45) \quad g(u) = \tanh^{-1} (1-u^2)^{1/2} - (1-u^2)^{1/2}$$

as a function of  $u$  as  $u$  decreases from 1. Since  $u(n+\frac{1}{2}) = KR_0$ ,  $u$  decreasing from 1 corresponds to  $n+\frac{1}{2}$  increasing from  $KR_0$ .

The fact that  $g(u)$  is positive for  $u < 1$  implies that as  $n$  increases  $J_{n+\frac{1}{2}}(u(n+\frac{1}{2}))$  decreases as  $\exp\{-(n+\frac{1}{2})g(u)\}$  while  $Y_{n+\frac{1}{2}}(u(n+\frac{1}{2}))$  increases as  $\exp\{(n+\frac{1}{2})g(u)\}$ . Note that  $(n+\frac{1}{2})g(u)$  increases as  $n$  increases not only because of the factor  $n+\frac{1}{2}$  but also because  $u = KR_0/(n+\frac{1}{2})$  decreases and  $g(u)$  increases. Thus in  $h_n^{(2)}(KR_0) = j_n(KR_0) - i y_n(KR_0)$ , as  $n+\frac{1}{2}$  increases from  $KR_0$ ,  $j_n(KR_0)$  becomes negligibly small compared to  $y_n(KR_0)$ .

Hence, to within a constant

$$(4.46) \quad P_n = \frac{2n+1}{2n(n+1)h_n^{(2)}(KR_0)} \sim \frac{2n+1}{2n(n+1)} \frac{1}{\frac{\exp\{(n+\frac{1}{2})g(u)\}}{[(n+\frac{1}{2})(1-u^2)^{1/2}]^{1/2}}}$$

or

$$(4.47) \quad P_n \sim \frac{(2n+1)(n+\frac{1}{2})^{1/2}}{2n(n+1)} (1-u^2)^{1/4} \exp\{-(n+\frac{1}{2})g(u)\}$$

where

$$u = KR_0/n + \frac{1}{2}$$

and

$$g(u) = \tanh^{-1} (1-u^2)^{1/2} - (1-u^2)^{1/2}$$

Thus the rapid convergence of the series (1) as the number of terms of the series included increases past  $KR_0$  is attributable to the factor  $\exp\{-(n+\frac{1}{2})g(u)\}$  derived from the  $h_n^{(2)}(KR_0)$  in the denominator of (2).

To give an idea of how  $P_n$  decreases as  $n$  increases from  $KR_0$  we have calculated  $P_n$  for several values of  $n$  from (4.25) for  $KR_0 = 100$  and 200.

For  $KR_0 = 100$ :

| $n$ | $u$  | $(1-u^2)^{1/4}$ | $\exp\{-(n+\frac{1}{2})g(u)\}$ | $\frac{(2n+1)(n+\frac{1}{2})^{1/2}}{2n(n+1)}$ | $P_n$   |
|-----|------|-----------------|--------------------------------|---|---------|
| 100 | .995 | .316            | .966                           | .100  | .030    |
| 105 | .948 | .565            | .300                           | .097  | .016    |
| 110 | .905 | .652            | .045                           | .095  | .0028   |
| 115 | .866 | .707            | .0034                          | .093  | .00022  |
| 120 | .830 | .747            | .00017                         | .091  | .000012 |

For  $MR_0 = 200$ :

| n   | u    | $(1-u^2)^{1/4}$ | $\exp\left\{-\left(n+\frac{1}{2}\right)g(u)\right\}$ | $\frac{(2n+1)(n+\frac{1}{2})^{1/2}}{2n(n+1)}$ | $P_n$   |
|-----|------|-----------------|--|---|---------|
| 200 | .998 | .266            | .966   | .071  | .018    |
| 205 | .973 | .479            | .492   | .070  | .016    |
| 210 | .950 | .558            | .103   | .069  | .0040   |
| 215 | .928 | .610            | .021   | .068  | .00086  |
| 220 | .907 | .649            | .0021  | .067  | .000093 |
| 225 | .887 | .680            | .00030   | .067  | .000013 |

Note that the decreases of  $P_n$  is almost entirely due to the exponential; the  $\left[\frac{(2n+1)(n+\frac{1}{2})^{1/2}}{2n(n+1)}\right]$  factor decreases extremely slowly, and the  $(1-u^2)^{1/4}$  factor increases slowly as n increases.

So far in our examination of the convergence of the series (1) we have made use of the far field assumption to replace  $h_n^{(2)}(MR_1)$  by its large argument asymptotic form with magnitude  $1/MR_1$  independent of n. What happens in the near field of the horn aperture? It is clear that in this limit as  $R_1 \rightarrow R_0$  the series (1) becomes a highly inefficient method of computing the horn aperture field since the  $h_n^{(2)}(MR_1)$  in (1) cancels the  $h_n^{(2)}(MR_0)$  in (2) which as we have seen accounts for the rapid convergence of the series in the far field case. If, however,  $MR_1$  is somewhat larger than  $MR_0$ , say  $MR_1 > MR_0 + 15$ , then the above analysis of convergence in the far field case continues to apply. This is so because the  $1/h_n^{(2)}(MR_0)$  in (2) starts to decrease rapidly as soon as  $n+\frac{1}{2} > MR_0$  whereas the switch from oscillatory to exponential behavior for the  $h_n^{(2)}(MR_1)$  in (1) does not occur until  $n+\frac{1}{2} > MR_1$ . Thus, as long as  $MR_1$  is sufficiently larger than  $MR_0$  for the exponential decrease of  $1/h_n^{(2)}(MR_0)$  to get a "good head start" on  $h_n^{(2)}(MR_1)$  there will be no problem with obtaining convergence. Only as the horn aperture is closely approached are convergence problems likely to be encountered; here caution in using (1) and (2) to calculate the horn field is clearly indicated.

As an example of how the coefficients  $C_n$  in (2) behave as n increases past  $MR_0$ , the following table presents the real and imaginary parts of  $C_n$  for n from 150 to 225. These values are for a horn with semi-flare angle of  $11.997^\circ$  and  $R_0 = 76.2$  cm. The wavelength  $\lambda$  is 2.50 cm so that  $MR_0 = (2\pi/\lambda)R_0 = 191.5$ .

| <u>n</u> | <u>Real [C<sub>n</sub>]</u> | <u>Imag [C<sub>n</sub>]</u> |
|----------|-----------------------------|-----------------------------|
| 150      | 0.3985 E-05                 | -0.2651 E-04                |
| 155      | -0.1808 E-05                | 0.2826 E-04                 |
| 160      | 0.8861 E-06                 | 0.4324 E-05                 |
| 165      | 0.9486 E-05                 | -0.1450 E-04                |
| 170      | -0.1699 E-04                | 0.6299 E-05                 |
| 175      | 0.2340 E-05                 | 0.1489 E-05                 |
| 180      | -0.2484 E-05                | 0.1015 E-04                 |
| 185      | 0.9723 E-05                 | 0.2910 E-05                 |
| 190      | 0.9444 E-06                 | -0.9171 E-06                |
| 195      | -0.8590 E-06                | 0.3131 E-05                 |
| 200      | -0.1757 E-06                | 0.1270 E-05                 |
| 205      | -0.5559 E-08                | 0.4386 E-07                 |
| 210      | 0.3207 E-08                 | -0.2538 E-07                |
| 215      | 0.3693 E-09                 | -0.2923 E-08                |
| 220      | 0.4862 E-11                 | -0.3849 E-10                |
| 225      | -0.1247 E-11                | 0.9872 E-11                 |

Note the sharp decreases of both the real and imaginary parts of  $C_n$  as  $n$  increases beyond 200.

The above analysis of the convergence of the series (1) completes this discussion of the calculation of the electric field of a corrugated horn. The principal steps of the calculation procedure are as follows:

1) Estimate the number of terms of the series required,  $N$ , using (4.25) to approximate the behavior of the coefficients  $C_n$  for  $n > MR_0$  (a reasonable working estimate is  $N = \text{Int}(MR_0) + 25$ ).

2) Given  $\theta_1$ , the horn semi-flare angle, calculate the value of  $\nu$  given by the lowest root of the equation  $f'_\nu(\theta) = 0$ .

3) Calculate and store the values of the integrals

$$I_n = \int_0^{\theta_1} f'_\nu(\theta) f'_n(\theta) \sin \theta d\theta, \quad n = 1, 2, \dots, N$$

4) Given  $R_0$ , the horn length, calculate and store the values of the coefficients  $C_n$ ,  $n = 1, 2, \dots, N$ . The values of  $h_n^{(2)}(MR_0)$ ,  $n = 1, 2, \dots, N$  are calculated in one operation prior to the calculation of the  $C_n$  and stored and used as needed.

5) If  $N$  is not sufficiently large as evidenced by the  $C_n$  not falling off enough as  $m$  approaches  $N$ , increase  $N$  and calculate additional integrals and coefficients.

6) Given  $R_1$ , the radius of the spherical surface over which the horn field is to be calculated, calculate and store the values of  $h_n^{(2)}(KR_1)$ ,  $n = 1, 2, \dots, N$  in one operation and then calculate and store the values of  $C_n h_n^{(2)}(KR_1)$ ,  $n = 1, 2, \dots, N$ .

7) For each value of  $\theta$  for which the field is desired, calculate  $E(R_1, \theta)$  using (1). The stored values of  $C_n h_n^{(2)}(KR_1)$  remain the same for the different values of  $\theta$ . Only the  $f'_n(\theta)$  need be calculated again as  $\theta$  changes.

Following the above analytical procedure near-zone horn patterns at 120.65 cms from the horn apex ( $F_1$  of Fig. 1.1) are shown in Figs. 3.8 and 3.9. Fig. 3.8 shows the conical corrugated horn amplitude function when the horn is 68.50 cms long. The edge taper at  $\theta = 12^\circ$  (semi-flare angle of the horn) for different horn lengths is shown in the insert. The horn phase function (departure from a spherical wavefront) is shown in Fig. 3.9 when the horn is 76.21 cms long and data is taken a 120.65 cms from the horn apex or focal point. The horn phase function changes very little over the range of horn lengths considered in this antenna design problem.

### 3.5 Design of the Corrugated Conical Horn

Under Section 3.2, Configuration, of this report the choices of tilt angle  $\alpha = 17^\circ$  (horn axis referred to the paraboloid axis) and  $\theta_1 = 12^\circ$  (horn semiflare angle) were discussed. Based on Section 4.0, horn analysis, the maximum length of the horn along its axis was chosen to be about 76.2 cms to give about a -20 dB taper at the edges of the illuminated portion of the subreflector. This antenna with this horn and subreflector design should produce -35 dB first sidelobes and -40 dB sidelobes beyond the main beam region with about 70-75% aperture efficiency. The same horn shortened to 61 cms length by removing 7.6 cms from mouth end should give the -30 dB first lobes with 75-80% aperture efficiency.

To construct the conical corrugated horn with flare angle of  $12^\circ$  we need to know the slot dimensions and to provide for a circular waveguide input port with good impedance match over the 11.7 to 12.2 GHz band. The horn will operate also over the 14 to 14.5 GHz band also; however, higher modes can exist in the circular waveguide at these higher frequencies. Slot details for the horn corrugations were dimensioned according to Clarricoats<sup>(28)</sup> and by comparing data on a 12 GHz antenna successfully built and tested by Antenna Santa Rita, São Paulo, Brazil, through information kindly provided by Prof. Marco Rabello and Marco Marchesi.

To insure that only the dominant  $TE_{11}$  mode can exist in the circular wave guide at 12.2 GHz a circular wave guide diameter of 1.892 cms was selected although the WR 75 guide of 2.024 cm diameter can also be used.

Some work<sup>(29)</sup> has been reported on the best corrugated slot depths to cover wide bandwidths. For excitation of the  $HE_{11}$  mode the slots should be about  $\lambda/4$  deep although slightly deeper slots provide the proper impedance boundary conditions approximately. To avoid impedance mismatch at the throat of the horn (circular waveguide part) the corrugation next to the waveguide input can be cut  $\lambda/2$  deep. By tapering the next ten slotted corrugations from  $\lambda/2$  to  $\lambda/4$  in equal increments the waveguide mode transition from  $TE_{11}$  mode to the conical horn  $HE_{11}$  mode can be done without significant reflection back into the waveguide.

Referring to Fig. 3.10 slot dimensions are obtained from the iterative equations:

$$\begin{aligned}
 (5.1) \quad A_{1n} &= d_0 + (N-n) 2 (s+w) \tan \theta, \\
 A_{2n} &= A_{1n} + 2s \tan \theta, \\
 A_{3n} &= A_{2n} + 2d_n \\
 A_{4n} &= A_{1n} + 2d_n
 \end{aligned}$$

$n$  is the Fin number starting from the mouth of the horn. The diameters  $A_{1n}$ ,  $A_{2n}$ ,  $A_{3n}$  and  $A_{4n}$ , as shown in Fig. 3.10 give the dimensions needed for turning the lathe and cutting the slots from the aluminum stock.

$S_n = (s+w)(n-1)$  is the axial length from the front surface of the  $n^{\text{th}}$  fin to the horn aperture. For the demonstration model conical corrugated horn the dimensions are:

$$\begin{aligned}
 N &= 108 \text{ total number of fins (numbered from mouth by } n) \\
 d_0 &= 2.062 \text{ cms (0.812") (} A_1 \text{ for fin \# 108)} \\
 s &= 0.152 \text{ cms (.060") fin width, all slots} \\
 w &= 0.508 \text{ cms (0.200") slot width, all slots} \\
 d_n &= 0.635 \text{ cms (0.250") slot depth; except that } d_{108} \text{ is} \\
 &\quad 1.067 \text{ cms (0.420") and each slot from slot 108 to} \\
 &\quad \text{slot 98 is linearly reduced in depth by a decrement} \\
 &\quad \text{of 0.043 cms (0.017") such that slot 98 is 0.635 cms} \\
 &\quad \text{(0.250") deep. All other slots for } n < 98 \text{ are} \\
 &\quad d = 0.635 \text{ cms (0.250") deep.}
 \end{aligned}$$

Table 5.1 gives principal corrugation dimensions near the horn aperture and near the horn throat. Detailed drawings and computer printouts were provided Chu Associates for the horn construction.

### 3.6 Theoretical Diffraction Patterns of Antenna Fed by the Corrugated Conical Horn.

In this section we describe the calculation of the diffraction pattern and efficiency of a paraboloidal antenna with a 121.91 cm radius circular projection illuminated by a 76.2 cm, 12° corrugated horn using an offset ellipsoidal subreflector. The calculation is a four-step procedure:

- 1) calculate the near field pattern of the 76.2 cm, 12° corrugated horn;
- 2) perform a least squares polynomial fit of the amplitude and phase of the near field horn pattern;
- 3) use a geometrical transformation to relate points on the circular aperture projection of the paraboloidal antenna to the near field of the 76.2 cm, 12° corrugated horn and calculate the illumination function of the circular aperture projection;
- 4) calculate the diffraction pattern and efficiency of the circular aperture.

The first step, the calculation of the near field horn pattern, has been described in detail in Section 3.4. The second step, the least square polynomial fit, was performed by assuming a representation of the amplitude (in dB),  $A$ , and phase,  $P$ , (in radians) of the near field horn pattern in terms of even powers of the angle,  $\theta$ , from the horn axis (in radians). A close fit was obtained with the following representations:

$$(6.1) \quad A = c_1 \theta^2 + c_2 \theta^4 + c_3 \theta^6 + c_4 \theta^8$$

$$(6.2) \quad P = D_1 \theta^2 + D_2 \theta^4 + D_3 \theta^6 + D_4 \theta^8 + D_5 \theta^{10}$$

where

$$\begin{aligned} c_1 &= -0.3523467522 \times 10^3 \\ c_2 &= 0.1927249512 \times 10^3 \\ c_3 &= -0.2212143832 \times 10^6 \\ c_4 &= 0.3749071740 \times 10^7 \end{aligned}$$

and

$$\begin{aligned} D_1 &= -0.1452520134 \times 10^2 \\ D_2 &= 0.3247243413 \times 10^4 \\ D_3 &= -0.2021168420 \times 10^6 \\ D_4 &= 0.4393230126 \times 10^7 \\ D_5 &= -0.3484023671 \times 10^8 \end{aligned}$$

The geometrical transformation relating points on the 121.92 cm (48") radius circular aperture projection of the paraboloidal reflector to the angular coordinates of the horn is

$$(6.3) \quad X_A = -B \tan \frac{\Theta}{2} \cos \phi$$

$$(6.4) \quad Y_A = -B \tan \frac{\Theta}{2} \sin \phi$$

where

$X_A, Y_A$  = coordinates of a point on the circular aperture in inches referred to the center of the circular aperture

$\Theta$  = angle from the horn axis

$\phi$  = azimuthal horn angle

$B = 4979.107415$

from (6.3) and (6.4), it follows that

$$X_A^2 + Y_A^2 = B^2 \tan^2 \frac{\Theta}{2}$$

$$\tan \frac{\Theta}{2} = \frac{(X_A^2 + Y_A^2)^{1/2}}{B}$$

and

$$\Theta = 2 \tan^{-1} \left\{ \frac{(X_A^2 + Y_A^2)^{1/2}}{B} \right\}$$

so that the illumination at a point on the circular aperture depends only on the distance  $r$  of the point from the center of the aperture. Given this distance we calculate

$$\Theta = 2 \tan^{-1} \left( \frac{r}{B} \right)$$

and then find the amplitude and phase of the illumination at the point using (6.1) and (6.2). The amplitude pattern across the dish is shown in Fig. 3.11. This radial distribution is seen to be very similar to ideal functions of section 3.3.

The last step, that of calculating the diffraction pattern and efficiency, has already been described above in Section 3 when we discussed the calculation of diffraction patterns and efficiencies of circular apertures with radial illumination functions.

The theoretical far field diffraction patterns of the antenna as calculated by the above procedure are shown in Figs. 3.12 and 3.13. Fig. 3.12 gives the pattern when the phase error is neglected, and Fig. 3.13 shows the pattern when the phase error is included in the illumination function. The corresponding efficiencies are included in Table 3.1.

### 3.7 Correcting for Center-of-Phase Change on the Corrugated Conical Horn

Ideally the phase vs angle curve shown in Fig. 3.9 would be flat; that is, horn phase  $\Delta\phi = 0$  (horn phase is relative phase shift on a spherical surface,  $R_1 = 120.65$  cms (47.5"), centered at the apex of the horn) for  $\theta = 0^\circ$  to  $\theta = 12^\circ$  ( $\theta$  is the spherical polar angle). We want a true spherical phase front from the horn to be incident on the ellipsoidal subreflector surface such that in a geometrical optics sense all rays reflected by the subreflector will pass through  $F_0$  and spread over the aperture of the main reflector to yield the ideal (phase error free) diffraction pattern of Fig. 3.12.

But the results shown in Fig. 3.9 as obtained from the near zone analysis of Section 3.4 indicate a phase error (a departure from a flat HORN PHASE curve) which can be considered as a shift of the horn phase center from the horn apex toward the subreflector as the polar pattern angle  $\theta$  is increased from  $\theta = 0^\circ$ . The phase errors in the conical horn pattern are, in general, small and only for  $\theta > 9^\circ$  are the phase errors significant. At the edge of the horn pattern,  $\theta = 12^\circ$ , the total scalar phase error is only about  $48^\circ$  or  $\lambda/7.5$ . This scalar phase error causes a pattern deterioration shown in Fig. 3.13. The deterioration in the pattern will be somewhat more than that shown, however, because the change in phase shift at the edge of the horn pattern occurs in a small angular region. The rapid change in phase means that the edge rays which are vectors change directions significantly effecting both the aperture amplitude distribution and the aperture phase errors. The main effect of these vector changes is to increase the amplitude taper on the main reflector decreasing the aperture efficiency somewhat and lowering side-lobes slightly.

The first step in correcting for the horn phase errors is to transform the near zone phase pattern (Fig. 3.9) obtained numerically by the involved diffraction computations of Section 3.4 into a spatial distribution of rays referred to spherical surface. We are interested primarily in this ray field near the edges of the illuminated portion of the subreflector. For the demonstration model a radial distance of 120.65 cms from the horn apex was chosen which is on the subreflector rim at 2 regions for  $\theta = 12^\circ$  the horn semiflare angle.

To compute a set of discrete rays representing the  $\Delta\phi$  error data on the 120.65 cm radius the numerically tabulated phase error vs  $\theta$  angle values need to be approximated by a continuous function. Using data plotted in Fig. 3.9 a continuous curve in the form of a polynomial (useful for ray studies) was selected

$$(7.1) \quad \Delta\phi = B_0 + B_2\theta^2 + B_4\theta^4 + B_6\theta^6$$

and a regressional fit using standard analytical techniques<sup>(28)</sup> used for a "best" least squares fit to 15 numerically computed points. When the phase shifts  $\Delta\phi$  and polar angles  $\theta$  are expressed in radians we obtained the polynomial coefficients.

$$(7.2) \quad B_0 = -0.0055349, \quad B_2 = 1.646679, \quad B_4 = 92.796739 \\ B_6 = 1.3301.82652$$

This continuous curve approximation is plotted in Fig. 4.3 with dots labelled regressional fit.

To obtain a spatial distribution of ray directions expressed in spherical coordinates,  $r, \theta, \phi$ , crossing the spherical cap  $R_1 (= 47.5")$  we assume a congruence of rays propagating over all space as TEM waves and that

$$(7.3) \quad \Delta\Phi(\theta) = \frac{2\pi}{\lambda} \Delta r(\theta) = k \Delta r(\theta)$$

$$\text{where } k = \frac{\lambda}{2\pi} = 0.397891 \quad (12 \text{ GHz})$$

The  $\Delta r$  displacement then from the spherical cap  $R_1 = 120.65$  cms (47.5") (always assuming no variations with the spherical angle  $\phi$ ) is

$$(7.4) \quad k \Delta\Phi = \Delta r(\theta) = r(\theta) - R_1$$

Defining a function  $\psi = 0 = r(\theta) - R_1 - k \Delta\Phi(\theta)$ , we can write normals to this surface of ray directions as

$$(7.5) \quad \hat{n} = \nabla\psi = \frac{\partial\psi}{\partial r} \hat{r} + \frac{1}{r} \frac{\partial\psi}{\partial\theta} \hat{\theta} + \frac{1}{r \sin\theta} \frac{\partial\psi}{\partial\phi} \hat{\phi}$$

$$(7.6) \quad \hat{n} = \hat{r} - \frac{1}{r} \frac{\partial(k \Delta\Phi)}{\partial\theta} \hat{\theta}$$

$$(7.7) \quad \hat{n} = a_1 \hat{r} + a_2 \hat{\theta} + a_3 \hat{\phi}$$

$$(7.8) \quad r' = k \frac{\partial\Delta\Phi}{\partial\theta} = \frac{\partial r}{\partial\theta}$$

$$(7.9) \quad \text{Then } a_1 = \frac{1}{\sqrt{1 + \left(\frac{r'}{r}\right)^2}}, \quad a_2 = \frac{-r'}{r \sqrt{1 + \left(\frac{r'}{r}\right)^2}}, \quad a_3 = 0$$

To express  $\hat{n}$  the ray directions in rectangular coordinates  $x, y, z$  with origin at  $F_1$ , we write

$$(7.10) \quad \begin{aligned} x &= r \sin\theta \cos\phi \\ y &= r \sin\theta \sin\phi \\ z &= r \cos\theta \end{aligned}$$

Then the direction cosines of the ray are

$$(7.11) \quad \begin{aligned} l &= a_1 \sin \theta \cos \phi + a_2 \cos \theta \cos \phi \\ m &= a_1 \sin \theta \sin \phi + a_2 \cos \theta \sin \phi \\ n &= a_1 \cos \theta - a_2 \sin \theta \end{aligned}$$

This family of rays can be expressed as straight lines

$$(7.12) \quad \begin{aligned} x &= k_x z + \epsilon_x \\ y &= k_y z + \epsilon_y \end{aligned}$$

where

$$(7.13) \quad \begin{aligned} k_x &= l/n \\ \epsilon_x &= \frac{l}{n} (-z + C_2) + x \end{aligned}$$

$$(7.14) \quad \begin{aligned} k_y &= m/n \\ \epsilon_y &= \frac{m}{n} (-z + C_2) + y \end{aligned}$$

When  $\epsilon_x$  and  $\epsilon_y$  are zero the lines (rays) pass through the focus,  $F_1$ , and the phase center is at the apex of the horn

$C_2$  is the distance along the z-axis which makes  $\epsilon_x$  and  $\epsilon_y$  zero and  $C_2$  is therefore the shift of the phase center toward the subreflector for a discrete ray passing through a point  $x, y, z$  on the spherical surface  $R_1$ .

For the analysis and shaping synthesis to follow  $C_2$  was set to zero and the values  $\epsilon_x$  and  $\epsilon_y$  represent the z-plane intercepts of the lines. The lines carry the information on magnitude and direction of the phase errors in the horn phase pattern. Each ray as a line is stored in the computer by four numbers,  $k_x, k_y, \epsilon_x, \epsilon_y$ . This 4-element array of numbers for each discrete line provides a 3-coordinate vectorial representation of the equiphase surface  $r(\theta)$  near  $R_1 (= 47.5")$  which surface nearly touches the ellipsoidal subreflector near the edges of the illuminated sector at maximum values of  $|x|$ .

#### Methods for Correcting Horn Phase Errors

Three methods for correcting the horn phase errors were investigated: (1) refocusing the horn by moving it forward to redistribute the phase errors; (2) changing the eccentricity of the subreflector to bring the horn edge rays to the edge of the main reflector (after reflection by the subreflector); and (3) reshaping the subreflector to bring all rays to focus at  $F_0$ .

The first means for correcting phase errors, by refocusing, is illustrated in Fig. 3.14 wherein the horn was moved forward 76.2 cms so  $R_1 = R_2 = 113$  cms. It is seen that the aperture phase error distribution has shifted to give larger phase errors

at lower values of  $\theta$  and smaller phase errors at  $\theta = 12^\circ$ . Because the horn amplitude pattern is greater at small values of  $\theta$ , the new phase error distribution will cause more pattern deterioration than the original phase errors when the horn apex is located near the focus  $F_1$ .

In order to refocus analytically the phase error or path length error distribution, we again use the equiphase surface function

$$(7.15) \quad r(\theta) = R_1 + \Delta r(\theta) = R_1 + k \Delta \Phi(\theta)$$

where  $R_1 = 120.65$  and  $k = 0.3978874$

To find the phase error distribution at  $z = C_2 = 7.62$  cm we write

$$(7.16) \quad r'(\theta') = R_2 + k \Phi'(\theta')$$

where  $R_2 = 113$  cm and the primes indicate the transformation of coordinates to  $z = 7.62$ . Using polar coordinates in the x-z plane to locate a point on the equiphase surface, we write

$$\begin{aligned} x &= r \sin \theta && \text{For origin at } F_1 \\ z &= r \cos \theta \\ x' &= r' \sin \theta' && \text{For origin at } z = 7.62 \text{ cm} \\ z' &= r' \cos \theta' && x = 0 \\ z' + C_2 &= z && \\ x' &= x && \tan \theta' = x' / z - C_2 \end{aligned}$$

$$\text{so} \quad \begin{aligned} r'(\theta') &= (z - C_2) / \cos \theta' \\ \tan \theta' &= x' / z - C_2 \end{aligned}$$

$$\frac{r' - R_2}{k} = \Phi'(\theta') \quad \text{radians phase error at } \theta'.$$

Based on these results only a minor amount of refocusing appears to be desirable for improving the main dish radiation patterns.

Increasing the Eccentricity of Ellipsoidal Subreflector as Means for Correcting Horn Phase Errors:

The "creep" of horn phase center forward with large values of  $\theta$  and especially at the edge of the horn pattern ( $\theta_1 = 12^\circ$ ) results in a redistribution of the aperture amplitude distribution because the horn's edge rays are directed toward the center of the dish as shown in Fig. 3.15. This effect is due to the change of ray directions near the edge of the horn pattern.

We can in theory always reflect the horn edge rays to the edge of the circular dish aperture with radius  $R = 121.92$  cms

by increasing the value of  $e$  for the ellipsoidal subreflector. We can do this and still design a feed system (with horn semi-flare angle  $12^\circ$ ) according to the Japanese tilt angle criteria for low cross polarization and true beam symmetry. However, such an approach does not reduce the aperture phase errors and results in a new and less than ideal aperture amplitude distribution on the dish.

To understand why change in  $e$  changes the main dish aperture amplitude distribution when illuminated by a given horn consider Fig. 3.3. For the  $12^\circ$  horn and a subreflector with  $e = 0.538$  the feed just illuminates to the dish edges  $R=x=121.92$  cms on the  $x-z$  diagram when horn has no phase errors. The edge ray shown striking the  $e = .538$  subreflector has phase errors causing ray to strike dish at about  $x = 93.98$  cms point, not  $x = 121.92$  cms. Assuming now that all subreflectors are made "oversize" to allow for scanning by feed motion and to reduce spillover around the subreflector edges.

When the subreflector eccentricity is increased to  $e = 0.6$  a  $9.93^\circ$  semiflare angle horn (no phase errors) with point of phase at  $F_1$  is all that would be needed to illuminate the  $R = 121.92$  cms radius dish. If a  $12^\circ$  horn (no phase errors) is used to feed the  $e = 0.6$  subreflector then a larger subreflector surface and larger main reflector surface ( $R > 121.92$  cms) are illuminated. However, if the  $12^\circ$  horn has phase errors (center of phase moving in  $+z$  direction) then the large value of  $e = .6$  results in the edge ray striking near the edge of the main reflector as shown in Fig. 3.15.

To quantify these effects rays from the demonstration model horn must be traced onto Japanese optimized subreflectors of different  $e$ . This can be done using an interpolation function,  $G_i$ , to find where the horn rays intersect the subreflector surfaces.

$$(7.17) \quad \begin{aligned} G_{xi} &= k_{xi} z_n + \epsilon_{xi} - x_n \\ G_{yj} &= k_{yj} z_n + \epsilon_{yj} - y_n \end{aligned}$$

From the (ray) line values  $G_{xi}$ ,  $\epsilon_{xi}$ ,  $k_{yj}$ ,  $\epsilon_{yj}$ , the points of surface intersection  $x_n$ ,  $y_n$ ,  $z_n$  can be located which make  $G_{xi}$  and  $G_{yj}$  go to zero.

After considerable effort this correction procedure was abandoned because (1) aperture phase errors are not corrected and (2) the dish amplitude distribution is even more tapered with  $e = .60$  than for  $e = 0.538$ .

It should be observed that although refocusing the horn and increasing the subreflector eccentricity do not adequately

correct for horn phase errors, an ellipsoidal subreflector with slightly larger  $e$  than for a true point source horn and a slight forward focusing motion of the horn should improve the antenna pattern performance somewhat.

### 3.8 Subreflector Shaping Technique to Correct for Horn Phase Errors

In order to correct the phase errors for both scalar and vector effects and maintain near to ideal aperture distributions on the main reflector, it was decided to shape the subreflector such that the field of rays representing the near-field radiation pattern of the horn are focused to  $F_0$ . This shaping synthesis of the subreflector results in a surface that is not truly ellipsoidal except for a small reference region (a Japanese optimized reference ellipsoid) near to the mid-point of the subreflector,  $\theta = 0^\circ$ . Because the horn phase errors are very small out to  $\theta = 8^\circ$  the shaped central region of the subreflector is nearly ellipsoidal over a large central region of the subreflector. Also a rim section was added around the edge of the demonstration model for scanning a  $3^\circ$  cone by horn motion. This rim section is also part of the reference ellipsoid.

To achieve the desired phase-error-free dish aperture distribution, hopeful to realize the ideal amplitude needed to get pattern shown in Fig.3.12, a technique is now described that will focus the near zone pattern of the horn to  $F_0$  by shaping the subreflector surface. This surface synthesis method uses the discrete set of ray-lines with parameters  $G_x, \epsilon_x, k_y, \epsilon_y$  to represent the near zone pattern of the horn. With the horn apex at  $F_1$  a reference ellipsoid is defined with  $e = 0.538$  and  $c = 88.9$  cms.

To compute the set of discrete rays carrying the phase errors of the horn, lines passing through a sphere with  $x, y, z$  points on the  $R = 120.65$  cms surface spaced about 2.54 cms apart are used and the corresponding  $k_x, \epsilon_x, k_y, \epsilon_y$  values stored in computer memory are obtained from equations 7.13 and 7.14.

To start the numerical shaping synthesis of the subreflector surface a grid of subreflector surface points  $x, y, z$  spaced 0.25 cms apart in  $x$  and  $y$  are computed for the reference ellipsoid in a small region about the central zone ( $\theta = 0^\circ$ ) of the subreflector. These surface points are correct because the horn pattern has almost zero phase errors for  $\theta \approx 0^\circ$ . These surface points in this central region of the subreflector are used as start-up data in a computer synthesis procedure. Generally Adam's projector is used for synthesis which requires

3 back slopes to project to new points, that is for x cuts:

$$(8.1) \quad Z_{n+1} = Z_n + \frac{\Delta x}{24} \left( 55 \frac{\partial Z}{\partial x} \Big|_n - 59 \frac{\partial Z}{\partial x} \Big|_{n-1} + 37 \frac{\partial Z}{\partial x} \Big|_{n-2} - 9 \frac{\partial Z}{\partial x} \Big|_{n-3} \right)$$

With a similar equation for y cuts by replacing  $\Delta x$  with  $\Delta y$  and  $\frac{\partial Z}{\partial x} \Big|_i$  with  $\frac{\partial Z}{\partial y} \Big|_j$ .

The reference ellipsoid has the surface and slopes based on the Japanese optimized tilts and :

$$(8.2) \quad x^2 + y^2 + z^2 = e^2 (z \cos \alpha - y \sin \alpha + d)^2$$

$$\begin{aligned} d &= 109.1202934'' \\ \alpha &= 17.046130631^\circ \\ \beta &= 5.14239^\circ \end{aligned}$$

for the reference surface.

$$(8.3) \quad \frac{\partial z}{\partial x} = \frac{-\frac{x}{e^2}}{\frac{z}{e^2} - \cos \alpha (z \cos \alpha - y \sin \alpha + d)}$$

$$\frac{\partial z}{\partial y} = \frac{-\left(\frac{y}{e^2} + z \sin \alpha \cos \alpha - y \sin \alpha + d\right)}{\frac{z}{e^2} - \sin \alpha (z \cos \alpha - y \sin \alpha + d)}$$

for the reference surface slopes.

Numerical shaping of the subreflector is first done along 4 x-cuts (x-z plane) spaced 0.254 cms (0.1") apart in y at 0.254 cms (0.1") intervals in  $\Delta x$ . Beginning at the edge of the small central section the back partial derivatives and surface values from the central section (reference ellipsoid) are substituted into Adam's projector at the start of each x-cut. Because of the left-right symmetry of the offset antenna only + x cuts need to be computed out to about  $x = 25.4$  cms (10"). Equation 8.1 projects us to a new point  $x_{n+1}$ ,  $y_{n+1}$ ,  $z_{n+1}$ , where we use Snell's law to calculate surface slopes, using the discrete rays from the conical horn, such that the incremental surface at  $P_n$  and  $P_{n-1}$  has a normal  $\hat{n}$  that satisfies

$$(8.4) \quad \hat{S}_2 = \hat{S}_1 - 2(\hat{S}_1 \cdot \hat{n})\hat{n}$$

$\hat{S}_1$  is a ray from the horn (phase error) pattern incident on the point  $P_n(x_n, y_n, z_n)$ . But we have stored in computer memory only a discrete set of lines representing the horn phase pattern. To obtain the ray passing through  $P_n$  we must interpolate from the discrete family of lines using Eq. 7.17. We substitute the ray values  $G_{xi}$ ,  $\epsilon_{xi}$ ,  $k_{yj}$ ,  $\epsilon_{yj}$  into (7.17) until the  $G_{xi}$  and  $G_{yj}$  values change signs indicating that a known

discrete line passed near the surface point  $P_n$ . We store both the + and - values of  $G_{xi}$  (and  $G_{yi}$ ) and using these we interpolate to find the "true" values of  $k_{xt}$  and  $k_{yt}$  for the ray intersecting  $P_n$  using expressions:

$$(8.5) \quad F_1 = \frac{G_{x(+)} - G_{x(-)}}{G_{x(+)} - G_{x(-)}} \quad ; \quad F_2 = \frac{G_{y(+)} - G_{y(-)}}{G_{y(+)} - G_{y(-)}}$$

$$(8.6) \quad k_{xt} = k_{x(+)} - F_1 (k_{x(+)} - k_{x(-)})$$

$$k_{yt} = k_{y(+)} - F_2 (k_{y(+)} - k_{y(-)})$$

$$\hat{S}_1 = \frac{k_{xt} \hat{x} + k_{yt} \hat{y} + \hat{z}}{\sqrt{k_{xt}^2 + k_{yt}^2 + 1}} = a_1 \hat{x} + b_1 \hat{y} + c_1 \hat{z}$$

Having found  $\hat{S}_1$  to high accuracy by this interpolation procedure we solve for  $\hat{n}$  at the surface value at  $P_n$  by using equation (8.4). We want to reflect all rays off the shaped subreflector to  $F_0$  which for the coordinates system with origin at  $F_1$  is the point:

$$x_0 = 0$$

$$y_0 = c \sin \alpha$$

$$z_0 = c \cos \alpha$$

We can write the reflected ray  $\hat{S}_2$  as:

$$(8.7) \quad \hat{S}_2 = \frac{x_n \hat{x} + (y_0 - y_n) \hat{y} + (z_0 - z_n) \hat{z}}{[x_n^2 + (y_0 - y_n)^2 + (z_0 - z_n)^2]^{1/2}}$$

$$\hat{S}_2 = a_2 \hat{x} + b_2 \hat{y} + c_2 \hat{z}$$

We can invert (8.4) given  $S_1$  and  $S_2$  to find

$$\hat{n} = a_N \hat{x} + b_N \hat{y} + c_N \hat{z} \quad \text{from}$$

$$(8.9) \quad a_N = \frac{(a_1 - a_2)}{T_3} \quad ; \quad b_N = \frac{(b_1 - b_2)}{T_3} \quad ; \quad c_N = \frac{(c_1 - c_2)}{T_3}$$

$$T_3 = 2 [1 - (a_1 a_2 + b_1 b_2 + c_1 c_2)]^{1/2} \quad \text{and}$$

(8.10)

$$\left. \frac{\partial z}{\partial x} \right|_n = -\frac{a_N}{c_N} \quad , \quad \left. \frac{\partial z}{\partial y} \right|_n = -\frac{b_N}{c_N}$$

are the new partial derivatives for the extrapolation to the next point on  $Z_{n+1}$  in Eq. (8.1).

Using this procedure the 4 x-cuts are calculated for every 0.254 cms in x and values at 1.27 cms intervals in x are computer stored for use in computing y-cuts for both +y and -y directions to complete the templet curves needed to construct the surface of the shaped subreflector.

The stored values along the 4 x plane cuts separated by 0.254 cms (0.1") y and 1.27 cms x intervals serve to provide the start-up (back partial derivatives) and surface coordinate values for the same interpolation-extrapolation procedure already described for the y-cuts. A slightly different program is needed to go along the +y cuts than the -y cuts. Again surface coordinate points along the y direction are made at 0.254 cms intervals and points stored every 1.27 cms. Actually, the every 0.254 cms data is printed out along with computer graphics to aid in construction of the subreflector.

In Fig. 3.16 a cross section through the subreflector on a center cut displaced 0.254 cms from the y axis. The subreflector contour is very nearly that of an ellipsoid tilted  $5.14^\circ$  from the paraboloid axis. Only the subreflector portion near the small steps is shaped, with the surfaces near  $y = 0$  and the outer edge portion or skirt being true ellipsoids. In Fig. 3.17 a front view of the Gregorian subreflector is shown indicating where several y-cut templates are located. These templates are located every 1.27 cms apart in x direction and provide means for constructing the shaped reflector which is not exactly an ellipsoid of revolution.

### 3.9 Finding the Best Focal Curves

The method reported here can find three focal surfaces of interest for: best azimuth plane patterns, best elevation plane patterns, and compromise patterns lying at focal points between the tangential and sagittal foci. Techniques in references (4) and (28) have been extended here to include general scanning data on offset dual reflectors and a diffraction method to compute antenna far field patterns on scanned beams is developed in the next section.

The analytic steps needed to find the focal loci begin by tracing a congruence of received rays representing a plane wave tilted with respect to the paraboloid axis. These rays are incident upon the main reflector surface, an offset paraboloidal section with circular aperture, and reflected on to an elliptical (or hyperboloidal) subreflector surface which is confocal with the paraboloid. Tracing the circular edge of the main dish onto the subreflector gives a "footprint" which establishes the subreflector's borders for scanning angular sectors of interest and locates the point on the subreflector for pointing the axis of the horn. The central received ray incident on the

mid-point,  $Y_c$ , (see Fig.3.18) of the main paraboloidal section also intersects the point M on the subreflector for the given scan angle. This central ray also defines the horn or feed axis on which the best focal points are approximately located. The ray tracing technique for finding the best focal surfaces sets up a flat "screen" normal to the horn axis on which is displayed by computer graphics traces of the dish edge rays. The screen is analytically moved back and forth along the horn axis and traces or curves formed by the intersection of the dish edge rays as they converge on the screen are observed. These curves become approximately lines for best azimuth or elevation focusing and approximately circles for the compromise or circle of least confusion focal locus. Although the incident rays reflected from the circular edge contour of the main dish are generally traced, smaller circles on the dish should also be traced to get a more complete picture of the optical focusing characteristics.

### 3.9.1 Mathematical Development

The following equations can be used for symmetric or offset antennas fed by either hyperboloidal or ellipsoidal subreflectors. Consider the rectangular coordinate system shown in Fig. 3.18. In it the paraboloidal section reflecting surface is given by

$$(9.1) \quad x^2 + y^2 = 4f(f-z)$$

Where for numerical data and charts presented,  $f = 177.8$  cms. The rim of the circular paraboloidal section was offset 35.56 cms above the z-axis such that the center point of this dish is at  $x_c = 0$ ,  $y_c = 157.48$  cms,  $z_c = 142.92834$  cms. The circular edge of the 8-ft. diameter main reflector is given by

$$(9.2) \quad \begin{aligned} y &= y_c + R \sin \theta \\ x &= R \cos \theta \end{aligned}$$

$$\text{where } R = 121.92 \text{ cm and } 0^\circ \leq \theta \leq 180^\circ$$

The ellipsoidal subreflector surface is given by the expression

$$(9.3) \quad x_1^2 + (y_1 - h)^2 + (z_1 - k)^2 = e^2 ((z_1 - k) \cos \beta - (y_1 - h) \sin \beta + d_0)^2$$

Where  $h$  and  $k$  are small displacements of the ellipsoid from the confocal point  $F$  due to mechanical misalignment of the subreflector, for example, and are usually set at zero. For the numerical case and eccentricity studied  $d_0 = 109.1202923$  cms, axis of ellipsoidal tilt  $\beta = 5.14239^\circ$ , and eccentricity  $e = 0.538$ . (When  $d_0$  is negative in (9.3) and the eccentricity,  $e$ , is greater than 1.0, then the surface is a hyperboloid.) To find the edges of the ellipsoidal subreflector the largest

elevation angle,  $\alpha$ , and azimuth angle,  $\phi$ , required to scan the main beam over sectors of interest are introduced in (9.4) below and the edges of the subreflector found by ray tracing the "footprints" of the rim of the circular paraboloidal section onto the ellipsoidal surface.

The rays  $\hat{S}_0$  in the parallel bundle of incident (received) rays representing a plane wave tilted by  $\alpha$  and  $\phi$  with respect to the z-axis can be written as

$$(9.4) \quad \begin{aligned} \hat{S}_0 &= \cos \alpha \sin \phi \hat{x} - \sin \alpha \hat{y} + \cos \alpha \cos \phi \hat{z} \\ \hat{S}_0 &= l_0 \hat{x} + m_0 \hat{y} + n_0 \hat{z} \end{aligned}$$

Unit vectors normal to the paraboloid surface are given by:

$$(9.5) \quad -\hat{n} = \frac{x \hat{x} + y \hat{y} + 2f \hat{z}}{(x^2 + y^2 + 4f^2)^{1/2}}$$

The rays  $\hat{S}_1$  reflected from the paraboloid surface in the general direction of F are given by Snell's Law

$$(9.6) \quad \hat{S}_1 = \hat{S}_0 - 2(\hat{S}_0 \cdot \hat{n}) \hat{n} = l_1 \hat{x} + m_1 \hat{y} + n_1 \hat{z}$$

Substituting (9.4) and (9.5) into (9.6)

$$(9.7) \quad \begin{aligned} l_1 &= \cos \alpha \sin \phi - R_1 x \\ m_1 &= -\sin \alpha \hat{y} - R_1 y \\ n_1 &= \cos \alpha \cos \phi - R_1 2f \end{aligned}$$

where

$$R_1 = \frac{2(x \cos \alpha \sin \phi - y \sin \alpha + 2f \cos \alpha \cos \phi)}{(x^2 + y^2 + 4f^2)}$$

and  $x, y, z$  are coordinates of points on the paraboloid surface where  $\hat{S}_0$  is incident. The ray  $S_1$  can be written as a line (9.8) extending from the paraboloid point  $x, y, z$  to an intersection point on the ellipsoid

$$(9.8) \quad \frac{x_1 - x}{l_1} = \frac{y_1 - y}{m_1} = \frac{z_1 - z}{n_1}$$

Equations (9.7), (9.8), and (9.3) are solved simultaneously to find the intercept points  $P_1(x_1, y_1, z_1)$  on the ellipsoid. The unit normal  $\hat{n}_1$  on the ellipsoid can be calculated analytically at any point on its surface. Therefore we can write, again using Snell's Law of Reflection, the vector  $\hat{S}_2$  reflected from

the subreflector toward the focal surfaces we wish to find

$$(9.9) \quad \hat{S}_2 = \hat{S}_1 - 2(\hat{S}_1 \cdot \hat{n}_1)\hat{n}_1 = l_2 \hat{x} + m_2 \hat{y} + n_2 \hat{z}$$

$$l_2 = R_0 x_1 + l_1$$

$$m_2 = m_1 - R_0 (e^2 C_5 \sin \alpha + y_1 - h)$$

$$n_2 = n_1 - R_0 (z_1 - h - e^2 C_5 \cos \alpha)$$

where

$$C_5 = (z_1 - h) \cos \alpha - (y_1 - h) \sin \alpha + d_0$$

$$R_4 = 2(l_1 x_1 + m_1 (y_1 - h + e^2 C_5 \sin \alpha)) + n_1 (z_1 - h - e^2 C_5 \cos \alpha)$$

$$R_5 = x_1^2 + (y_1 - h + e^2 C_5 \sin \alpha)^2 + (z_1 - h - e^2 C_5 \cos \alpha)^2$$

$$R_0 = R_4 / R_5$$

Having started with a parallel bundle of received rays  $\hat{S}_0$  incident on the main reflector aperture, our ray tracing has given us  $\hat{S}_2$  representing a converging congruence of rays reflected from the subreflector that focus more or less on a focal surface. The initial ray traced then for an incident plane wave tilted  $\vartheta$  and  $\phi$  is, therefore, the central ray in order to set up a "screen" perpendicular to the convergent ray bundle axis. It is on this screen then that all the rays of interest (especially the rays from the rim of the dish) are traced. The plane screen is analytically moved in and out and the sharpness of focus observed by computer graphics. Denoting this in and out focusing parameter as  $Z_4$  the corresponding focal coordinates,  $x_4$  and  $y_4$ , are computed to lie on the central or axis ray. The initiating procedure is to input a trial value  $Z_4$  and compute the direction cosines of the central ray  $l_3, m_3, n_3$ . We give these central ray parameters the symbols  $l_3, m_3, n_3$  and write

$$(9.10) \quad \tan \frac{m_3}{n_3} = \gamma_1 \quad \text{and} \quad \tan \frac{l_3}{n_3} = \gamma_2$$

where  $\gamma_1$  and  $\gamma_2$  are the orientation angles of the flat screen on which all rays are subsequently traced. Also for  $Z_4$

$$(9.11) \quad x_4 = \frac{l_3}{n_3} (z_4 - z_1) + x_1$$

$$y_4 = \frac{m_3}{n_3} (z_4 - z_1) + y_1$$

$$D_3 = -(l_3 x_4 + m_3 y_4 + n_3 z_4)$$

In order to plot all the other rays in the converging bundle on the screen these intercept points are calculated from

$$(9.12) \quad z_0 = \frac{\left( \frac{l_3 l_2 z_1}{n_2} + \frac{z_1 m_3 m_2}{n_2} - (D_3 + l_3 x_1 + m_3 y_3) \right)}{\left( n_3 + \frac{l_3 l_2}{n_2} + \frac{m_3 m_2}{n_2} \right)}$$

$$x_0 = \frac{l_2}{n_2} (z_0 - z_1) + x_1; \quad y_0 = \frac{m_2}{n_2} (z_0 - z_1) + y_1$$

Finally, to plot the perpendicular displacements of the rays focused on the screen relative to the focal point of the central ray, we write:

$$(9.13) \quad x_s = (x_0 - x_u) \sec \delta_2$$

$$y_s = (y_0 - y_u) \sec \delta_1$$

For the 2.44 meter dish fed by the Gregorian subreflector, the best focal curve for  $+3^\circ$  elevation plane (2) scanning is shown in Fig. 3.18. This focal curve is for sharpest pattern nulls in the azimuth (x-z plane) cuts. Examples of computer graphics of the type used to determine focal surfaces is shown in Figs. 3.19A, B, and C. In Fig. 3.19A the direction of the beam from the z axis direction is inclined about  $\theta = 3^\circ$ , ( $\varphi = 0^\circ$ ) in azimuth angle. The focal points  $X_F, Y_F, Z_F$  as given on the graphics for best azimuth focus, best elevation angle focus and best compromise focus. The graphic traces are for rim rays, that is,  $R = 121.92$  cm. Note that the curves are shifted from the center ray axis at  $x_0 = 0, y_0 = 0$  which indicates a slight shift of the beam direction from  $\theta = 3^\circ$  ( $\varphi = 0^\circ$ ). The edge ray traces are shown in Fig. 3.19B for a beam direction of approximately  $\varphi = 3^\circ$  in elevation angle. Fig. 3.19C shows diagonal traces corresponding to beam direction at  $\varphi = 2^\circ$  and  $\theta = 2^\circ$ . The size of the rim traces indicate qualitatively the maximum phase errors or optical aberrations. These  $X_0, Y_0$  plots are given in inches. When all focal points  $X_F, Y_F, Z_F$  are plotted in an X,Y plane, focal surfaces for elevation angle, azimuth angle and  $45^\circ$  scanning are shown in Fig. 3.20.

Using rim tracing curves as shown in Figs. 3.19A, B, and C, focal surface and "optical beamwidth" data, as shown in Table 9.1, was compiled. Optical beamwidth was defined as the half width of the compromise or circle of least confusion rim trace divided by the focal plane distance  $d$  needed to steer a beam one degree. When this optical beamwidth is less than the diffraction beamwidth ( $\sim \lambda/D$ ), pattern deterioration due to aberrations is not likely to be excessive. This kind of estimation "OPT BW" is given in the last column of Table 9.1. The astigmatic characteristics of dual reflector focusing are evident from Fig. 3.19 and Table 9.1. The feed (horn) center of phase should be located on the focal surface at the focal point for

best azimuth, elevation or compromise focus as required for the application. Also, the feed axis should be pointed to the middle of the foot print which is shown as point M in Fig. 3.21. This is a frontal view of the subreflector ( $x_1 - y_1$  plane) for an azimuth scan angle  $\theta = 4.5^\circ$  ( $\alpha = 0^\circ$ ). The edge angles shown are simply polar angles locating the rim points on the dish.

Wider scan angles or multibeam coverage can be achieved by making the eccentricity,  $e$ , of the ellipsoid larger and, hence, increasing the dual reflector magnification. In Fig. 3.22a comparison is shown of the best focal curves in the  $y-z$  plane for a higher magnification system with  $e = 0.66$  (also a longer focal length to make subreflector sizes comparable and greater than 15 in diameter). At the bottom of Table 9.1 a comparison of optical beamwidths are given for the two subreflectors both feeding the same 2.44 meter offset paraboloid.

### 3.9.2 Computing Diffraction Patterns

#### 3.9.2.1 General Description of Technique

The geometrical optics analysis presented thus far provides design information for locating and scanning feeds on offset dual reflector antennas. In order to quantify sidelobe levels and beamwidths, diffraction patterns (at some wavelength) are needed to verify the optics and to establish scanning limits. Such diffraction diagrams can be computed from the ray path length differences measured from the "best" focal points out to points on a grid on the dish aperture plane. These path length differences,  $\Delta L$ , relative to the central ray path length can be converted to aperture phase errors  $\delta$  for the frequency of interest by  $\delta = 2\pi\Delta L/\lambda$ . It is assumed that the aperture amplitude distribution is the same as for the  $z$ -axis antenna pattern.

To obtain the  $\Delta L$  data for the aperture phase error distribution, the ray tracing procedure described earlier for finding best focal surfaces must be essentially reversed. A regular grid of aperture points is desired for carrying out a Fourier transform of aperture field in computing the far-field patterns. We begin, therefore, by tracing rays incident on a regular grid of aperture points  $x, y, z$  on the paraboloid surface in a receive-mode sense down to the ellipsoid surface and store the points  $x_1, y_1, z_1$  corresponding to these paraboloid points. Then, using a transmit-mode analysis, we connect the points  $x_1, y_1, z_1$  to the "best" focal point  $x_F, y_F, z_F$  chosen for the pattern desired. We calculate the total path length from the focal point, to the subreflector surface, to the paraboloid surface, and out to the aperture plane. (We make the aperture plane the tilted "plane wave" plane used in the receive-mode analysis.) The central ray is again traced first from the focal

point out to the aperture plane and its length recorded as the reference length,  $L_0$ . Then the entire grid of aperture points are traced and the  $\delta$  values found and stored with the amplitude values at each aperture point. This procedure for finding  $\Delta L$  is approximate in that the transmitted rays from  $x_F, y_F, z_F$  do not strike exactly on the paraboloid points chosen as grid points. These errors are usually very small. There is some amplitude distortion also that is negligible for small scan angles.

### 3.9.2.2 Mathematical Steps

The same analytical steps used for finding the ray intercept points  $x_1, y_1, z_1$  on the ellipsoidal subreflector for tilt values  $\alpha$  and  $\beta$  of an incident plane wave can be used again in the diffraction calculations. Equations 9.1, 9.3, 9.7 and 9.8 are needed to find the  $x_1, y_1, z_1$  points. Equation 9.2 is modified to obtain an aperture grid distribution  $x, y, z$  uniformly spaced along radial lines which are rotated by small increments in a polar angle  $\theta$ . To find the path length errors,  $\Delta L$ , we start from the selected focal point  $x_F, y_F, z_F$  and find the length,  $L_1$ , to the subreflector surface

$$(10.1) \quad L_1 = (x_1 - x_F)^2 + (y_1 - y_F)^2 + (z_1 - z_F)^2$$

where

$$\hat{L}_1 = \frac{(x_1 - x_F) \hat{x}}{L_1} + \frac{(y_1 - y_F) \hat{y}}{L_1} + \frac{(z_1 - z_F) \hat{z}}{L_1}$$

$$\hat{L}_1 = l_1 \hat{x} + m_1 \hat{y} + n_1 \hat{z}$$

To find the ray  $\hat{L}_2$  (and its length  $L_2$ ) reflected from the subreflector up to the main reflector write

$$(10.2) \quad \begin{aligned} l_2 &= l_1 - r' x_1 \\ m_2 &= m_1 - r' (y_1 + e^2 D \sin \beta) \\ n_2 &= n_1 - r' (z_1 - e^2 D \cos \beta) \end{aligned}$$

where

$$D = z_1 \cos \beta - y_1 \sin \beta + d_0$$

$$r' = \frac{2(x_1 l_1 + m_1 (y_1 + e^2 D \sin \beta) + n_1 (z_1 - e^2 D \cos \beta))}{x_1^2 + (y_1 + e^2 D \sin \beta)^2 + (z_1 - e^2 D \cos \beta)^2}$$

$$\hat{L}_2 = l_2 \hat{x} + m_2 \hat{y} + n_2 \hat{z}$$

To find the intercept points of the rays  $\hat{L}_2$  on the paraboloidal surface, we solve simultaneously the equations

$$(10.3) \quad \frac{x - x_1}{l_2} = \frac{y - y_1}{m_2} = \frac{z - z_1}{n_2}$$

$$x^2 + y^2 = 4f(f - z)$$

This simultaneous solution gives us the points on the paraboloid  $x, y, z$  which are not quite the same grid points selected in the receive mode for the tilted incident plane wave.

$$(10.4) \quad L_2 = (x - x_1)^2 + (y - y_1)^2 + (z - z_1)^2$$

To complete the path length calculation one must reflect  $L_2$  from the paraboloid surface and find the path length,  $L_3$ , back to the original plane tilted by  $\alpha$  and  $\beta$  with respect to the  $z = 0$  plane.

$$(10.5) \quad \begin{aligned} l_3 &= -2r_3 x + l_2 \\ m_3 &= m_2 - 2r_3 y \\ n_3 &= n_2 - 4r_3 f \\ r_3 &= \frac{l_2 x + m_2 y + n_2 z f}{x^2 + y^2 + 4f^2} \end{aligned}$$

The original plane wave is normal to the ray as given by (9.4).

The coordinates  $(x_{11}, y_{11}, z_{11})$  of the reflected rays on the aperture plane are

$$(10.6) \quad z_{11} = \frac{\frac{z}{n_3} (l_0 l_3 + m_0 m_3) - l_0 x - m_0 y}{l_0 l_3 / n_3 + m_0 m_3 / n_3 + n_0}$$

$$x_{11} = \frac{l_3}{n_3} (z_{11} - z) + x$$

$$y_{11} = \frac{m_3}{n_3} (z_{11} - z) + y$$

$$L_3 = (x_{11} - x)^2 + (y_{11} - y)^2 + (z_{11} - z)^2$$

$$L = L_1 + L_2 + L_3$$

$$\Delta L = L - L_0$$

where  $L_0$  is length of central ray which intersects the mid point of the paraboloidal surface. The aperture phase distribution is then

$$(10.7) \quad \delta(x_{11}, y_{11}, z_{11}) = \frac{2\pi \Delta L}{\lambda}$$

### 3.9.2.3 Aperture Diffraction Calculations

We now discuss the problem of calculating the far-field diffraction pattern of a circular aperture illuminated

with a specified amplitude and phase distribution. For all but a relatively few such distributions (e.g., uniform,  $(1 - 2)^n$ ) for which closed form solutions are available, the aperture radiation pattern must be evaluated numerically.

We start with the expression<sup>(11)</sup> for the radiation pattern of a circular aperture (see Fig. 3.23) of radius  $a$ ,

$$(11.1) \quad g(\theta, \phi) = \int_0^{2\pi} \int_0^a f(\rho, \phi') e^{jk\rho \sin\theta \cos(\phi - \phi')} \rho d\rho d\phi'$$

Letting

$$r = \rho/a$$

$$u = \frac{2\pi a \sin\theta}{\lambda}$$

we obtain

$$(11.2) \quad g(u, \phi) = a^2 \int_0^{2\pi} \int_0^1 f(r, \phi') e^{jur \cos(\phi - \phi')} r dr d\phi'$$

We express the aperture illumination in the form

$$(11.3) \quad f(r, \phi') = A(r, \phi') e^{j\psi(r, \phi')}$$

thus obtaining

$$(11.4) \quad g(u, \phi) = a^2 \left\{ \int_{-\pi}^{\pi} \int_0^1 A(r, \phi') \cos[\psi(r, \phi')] \cos[u \cos(\phi - \phi') r] r dr d\phi' \right. \\ \left. - \int_{-\pi}^{\pi} \int_0^1 A(r, \phi') \sin[\psi(r, \phi')] \sin[u \cos(\phi - \phi') r] r dr d\phi' \right. \\ \left. + j \left[ \int_{-\pi}^{\pi} \int_0^1 A(r, \phi') \cos[\psi(r, \phi')] \sin[u \cos(\phi - \phi') r] r dr d\phi' \right. \right. \\ \left. \left. + \int_{-\pi}^{\pi} \int_0^1 A(r, \phi') \sin[\psi(r, \phi')] \cos[u \cos(\phi - \phi') r] r dr d\phi' \right] \right\}$$

There are thus four double integrals to be evaluated of the form

$$(11.5) \quad \mathbf{I} = \int_{-\pi}^{\pi} \left[ \int_0^1 a(r, \phi') \begin{cases} \cos[V(\phi')r] \\ \sin[V(\phi')r] \end{cases} r dr \right] d\phi'$$

The procedure used for evaluating these integrals was to perform the inner integration, i.e., the integrating with respect to the radial variable  $r$ , by Filon's formula<sup>(29)</sup>, and to perform the outer integration, i.e., the integration with respect to the angular variable  $\phi$ , by the extended Simpson's

rule<sup>(30)</sup>. Both methods require evaluation of the integrals at an odd number of points. For the calculations performed here, it was found sufficient to use a grid of 25 points for the radial integrations and a grid of 151 points for the angular integration.

In Fig. 3.24 diffraction patterns calculated for the best azimuth focus are shown in the left side trace of Fig. 3.19A. For the cuts at  $\phi = 0^\circ$  and  $\phi = 180^\circ$  corresponding to azimuth plane patterns the pattern nulls and sidelobes are sharpest. The patterns in Fig. 3.25 are calculated for  $x_p, y_p, z_p$  as shown in the left trace of Fig. 3.19B. Now the elevation plane patterns corresponding to  $\phi = \pm 90^\circ$  cuts have the sharpest nulls and lowest sidelobes.

### 3.10 Effect of Near-Zone Diffraction of the 2.44 Meter Aperture

In this section we discuss the near field diffraction pattern of a paraboloidal reflector with a 2.44 meter diameter circular projection illuminated by a plane wave propagating in the direction parallel to the paraboloid axis. The calculations are described with reference to Fig. 3.26. The incident plane wave is assumed polarized with the magnetic field in the positive y direction and propagating in the positive z direction. (The positive X direction is taken to be pointing out of the plane of the paper.) The origin of the x,y,z coordinate system, 0, is the focus of the paraboloid.

The diffracted field is described with reference to spherical polar coordinates  $R, \theta, \phi$  based on the  $x, y', z'$  coordinate system centered at 0. The positive  $z'$  direction points in the direction of the ray from the center of the paraboloidal section passing through the focus. The  $y', z'$  axes can be obtained by rotating the  $y, z$  axes counterclockwise around the x axis by an angle  $\pi - \eta$  where

$$(12.1) \quad \eta = \tan^{-1} \left[ \frac{y_c}{\left( \frac{4F^2 - y_c^2}{4F} \right)} \right]$$

The procedure used for calculating the electromagnetic field components at a given point is as follows:

(1) let the coordinates of the given point,  $P_0$ , referred to spherical polar coordinates based on the  $x, y', z'$ -system be  $R_0, \theta_0, \phi_0$ ;

(2) obtain the coordinates of  $P_0$  referred to the  $xyz$ -system by the transformation

$$(12.2) \quad \begin{aligned} x_0 &= R_0 \sin \theta_0 \cos \phi_0 \\ y_0 &= -R_0 (\sin \theta_0 \sin \phi_0 \cos \eta + \cos \theta_0 \sin \eta) \\ z_0 &= -R_0 (\cos \theta_0 \cos \eta - \sin \theta_0 \sin \phi_0 \sin \eta) ; \end{aligned}$$

(3) calculate the x y z components of the diffracted electromagnetic field at  $x_0, y_0, z_0$  using the physical optics approximation to obtain the currents on the paraboloidal section and numerically integrating over the paraboloidal section;

(4) transform the field components in the x y z-coordinate system to components in spherical polar coordinates based on the x y' z'-system using the transformations

$$(12.3) \quad \begin{aligned} E_R &= E_x \sin \theta_0 \cos \phi_0 - E_y (\sin \theta_0 \sin \phi_0 \cos \eta + \cos \theta_0 \sin \eta) \\ &\quad - E_z (\cos \theta_0 \cos \eta - \sin \theta_0 \sin \phi_0 \sin \eta) \end{aligned}$$

$$(12.4) \quad \begin{aligned} E_\theta &= E_x \cos \theta_0 \cos \phi_0 - E_y (\cos \theta_0 \sin \phi_0 \cos \eta - \sin \theta_0 \sin \eta) \\ &\quad + E_z (\sin \theta_0 \cos \eta + \cos \theta_0 \sin \phi_0 \sin \eta) \end{aligned}$$

$$(12.5) \quad E_\phi = -E_x \sin \phi_0 - E_y \cos \phi_0 \cos \eta + E_z \cos \phi_0 \sin \eta$$

for the electric field components and similarly for the magnetic field components.

The physical optics approximation of the diffracted field is (Silver, Eq. 8, p. 132)

$$(12.6) \quad \vec{H}(P) = \frac{1}{4\pi} \int_S (\vec{K} \times \vec{V}) \frac{e^{-jkr}}{r} ds$$

with the surface current density  $\vec{K}$  given by

$$(12.7) \quad \vec{K} = 2 (\hat{n} \times \vec{H}_i)$$

where  $\vec{H}_i$  is the incident magnetic field. The electric field is obtained from the magnetic field by

$$(12.8) \quad \vec{E}(P) = \frac{1}{j\omega\epsilon_0} \nabla \times \vec{H}$$

Based on (10.1), (10.2), and (10.3), and with

$$(12.9) \quad \vec{H}_i = H_0(x, y) e^{-j k_z z} \hat{y}$$

(allowing the incident plane wave to have a tapered complex amplitude), the expressions for the field components in the  $x, y, z$ -coordinate system are as follows:

$$(12.10) H_x = \frac{1}{2\pi} \int_S dx dy H_0(x, y) \frac{x}{2F} (y_0 - y) a(x, y)$$

$$(12.11) H_y = -\frac{1}{2\pi} \int_S dx dy H_0(x, y) \left( z_0 - \frac{x^2}{4F} + \frac{y^2}{4F} + \frac{x_0 x}{2F} - F \right) a(x, y)$$

$$(12.12) H_z = \frac{1}{2\pi} \int_S dx dy H_0(x, y) (y_0 - y) a(x, y)$$

$$(12.13) E_x = \frac{1}{\pi j \omega \epsilon_0} \int_S dx dy H_0(x, y) a(x, y) - \frac{1}{2\pi j \omega \epsilon_0} \int_S dx dy H_0(x, y) b(x, y) \left[ (y_0 - y)^2 + \left( z_0 - F + \frac{x^2 + y^2}{4F} \right) c(x, y) \right]$$

$$(12.14) E_y = \frac{1}{2\pi j \omega \epsilon_0} \int_S dx dy H_0(x, y) b(x, y) (y_0 - y) \left[ (x_0 - x) - \frac{x}{2F} z_0 + \frac{x}{2F} \left( F - \frac{x^2 + y^2}{4F} \right) \right]$$

$$(12.15) E_z = -\frac{1}{\pi j \omega \epsilon_0} \int_S dx dy H_0(x, y) a(x, y) \frac{x}{2F} + \frac{1}{2\pi j \omega \epsilon_0} \int_S dx dy H_0(x, y) b(x, y) \left[ \frac{x}{2F} (y_0 - y)^2 + (x_0 - x) c(x, y) \right]$$

In the above equations for the field components

$$(12.16) \quad a(x, y) = \left( \frac{j k}{r^2} + \frac{1}{r^3} \right) \exp \left[ -j k \left( r + F - \frac{x^2 + y^2}{4F} \right) \right],$$

$$r = \left[ (x_0 - x)^2 + (y_0 - y)^2 + (z_0 - z)^2 \right]^{1/2},$$

$$b(x, y) = \left( \frac{3}{r^5} + \frac{3j k}{r^4} - \frac{k^2}{r^3} \right) \exp \left[ -j k \left( r + F - \frac{x^2 + y^2}{4F} \right) \right]$$

$$c(x, y) = z_0 - \frac{x^2}{4f} + \frac{y^2}{4f} + \frac{x_0 x}{2f} - f$$

The domain of integration, S, is

$$(12.17) \quad x^2 + (y - y_c)^2 \leq \left( \frac{D}{2} \right)^2$$

A computer program was written to calculate the components of the diffracted electromagnetic field based on the above expressions for the field components. The integrations were performed using the compound Simpson's rule. Two independent checks were made to verify the validity of the computer program. The first check was a comparison of the calculated field components with those obtained by Fante and Taylor<sup>(31)</sup> for the case of a symmetrical paraboloidal section; i.e.,  $y_c = 0$ . The second check<sup>(32)</sup> was a comparison with results obtained by Minnett and Thomas for the fields near the axis of a symmetrical paraboloidal reflector using an axial-wave representation of the scattered field. Excellent agreement was obtained in both checks.

Using the computer program, calculations were then performed to study the diffracted field of a 2.44 meter diameter paraboloidal section. The focal length,  $f$ , of the paraboloid was equal to 177.8 cms and the center of the paraboloidal section was located 157.48 cms above the  $z$ -axis ( $y_c = 157.48$  cms). The frequency was 12.2 GHz. An example of the results obtained is shown in Fig. 10.2A, B in which are plotted respectively the phase (in degrees) and magnitude of  $E_\theta/z_0$  ( $z_0 =$  ) in the plane  $\theta = 0$  for  $R = 43.18$  cms.

A taper of the incident magnetic field of the form

$$(12.18) \quad (\cos \psi_0)^{n/2} \cos^2 \psi_0$$

was used where  $\psi_0 = 2 \tan^{-1} \left\{ \frac{z}{\left[ x^2 + (y - y_c)^2 \right]^{1/2}} \right\}$

$$B = 1309.7164$$

and

$$n = 132.36$$

This taper gives an amplitude of -20 db at the edge of the paraboloidal section. The phase is seen to be quite flat until  $\theta$  begins to approach  $31^\circ$  corresponding to the ray through the focus from the upper edge of the paraboloidal section. Since the phase is plotted for constant R (i.e., on a spherical surface around the focal point) the small variation of the phase  $E\theta$  indicates that the diffracted field is closely approximated by a spherical wave.

#### 4.0 DESIGN AND FABRICATION

The Low Sidelobe SATCOM Antenna consists of a Feed Assembly, a Subreflector, and a Primary Reflector. The geometric relationship between the three main antenna components is shown in Figure 4-1. In the research model of the SATCOM Antenna, this geometric relationship is provided by arranging these principal components on a rigid platform so that the requisite exact positioning of these components is achieved. In this arrangement, the position of the feed assembly relative to the subreflector can be adjusted in a precise manner and within the bounds required for the research and development effort.

Adjustments during the configuration of the research model of the antenna is shown in Figure 4-2.

#### 4.1 Geometric Configuration

The three principal components comprising the SATCOM Antenna are located in a Cartesian coordinate system having its origin at the focal point of the primary reflector, with the Z axis coincident with the focal axis, and the Y axis oriented vertically, as shown in Figure 4-1.

The primary reflector is a section of a paraboloid having an aperture of 99" diameter. The reflector is offset from the Z axis (its focal axis) so that its center, labeled  $Y_c$ , is at  $y = 62.000$ . The subreflector is a concave surface of an especially computed contour (not definable as one of the conic sections) located to the right and below the focal point so that the center labeled "M" of its roughly 27" diameter aperture is located at  $Y = -12.922$ ",  $Z = -11.728$ ". Finally, the feed horn is located below and to the left of the origin with its axis inclined  $11.86^\circ$  from the Z axis, aimed at point M on the subreflector. The focal point F, of the feed horn is at  $Y = -3.137$ ",  $Z = 34.859$ ".

Provision is made in supporting the feed horn for changing its position in the coordinate system so that it can be accurately scanned in the Y-Z plane and concurrently in the X-Z plane through an angle of  $\pm 13^\circ$ , with its axis always aimed at point M on the subreflector.

## 4.2 Mechanical Design

The mechanical design of the complete antenna system including the primary reflector, subreflector, feed horn, feed horn support, and of the platform were completed in sufficient detail to permit their fabrication. This design is discussed below. The actual fabrication of the feed horn and of the subreflector was accomplished by Chu Associates, Inc. as part of Contract NAS 3-22343.

### 4.2.1 Primary Reflector

The primary reflector is constructed of fiberglass-epoxy laminate shown in Figure 4-3, Drawing B-10753. This type of construction was selected because of the relative simplicity in the tooling required to make a single unit, because of the ease with which glass cloth can be cut and formed into complex shapes, because of its low shrinkage, and because of its low density. The reflecting surface is rendered conductive by flame spraying aluminum onto the concave surface after lay-up. Other details of construction are as shown on the drawing. The reflector is mounted onto the platform by means of four 1/2" diameter bolts passing through the flat mounting interface provided on the rear of the reflector, parallel with the focal axis. The entire weight of the reflector is estimated to be 220 lbs.

### 4.2.2 Subreflector

The subreflector consists of a reflecting panel made of fiberglass epoxy laminate, reinforced by a rear, box-like attachment made of aluminum sheet, as shown in Figure 4-4. The purpose of the sheet metal reinforcement is to impart torsional rigidity and to provide the means of attachment to the platform. This means of attachment consists of two holes in each of two aluminum angle legs affixed to the sheet metal reinforcement. Threaded studs passing through these holes, together with hexagonal nuts on the studs, not only secure the subreflector to the platform but also allow dimensional adjustments between the subreflector and the platform. Reference marks and physical reference points, of known position relative to the point M have been included in the reinforcing structure enabling the exact positioning of the subreflector in the coordinate reference system.

#### 4.2.3 Feed Horn

The feed horn external configuration is shown in Figure 4-5. Detail of design and physical parameters are discussed in Section 5.0 of Phase I.

In order to acquire experimental data, the Feed Horn is required to be scanned  $+ 13^\circ$  in the horizontal plane. This is accomplished by means of the device shown in Figure 4-6, Drawing A-10754. It consists of a cradle, A-10762, to which the feed horn is affixed. The cradle is attached to a guide plate, A-10761, by means of screws passing through slotted holes and a straight key. This permits the linear adjustment of the feed horn along its own axis through a distance of  $+ 2$ " from nominal setting. The guide plate is attached to two vertical support arms (left hand and right hand), A-10758, using the intermediary follower bracket, A-10760 (also left hand and right hand). This provides the angular adjustment of the feed horn through a range of  $+ 13^\circ$  from nominal position, in a vertical plane. In every angular position, the axis of the feed horn passes through point M on the subreflector. Side braces, A-10759, are strictly structural items for the purpose of bracing the vertical support arms in the lateral direction. Next, the vertical support arms and side braces are attached to a swivel base A-10756, which, in turn, is mounted on platform B-10752. The swivel base is mounted on the platform by means of a pivot pin and four clamps so that releasing the clamps allows the pivot base to swing, or "pivot", about the pin, carrying with it the feed horn and associated support hardware. In this manner, angular positioning of the feed horn in the horizontal plane is provided through a range of  $+ 13^\circ$  from nominal setting. Here too, the axis of the feed horn, in every position, passes through point M on the subreflector.

#### 4.2.4 Platform

The platform is a trussed frame structure having provisions on one face for supporting the reflector, the subreflector, and the feed horn in proper geometrical relationship, having provisions on its opposite face for mounting onto a pattern range positioner, and having sufficient rigidity to maintain the requisite geometrical relationships in any position relative to gravity. The design for the platform is shown in Figure 4-7. This is an all aluminum weldment not requiring any machining after welding except for the location and drilling of holes. The weight of the entire structure is estimated to be 200 lbs.

#### 4.3 Tooling and Fabrication

Fabrication of the primary reflector and of the subreflector, each having a precision, concave reflecting surface, requires special tooling in the form of a mold for each reflector on which the fiberglass laminated layups can be made.

#### 4.3.1 Primary Reflector

A mold for fabrication of the primary reflector was in the process of construction when, in consideration of budgetary allocations, further work was abandoned. Accordingly, in order to fabricate a reflector, this work would have to be picked up where it was left off and carried to completion.

The mold for the primary reflector consists of a completely enclosed box, inclined relative to the floor, the top surface of which is the desired paraboloidal contour, as shown in Figure 4-8, Drawing 810309. The sides, the bottom, and the internal partitions are made of plywood. The top surface is a fiberglass epoxy laminate. A vertically standing "kingpost", located 6" off the side of the mold defines the focal axis of the paraboloidal surface. A sweep arm, Figure 4-9, Drawing 810408, is positioned over the mold, one end of which is support by the kingpost, and the other end of which rests on a precisely leveled circular track, shown in Figure 4-10. The center of this track is roughly coincident with the center line of the kingpost. Supported in this manner, the sweep arm can be manually moved, or "swept" over the top surface of the mold with the vertical, kingpost axis the axis of rotation. A template, one edge of which is the exact parabolic contour required, is attached to the swing arm. It is essential that reference holes and/or surfaces be incorporated in the template enabling precise positioning of the template relative to the kingpost axis, thus placing the focal axis of the parabolic template exactly on the axis of rotation. The rough mold surface, as thus far developed, is probably within 0.10" of the required contour. The object now is to coat the mold surface with resin and to scrape away or "screed" the excess resin by sweeping the template over the mold surface leaving behind a radial contour which is the contour of the template, and thus a surface contour which is a paraboloid. The swing arm, the kingpost, and the track are now removed as they serve no further use in fabrication of the end item, the reflector panel.

The status of completion for the reflector mold is the basic mold as depicted in Figure 4-8, having a rough fiberglass top surface ready for screeding, a swing arm as depicted in Figure 4-9, and a kingpost as depicted in Figure 4-11. A circular track remains to be completed as well as a parabolic template.

#### 4.3.2 Subreflector

The mold used in fabricating the subreflector is shown in Figure 4-12. It consists of 59 templates spaced at 1/2" intervals, the contour of each template having been cut on a CNC milling machine to match the contour of the subreflector through the particular cut represented by that template. The templates are then set on a surface plate, squared-up, and drawn together, the space between them being filled with a foam material. Afterwards, the filler material is skived to blend smoothly with the sharp edges of the templates. All through these procedures, the tolerances held in positioning and aligning was + .005" as a goal with + 0.010" maximum acceptable. Filling the space between templates with foam material imparts sufficient rigidity to the mold for it to be considered a rigid body, enabling it to be moved about without distortion (more precisely, negligible distortion).

#### 4.3.3 Feed Horn

The corrugated feed horn was manufactured to print without the use of any special tool or fixture. Accordingly, no tooling exists for this item.

#### 4.3.4 Assembly and Alignment

The primary reflector, the subreflector, and the feed horn are assembled onto the platform as shown in Figure 4-2. The position of these three components relative to each other is defined by their location in a three axis Cartesian coordinate system as depicted in Figure 4-1. Successful performance requires that the positioning of these components be precise, within .020" of true location. Accordingly, features have been included in the reflectors and in the platform to facilitate positioning these components by optical means.

#### 4.4 ANTENNA ASSEMBLY PROCEDURES

##### 4.4.1 Platform

Because of the impracticality of machining reference surfaces on the platform, reference points are provided by the use of 1/2-20 UNC-2A threaded studs labeled "B" and "C" in Figure 4-7. Adjusting the height by which these protrude from the surfaces on which they are mounted is equivalent to removing (or adding) metal by machining. The platform should be set on the shop floor in a nominally level position, securely propped so that the weight of additional components, as they are installed, does not disturb the position of the platform relative to the floor. Next, an engineers transit or a theodolite is set up and leveled so that two orthogonal, horizontal lines of sight are nominally aligned with the short and long sides of the platform. The three studs on the top surface labeled "B" are now adjusted in height until all three are the same distance + .005" from the transit's level line of sight (L.O.S.) and locked in place using the hexagonal lock nuts. These three buttons now define a plane parallel with the X-Y plane of the coordinate system. Next, the two studs labeled "C" are adjusted so that they are the same distance + .005" from the transit's L.O.S. which is aligned with the long side of the platform. These two buttons define a line which is parallel with the Y-Z plane of the coordinate system. Finally, the transit is traversed 90° in order to position stud labeled "D". The vertical, Y axis of the coordinate system falls 11.728" to the left of pivot pin labeled "E". Accordingly, if the face of the "D" stud is set to be 6.272" + .005 from the center of pin "E", this stud will be 18.000" from the Y axis, a "round" number for convenience in arithmetic later on. Going back to studs labeled "C", convenience in arithmetic would be obtained if in addition to being parallel to the Y-Z plane, they are also set to be 19.000" from the center of the pivot pin. We have thus far established the X, Y, and Z directions of the coordinate system and the X and Z location of the origin. We have yet to establish the Y location of the origin.

#### 4.4.2 Feed Support Device

Place the pivot plate, Figure 4-6b in place on the platform so that it is positioned by the pivot pin, and install the four clamps. Now place shims under the pivot plate under each of the four clamp areas and trim the thickness of each shim as required to make the pivot plate level, i.e. parallel with the X-Z plane, using the transit. Tack weld, pin, or otherwise secure the shims to keep them in place. Install the vertical support arms, shown in Figure 4-6a onto the pivot plate and affix the horn positioning fixture, shown in Figure 4-13, to one of the vertical support arms. For convenience, level the fixture using the lines inscribed on it for that purpose. A non-level condition will not affect the position of point "M" in Figures 4-6a, and 4-13. Using the transit, adjust the position of the vertical support arm so that the location of point M on the fixture is 6.272" in the Z direction from reference button D on the platform. Measure and record the position of point M on the fixture from reference buttons "B" on the platform, in the Y direction. Repeat this procedure with the fixture affixed to the other vertical support arm. We have now fixed the position of point M on the subreflector surface. Since this point is 12.922" below X-Z plane we know the vertical, Y distance from the origin to the "B" buttons on the platform.

#### 4.4.3 Reflector

Mount the primary reflector, Figure 4-3 onto the platform using four 1/2" 20UNF2A studs as stand-offs. A pair of hexagonal nuts secure each stud onto the flange of the reflector and likewise, a pair of hexagonal nuts secure these same studs onto the flange of platform. The nominal space between the reflector mounting flange and the platform is 1.4". Adjust the lengths of the inboard pair of studs relative to the outboard pair of studs until the scribed lines labeled "B" on the reflector lie in a level plane, i.e., parallel with the Z direction. Likewise, adjust the lengths of the pair of studs on the left side relative to the pair of studs on the right side until the scribe lines labeled "C" on the reflector lie in a level plane parallel with the X direction. Having accomplished this, the lengths of all four studs are adjusted in unison to set the height of the reflector above the X-Y plane. Height measurements are to be made from the "B" buttons on the platform to the target placed in the face of the reflector at the center of the aperture. This target is at Y = 62.000". Finally, the four nuts on the inside of the platform can be loosened and the reflector repositioned in the X direction and/or the Z

direction until the center target on the reflector is at  $X = 0$  and at  $Z = 56.271$ ". There are four other targets built into the reflector surface near its rim. Two of these are aligned with the horizontal, X direction and two are aligned with the vertical, Y direction. These are to be used to verify alignments in these directions.

#### 4.4.4 Subreflector

The subreflector is mounted onto the platform in the same way as the primary reflector, via four mounting studs. It straddles the pivot pin at the right hand end of the platform. Positioning the subreflector into its correct location in the coordinate system is accomplished by manipulating the studs in the same manner as used in positioning the primary reflector. Reference buttons have been incorporated into the subreflector for the purpose of leveling, or aligning with the X, Y, and Z directions. In addition, scribe lines have been placed on the structure at known distances from point M on the subreflector surface. These lines are used for distance measurements.

Referring to Figure 4-4, the three buttons marked "B" define a plane parallel with the X-Z plane. The two buttons marked "C" define a line parallel with the X-Y plane. The button marked "D" is 11.500" from the Y-Z plane. In other words,  $X = 11.500$ ". The scribe lines just under the two B buttons in the right hand view, parallel with the base, are placed 8.000" below point M. Therefore, these two lines are at  $Y = 8.000 + 12.992 = 20.922$ "(-). Another scribe line, aligned vertically, also under (one of) the B buttons is placed 5.000 from point M on the subreflector surface. Therefore, this line is at  $Z = 11.728 - 5.000 = 6.728$ "(-).

A completed subreflector as shown in Figure 4-4 (Dwg. A-10763) has been manufactured and is furnished as a deliverable item under contract NAS 3-22343.

#### 4.4.5 Feed Horn

No special features have been provided on the feed horn for mounting. However, the existing feed horn must be modified by drilling and tapping several holes into one of its steps to facilitate holding it in the feed support device, Figure 4-6. These are six #10-32UNF2B holes equally spaced on a 9.125" dia. B.C., as shown in Figure 4-5.

## 5.0 RESULTS AND CONCLUSIONS

The results reported in Analysis Sections 3.1 and 3.2, on the best offset dual reflector antenna configuration show that for the 2.44 meter diameter aperture scanned over a  $3^\circ$  cone by horn motion, the paraboloid focus to aperture diameter ratio ( $f/D$ ) and subreflector eccentricity should be selected to provide a dual reflector magnification factor of about 3.25. This choice leads to a paraboloid focal length of 177.8 cms, a conical horn with semiflare angle of  $12^\circ$ , and a subreflector diameter of about 76 cms. A Gregorian (near ellipsoidal) rather than a Cassegrain (hyperboloidal) subreflector shape was selected because it produces higher aperture edge tapers when fed by a corrugated conical horn and, hence, lower pattern sidelobes. The horn near-zone pattern is also more uniformly distributed over the ellipsoidal subreflector and the horn mouth can be brought nearer to the subreflector.

A significant result in Section 3.3 is that the several different theories for calculating ideal sidelobe level vs. aperture efficiency relations all lead to about the same radial distribution curves over the aperture with edge tapers ranging from 15 db to 20 db when -30 db to -40 db sidelobe levels are required with 70% to 80% efficiencies. Of considerable practical consequence is the finding that actual corrugated conical horn near-zone patterns, when reflected by the optimally tilted subreflector, produce nearly ideal radial aperture distributions for the sidelobe levels desired.

In Section 3.4 the largest analytical task was to extend Clarricoats work on corrugated conical horns to the longer horns needed to produce lower edge tapers on the subreflector. The important design result is the dependence relation of horn length on subreflector edge illumination. For the model antenna configuration a  $12^\circ$  horn, 76cms long, should produce tapers needed for -35 db first sidelobe levels and 40 db for all others and a 63 cm horn is appropriate for -30 db first sidelobes with higher aperture efficiencies. In the range of horn length studies, horn phase errors in the near zone patterns were computed. These horn phase errors lend to produce a rise in sidelobe levels of approximately 2 to 3 db.

In Section 3.5 the iterative calculations for dimensioning long corrugated conical horns are given, and in Section 3.6 diffraction pattern calculations are described which take numerical data from the phase and amplitude horn patterns to generate the antenna patterns of the 2.44 meter dish. This analytical procedure is thought to be new.

The principal result of the research reported in Sections 3.7 and 3.8 is that because the antenna aperture distribution is nearly optimum when fed by the 76 cms long  $12^\circ$  conical horn, only the aperture phase errors due to the horn phase pattern need to be corrected. These horn phase errors can be corrected somewhat by slightly refocusing the horn or by increasing the eccentricity of the subreflector. However, these adjustments are inadequate when stringent sidelobe requirements are to be met. A method for shaping the subreflector surface to eliminate, in an optical sense, the horn phase errors is therefore presented. Shaping the subreflector even a minor amount as required here leads to surfaces which cannot be constructed by revolving or sweeping in a lathe. The subreflector contours were described by a set of templates. A judgement must be made on economic grounds concerning the rather small increase (2 - 3 db) in sidelobe levels on an antenna with an ellipsoidal or revolved subreflector compared to the more expensive shaped subreflector construction.

The work of section 3.9 is significant in that it provides a method for finding the focal surfaces on dual reflector antennas. This means that when beam steering by horn positioning is required, the loci for locating the horn or feed phase center and the angular orientation of the horn can be calculated.

Finally, in Section 3.10, the difficult problems of near-zone effects produced by the 2.44 meter aperture in the region of the subreflector are formulated and fields computed. The fields from the aperture should match those of the conical horn in the region of the subreflector over the 12 GHz and 14 GHz bands. Results indicate that the frequency dependence of antenna pattern sidelobe levels appear to be small. The numerical analysis involving tapered aperture fields is a useful theoretical achievement.

The complete antenna system, including parabolic reflector, shaped subreflector, primary feed horn, and mounting frame has been mechanically and structurally designed as part of the contract. The corrugated feed horn was built and tested, and its' phase and amplitude characteristic obtained for use in design of the balance of the antenna. The specially shaped, high precision, subreflector was also built and furnished as part of contract NAS 3-22343. The remainder of the antenna system was not manufactured as part of this contract.

In order to verify the theoretical design contained in this report, it is necessary to complete manufacture of the balance of the antenna system and to conduct comprehensive performance tests.

6.0 REFERENCES

- (1) H. Tanka and M. Mizusowa, "Elimination of Cross Polarization in Offset Dual Reflector Antennas," Trans IECE, Vol. 58-B, No. 12, UOC, 1975.
- (2) Y. Mizugutch, et al, "Offset Dual Reflector Antennas," IEEE, AP-S Symp. Dig. (Univ. of Mass., Amherst, MA.), pp 2-5, Oct. 1976.
- (3) N.A. Adatia and K. M. Kien, "Radiation Characteristics of a Double Offset Antenna: Theory and Experiment," IEEE, AP-S Symp. Dig. (Quebec, Canada), p 545, June 1980.
- (4) C. J. Sletten, "Subreflector and Main Reflector Shaping for Beam Tracking Offset Antennas," IEEE, AP-S Symp. Dig. (Seattle, WA) pp 88-91, 1 June 1979.
- (5) C. J. Sletten, "Numerical Technique for Shaping Reflecting Surfaces to Synthesize Antenna Patterns," Proc. IEEE, Vol. 69, pp 392-394, March 1981.
- (6) Reflector Antenna Analysis and Design, P. J. Wood, Peregrinus Ltd. 1980, Chapter 5.
- (7) P. W. Hannan, "Microwave Antennas Derived from the Cassegrain Telescope," IRE, T-AP 9, pp 140-153, March 1961.
- (8) J. W. Sherman, "Aperture Antenna ANalysis," Radar Handbook, M. Skolnik, McGraw Hill, 1970, Chapter 9.
- (9) V. Kouznetsov, "Sidelobe Reduction in Circular Aperture Antennas," 1978 European Antenna Conference Digest, London.
- (10) P. Jacquinet and B. Roizin-Dossier, Progress in Optics, Emil Wolf, Vol. III, 1964, North Holland.
- (11) Microwave Antenna Theory and Design, S. Silver, ed., p 192 ff, McGraw Hill, 1949.

- (12) (a) Clarricoats, P.J.B. and Saha, P.K.,  
"Radiation From Wide-flare-angle Scalar  
Horns," Electron. Lett. 5 (1969), pp  
376-378.
- (b) Clarricoats, P.J.B. and Olver, A.D.,  
"Near-field Radiation Characteristics of  
Corrugated Horns," Electron. Lett. 7 (1971),  
pp 446-448.
- (c) Clarricoats, P.J.B. and Saha, P.K.,  
"Propagation and Radiation Behavior of  
Corrugated Feeds. Part 2 -  
Corrugated-Conical-Horn Feed," Proc. IEE 11P  
(1971), pp 1177-1186.

These papers are reprinted in Love, A.W. (ed.),  
Electromagnetic Horn Antennas, IEEE Press, N.Y.,  
1976.

- (13) Stegun, Irene A., "Legendre Functions," Chapter 8  
in Abramowitz, M. and Stegun, I.A., Handbook of  
Mathematical Functions and Formulas, Graphs, and  
Mathematical Tables, National Bureau of  
Standards, U.S. Government Printing Office,  
Washington, D.C., 1964. See Eq. 8.5.4.
- (14) Stegun, I.A., referenced above in (13): Eq.  
8.5.3.
- (15) See Fig. 2 and Table 1 of Clarricoats, P.J.B. and  
Saha, P.K., referenced above in (12c)
- (16) Lebedev, W.N. and Silverman, R.A. (trans.),  
Special Functions and Their Applications, Dover  
Publications, N.Y., 1972. See note 29 n p 193.  
Definition (11a) is used by Lebedev and by Stegun  
referenced above in (13).
- (17) Lebedev, W.N., referenced above in (16). See Eq.  
7.3.6.
- (18) These tables may be obtained on application to  
P.J.B. Clarricoats. For address see the papers  
referenced above in (12).
- (19) Forsythe, George E., Malcom, Michael A., and  
Moler, Clara B., Computer Methods for  
Mathematical Computations, Prentice-Hall, N.J.,  
1977. See Chapter 7.
- (20) Forsythe, G.E. et al, referenced above in (19).  
See Chapter 5.

- (21) IBM System/360 Scientific Subroutine Package, Version III.
- (22) Stegun, I.A., referenced above in (13). Eq. 8.2.1.
- (23) Antosiewicz, H.A., "Bessel Functions of Fractional Order," Chapter 10 in Abramowitz, M. and Stegun, I.A., referenced above in (13). See Section 10.5
- (24) Antosiewicz, H.A., referenced above in (23). Eq. 10.1.19.
- (25) Antosiewicz, H.A., referenced above in (23). Eq. 10.1.15.
- (26) Olver, F.W.J., "Bessel Functions of Integer Order," Chapter 9 in Abramowitz, M. and Stegun, I.A., referenced above in (13). See Eq. 9.2.4.
- (27) Olver, F.W.J., referenced above in (26).
- (28) Antenna Theory, Part II, Collin and Zucker, McGraw Hill, 1969, p 55 ff.
- (29) P. J. Davis and P. Rabinovitz, Method of Numerical Integration, Academic Press, 1975. pp 122-124, 369-370.
- (30) P. J. Davis and P. Rabinovitz, op cit, p. 46.
- (31) R. L. Fante and R. L. Taylor, "The Complete Electromagnetic Fields in the Focal Region of a Paraboloidal Reflector," RADC In-House Report, RADC-TR-76-295. Sept. 1976.
- (32) H. C. Minnett and B. Mac A. Thomas, "Fields in the Image Space of Symmetrical Focusing Reflectors," Proc. IEE, 115, 1419-1430, 1968.

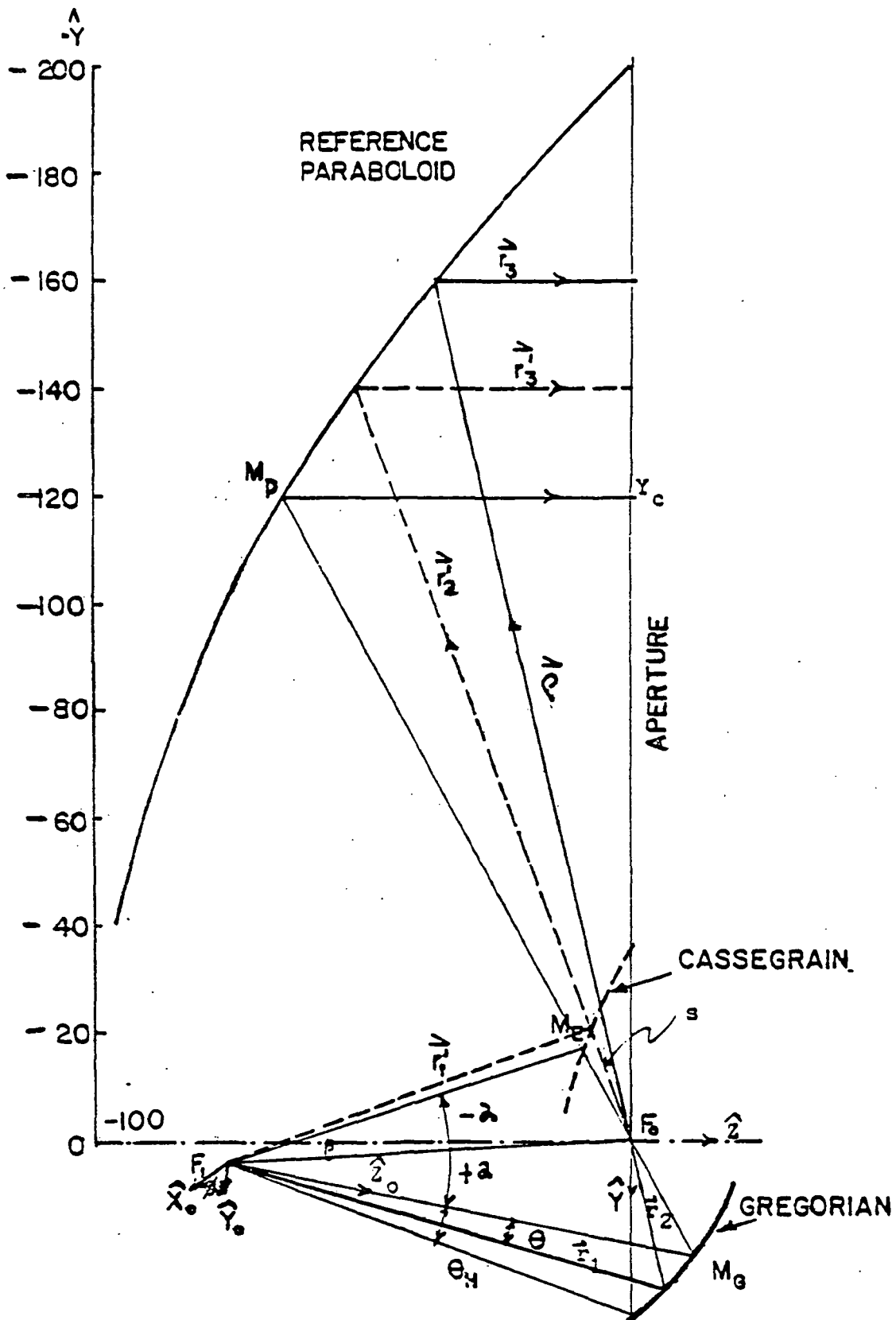


FIG.3.1 OFFSET DUAL REFLECTOR GEOMETRY FOR REFERENCE SURFACES

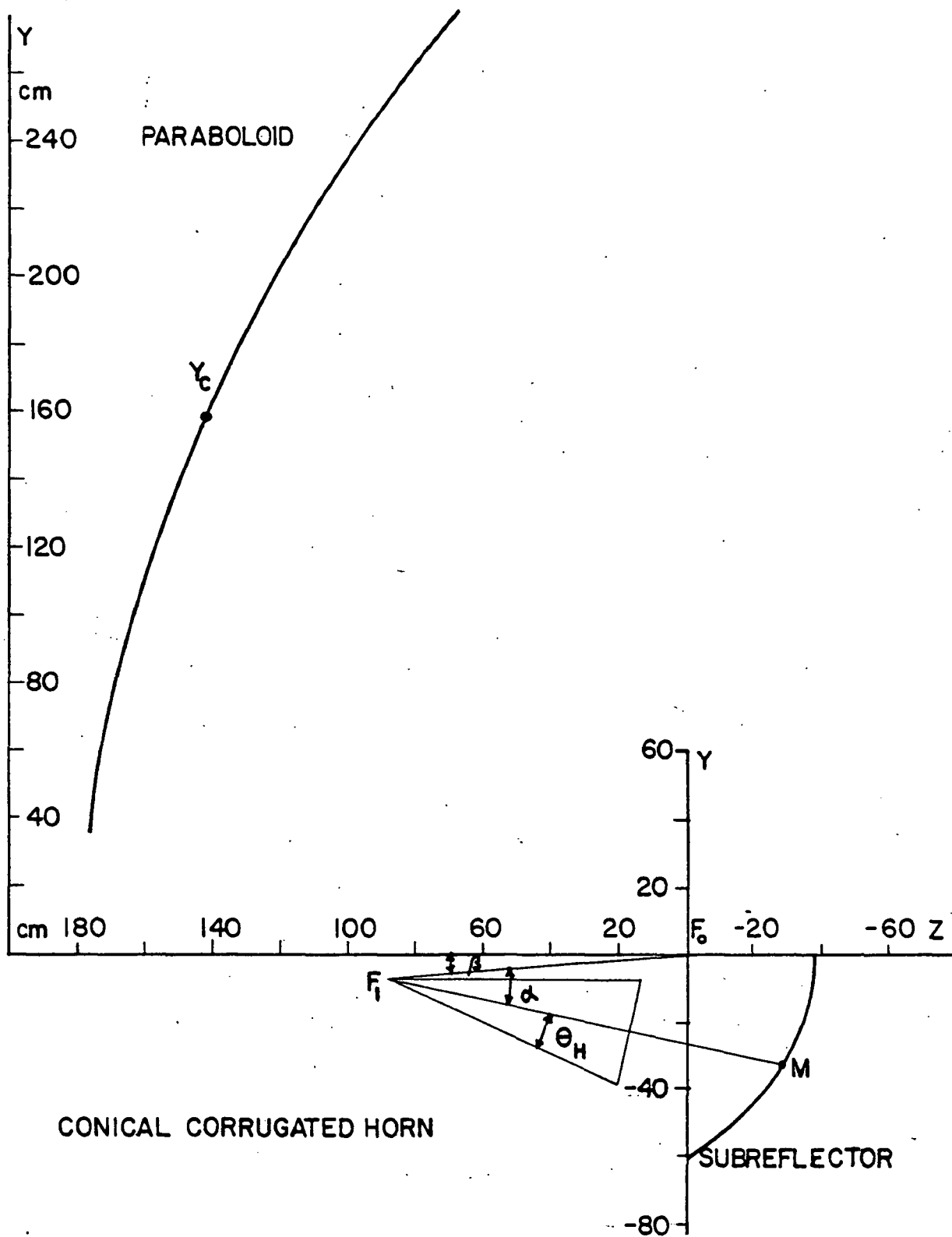


FIG. 3.2 CROSS SECTIONAL VIEW OF MODEL ANTENNA

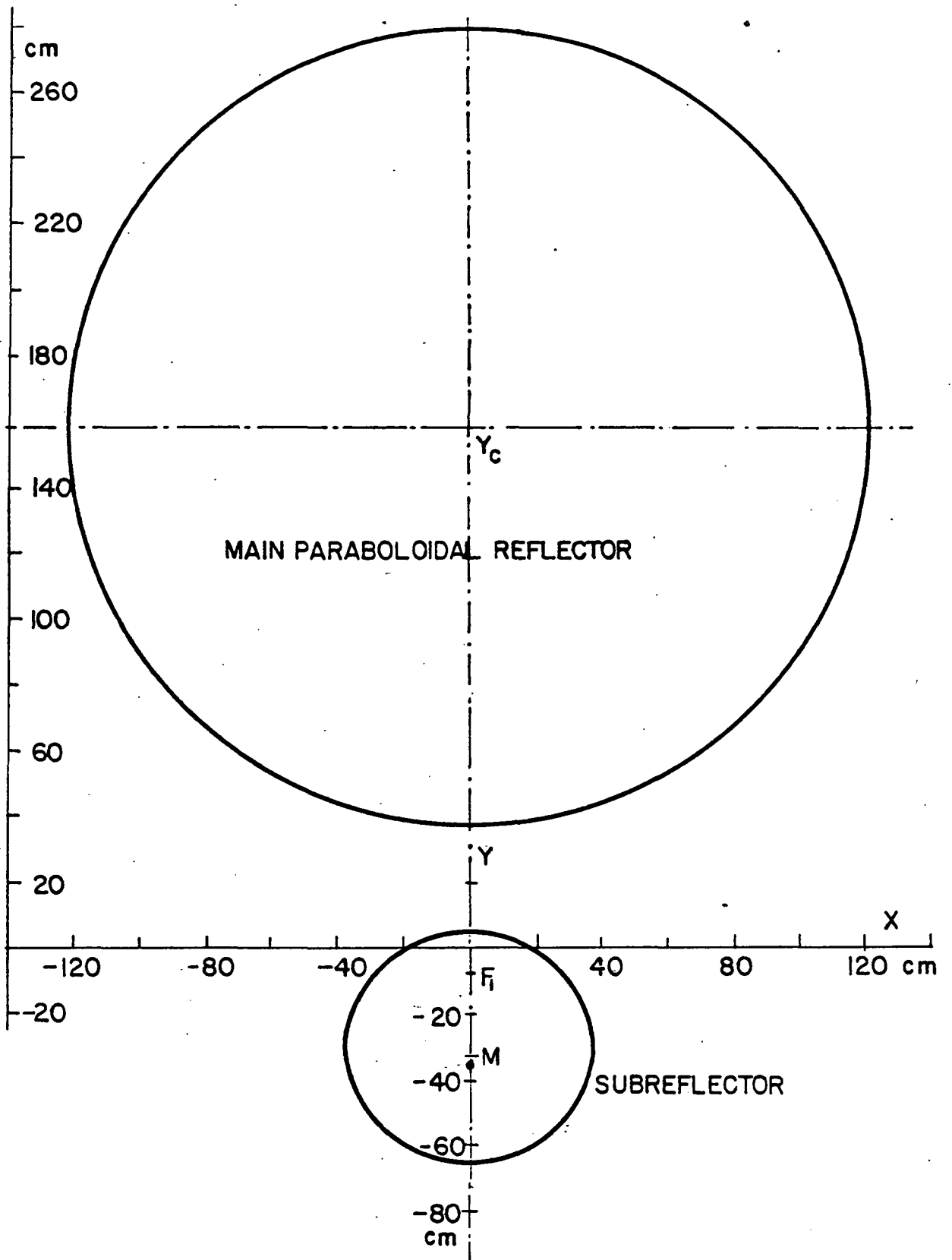
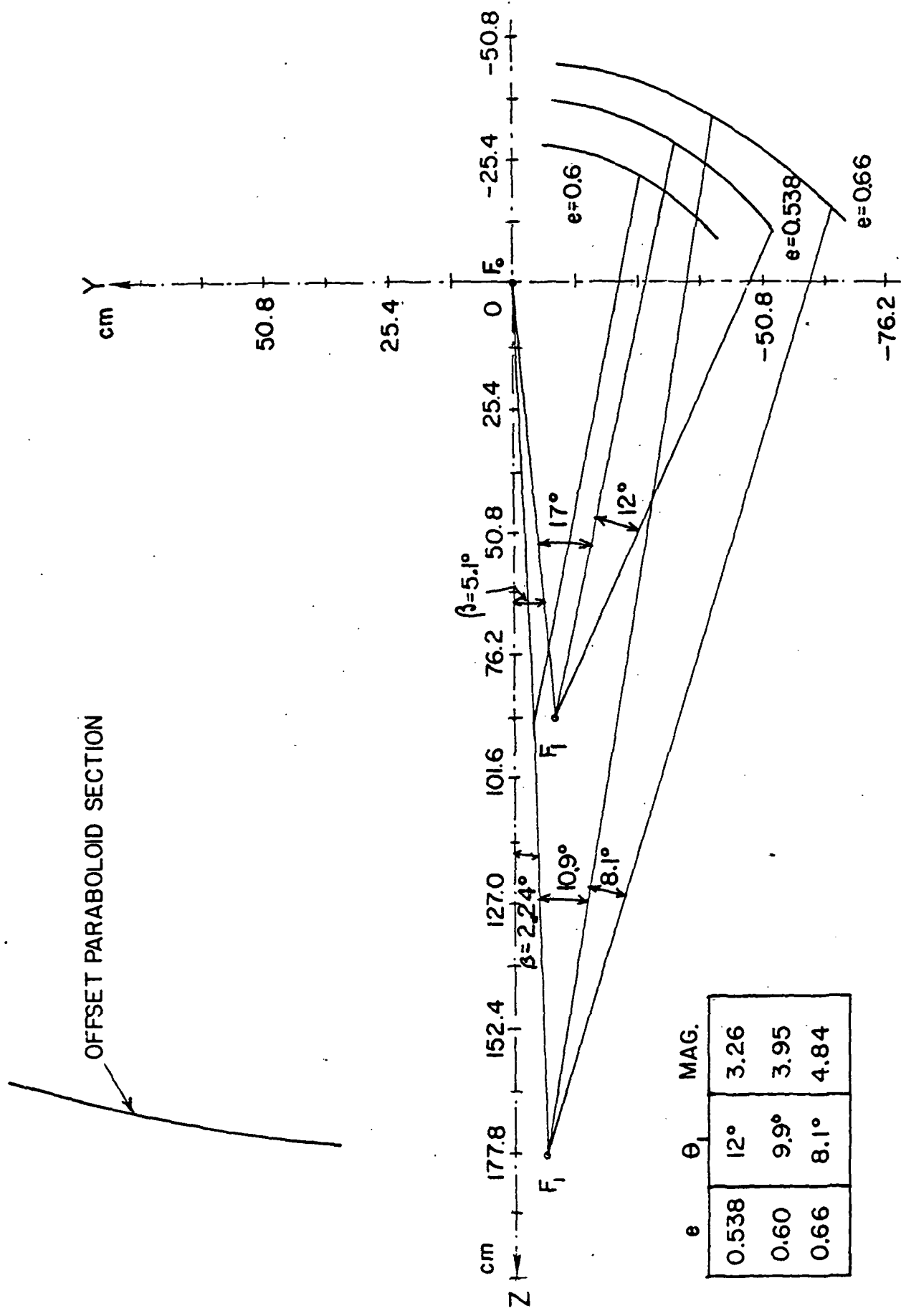


FIG. 3.3, FRONT VIEW OF MODEL ANTENNA



| e     | $\theta_1$  | MAG. |
|-------|-------------|------|
| 0.538 | $12^\circ$  | 3.26 |
| 0.60  | $9.9^\circ$ | 3.95 |
| 0.666 | $8.1^\circ$ | 4.84 |

FIG. 3.4 DESIGN PARAMETER TRADEOFFS

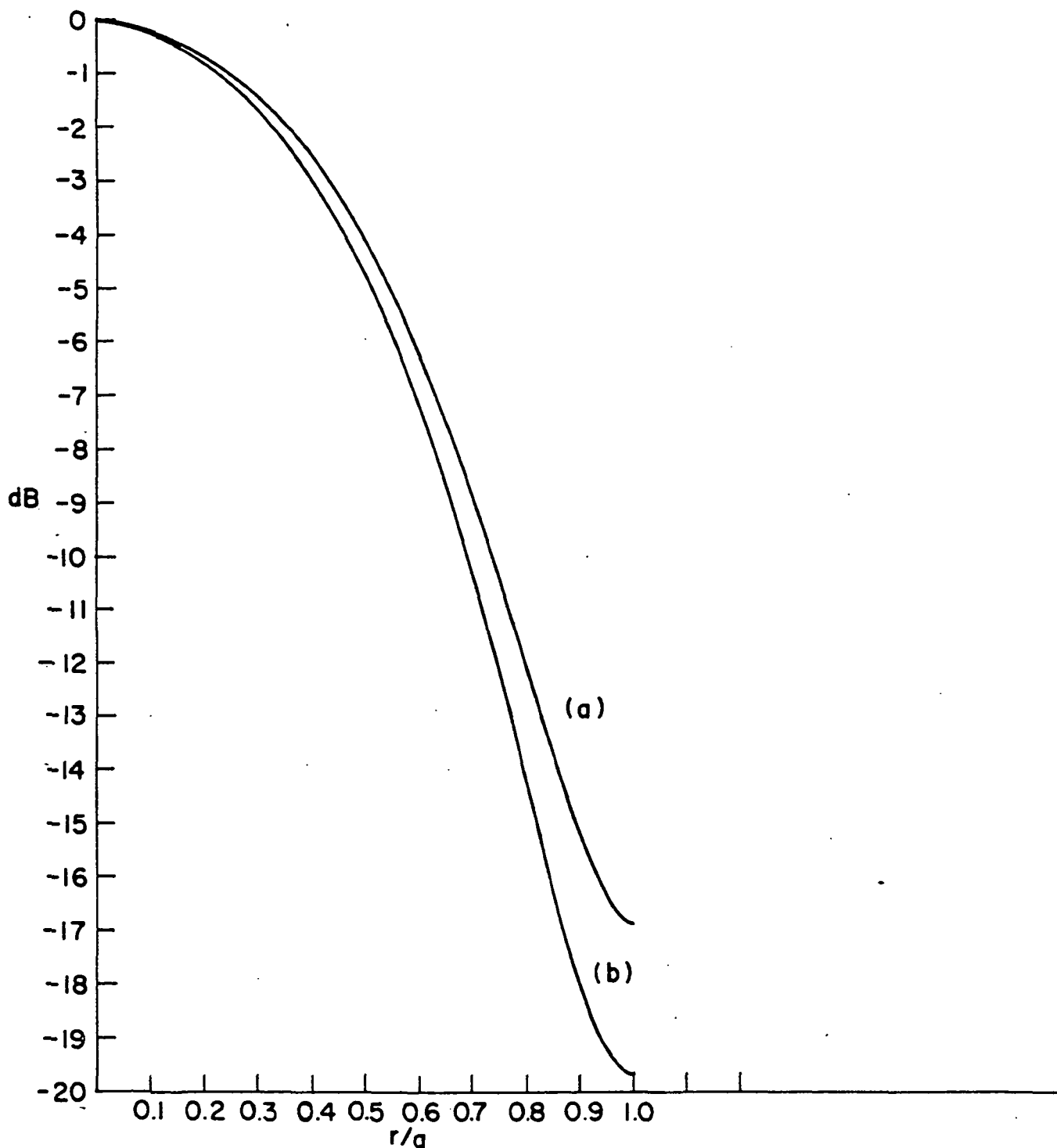


FIGURE 3.5 KOUZNETSOV LOW SIDELobe CIRCULAR APERTURE ILLUMINATION FUNCTIONS

$$a) G(r) = \frac{1}{7} + \frac{6}{7} (1-r^2)^2$$

$$b) G(r) = \frac{3}{29} + \frac{18}{29} (1-r^2)^2 + \frac{8}{29} (1-r^2)^3$$

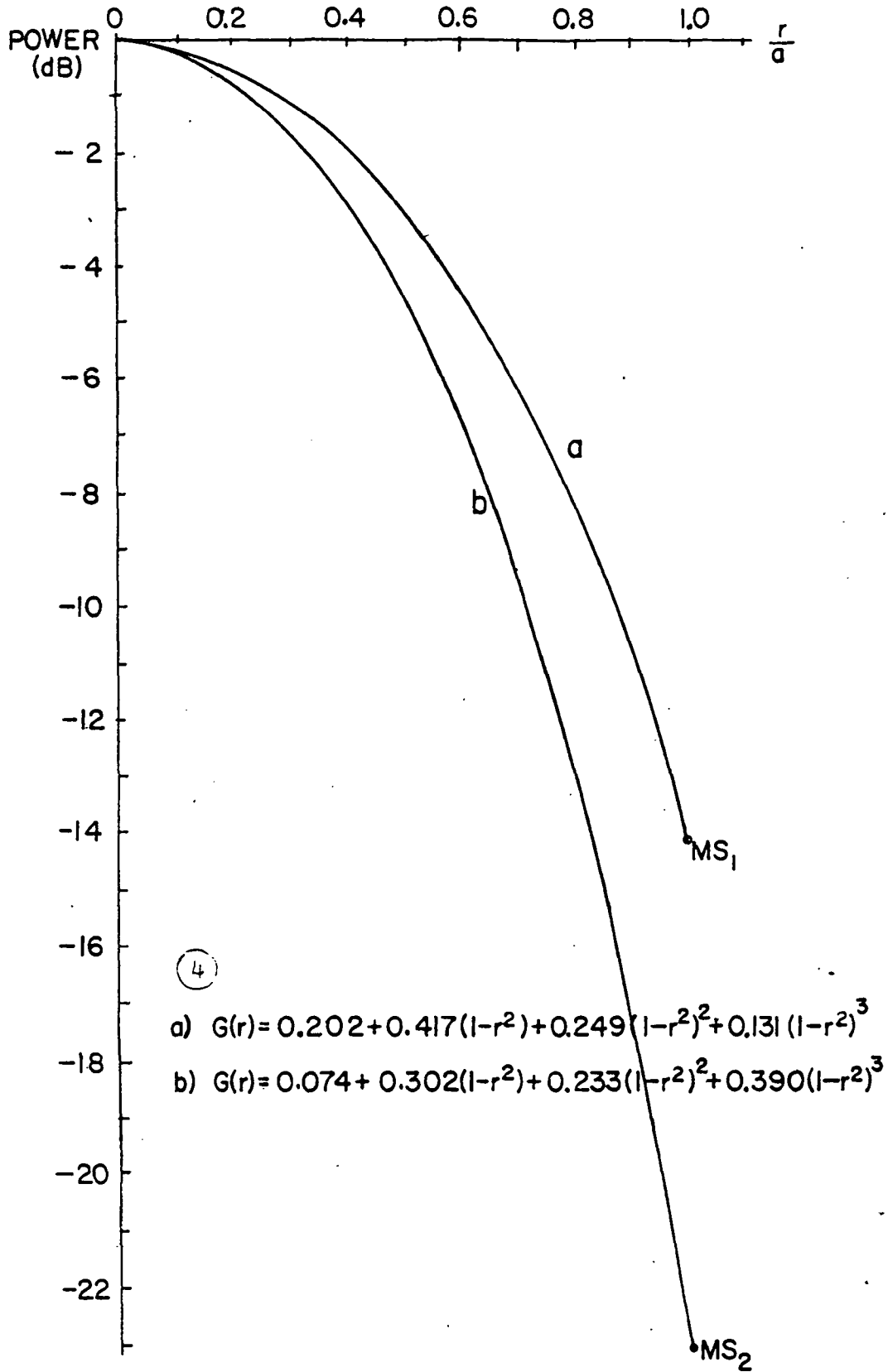


FIG. 3.6 MINIMUM SPREADING FACTOR FUNCTIONS

KEY TO  
ILLUMINATION FUNCTIONS OF TABLE 3.1

- 1 UNIFORM
- 2 76.2 cms, 12° CORRUGATED HORN  
 A NO PHASE ERROR  
 B PHASE ERROR INCLUDED
- 3 KOUZNETSOV LOW SIDELobe FUNCTIONS  
 A  $G(r) = 1/7 + 6/7 (1-r^2)^2$   
 B  $G(r) = 3/29 + 18/29 (1-r^2)^2 + 8/29 (1-r^2)^3$
- 4 MINIMUM SPREADING FACTOR FUNCTIONS  
 A  $G(r) = 0.202 + 0.417 (1-r^2) + 0.249 (1-r^2)^2 + 0.131(1-r^2)^3$   
 B  $G(r) = 0.074 + 0.302 (1-r^2) + 0.233 (1-r^2)^2 + 0.390(1-r^2)^3$
- 5  $G(r) = b + (1-r^2)^3$   
 A  $b = 0.5$   
 B  $b = 0.4$   
 C  $b = 0.32$
- 6  $G(r) = \cos^{n/2} \theta_0 \cos^2 \theta_0/2$   
a = 48  
B = 515.64  
 A  $n = 198.29$  (-15 dB taper)  
 B  $n = 264.72$  (-20 dB taper)
- 7  $G(r) = 1, 0 \leq r \leq r_1$   
 $G(r) = 1 + \frac{1-b}{2} \left[ \frac{\cos \pi(r-r_1)}{1-r_1} - 1 \right], r_1 \leq r \leq 1$   
 A  $r_1 = 0.15, b = 0.23$   
 B  $r_1 = 0.10, b = 0.23$   
 C  $r_1 = 0.05, b = 0.23$

TABLE 3.1

APERTURE EFFICIENCY, HALF-POWER POINT, AND SIDELOBES  
FOR DIFFERENT CIRCULAR APERTURE ILLUMINATION FUNCTIONS

| Case | Apt<br>Eff | BW<br>1/2<br>Pwr | $u_1$ | $S_1$  | $u_2$ | $S_2$  | $u_3$ | $S_3$  | $u_4$ | $S_4$  | $u_5$ | $S_5$  |
|------|------------|------------------|-------|--------|-------|--------|-------|--------|-------|--------|-------|--------|
| (1)  | 1.00       | 1.62             | 5.12  | -17.57 | 8.42  | -23.81 | 11.62 | -27.96 | 14.80 | -31.08 | 17.96 | -33.60 |
| (2A) | 0.71       | 2.04             | 6.66  | -33.22 | 9.33  | -41.35 | 12.08 | -43.67 | 15.07 | -44.88 | 18.17 | -46.79 |
| (2B) | 0.69       | 2.06             | 6.97  | -30.96 | -     | -      | 11.66 | -37.59 | 15.12 | -43.71 | 18.21 | -46.48 |
| (3A) | 0.74       | 2.00             | 6.51  | -34.02 | 9.06  | -39.78 | 11.86 | -41.02 | 14.89 | -42.72 | 18.02 | -44.52 |
| (3B) | 0.68       | 2.08             | 6.95  | -41.31 | 9.13  | -44.99 | 11.81 | -43.46 | 14.87 | -44.67 | 18.00 | -46.35 |
| (4A) | 0.81       | 1.88             | 5.97  | -26.71 | 8.91  | -32.45 | 11.97 | -36.42 | 15.07 | -39.48 | 18.19 | -41.96 |
| (4B) | 0.71       | 2.06             | 6.72  | -34.68 | 9.35  | -39.79 | 12.26 | -43.01 | 15.32 | -45.83 | 18.38 | -48.25 |
| (5A) | 0.88       | 1.82             | 5.71  | -30.77 | 8.35  | -28.38 | 11.58 | -31.75 | 14.77 | -34.71 | 18.00 | -37.18 |
| (5B) | 0.84       | 1.86             | 5.85  | -35.57 | 8.34  | -29.35 | 11.57 | -32.51 | 14.77 | -35.43 | 17.94 | -37.87 |
| (5C) | 0.80       | 1.90             | 6.03  | -45.48 | 8.31  | -30.50 | 11.55 | -33.39 | 14.76 | -36.26 | 17.94 | -38.68 |
| (6A) | 0.81       | 1.91             | 6.10  | -30.01 | 8.89  | -33.18 | 11.93 | -36.92 | 15.03 | -39.88 | 18.15 | -42.31 |
| (6B) | 0.71       | 2.03             | 6.63  | -40.93 | 8.96  | -36.94 | 12.03 | -40.52 | 15.11 | -43.36 | 18.22 | -45.73 |
| (7A) | 0.80       | 1.92             | 6.18  | -30.28 | 8.79  | -38.42 | 11.65 | -35.72 | 14.84 | -39.58 | 17.97 | -40.96 |
| (7B) | 0.80       | 1.92             | 6.14  | -31.83 | 8.70  | -35.95 | 11.65 | -35.49 | 14.83 | -39.03 | 17.97 | -40.55 |
| (7C) | 0.80       | 1.91             | 6.11  | -33.21 | 8.62  | -34.06 | 11.66 | -35.35 | 14.82 | -38.40 | 17.97 | -40.29 |

$$u = \frac{2\pi}{\lambda} a \sin \theta$$

S = Sidelobe dB from Beam Peak

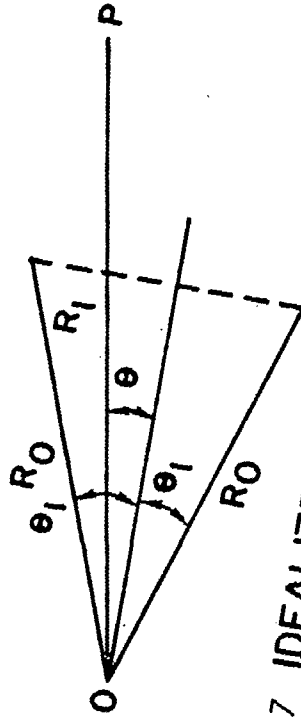


FIG. 3.7 IDEALIZED HORN GEOMETRY

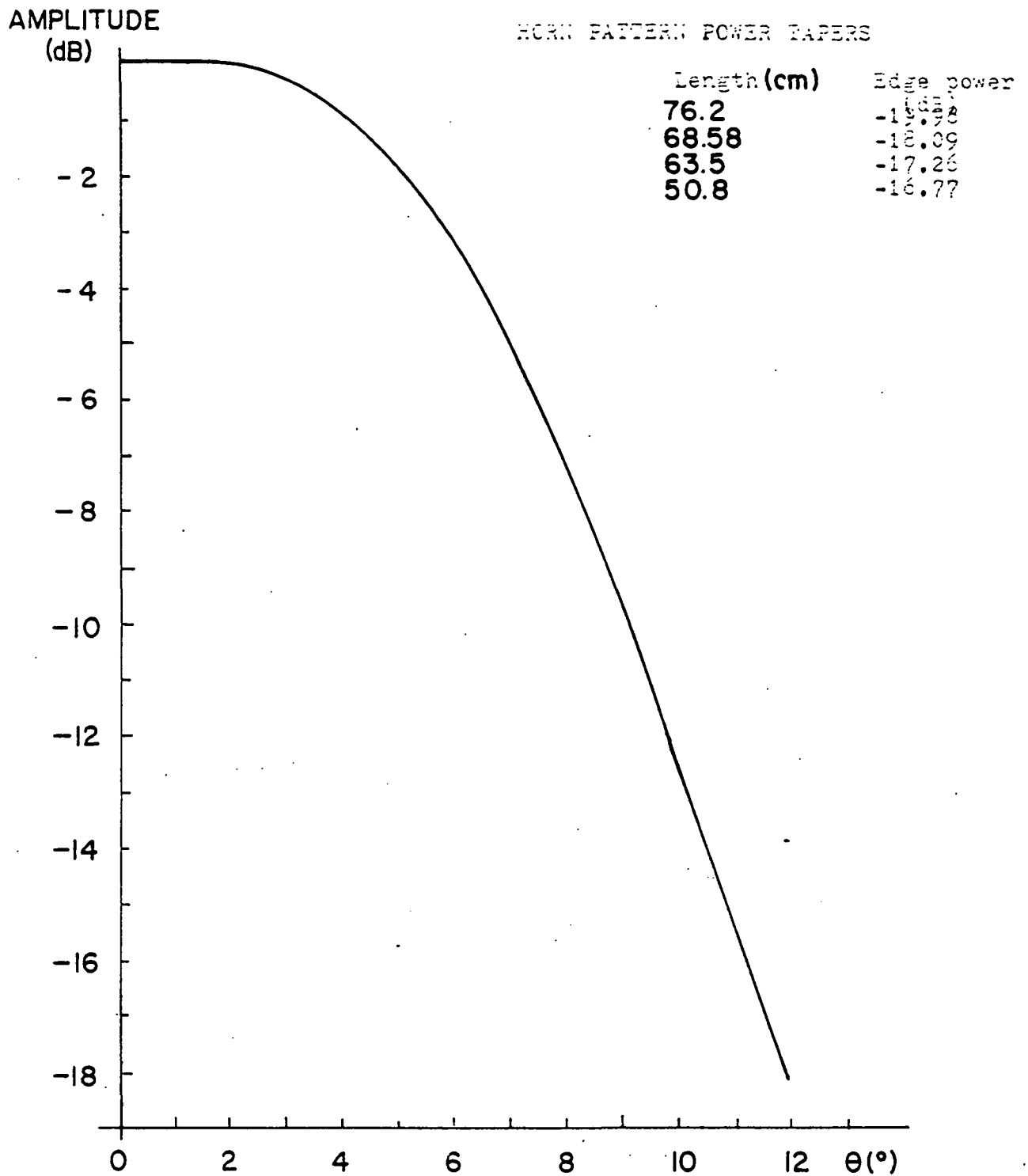


FIG. 3.8 AMPLITUDE FUNCTION OF 68.58 cm, 12° CORRUGATED HORN

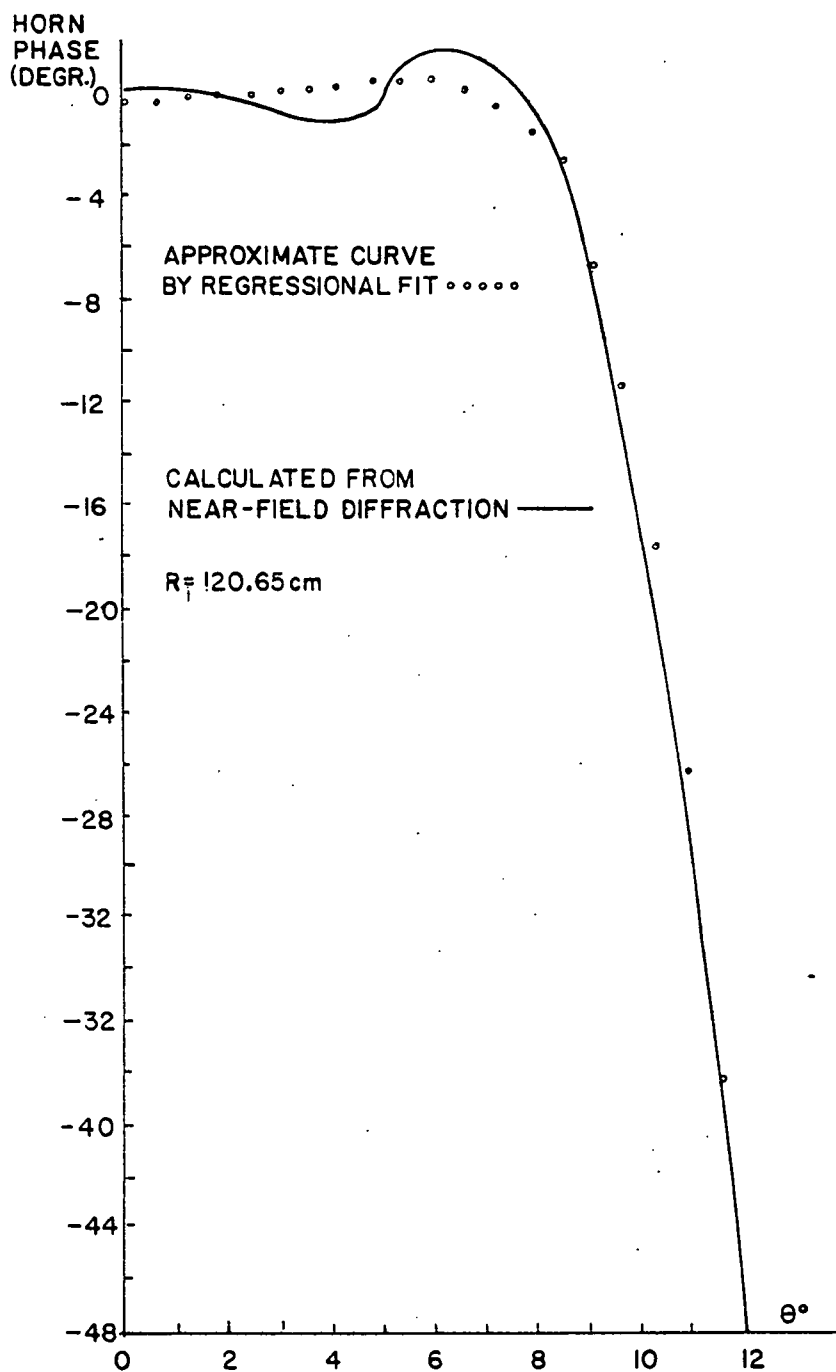
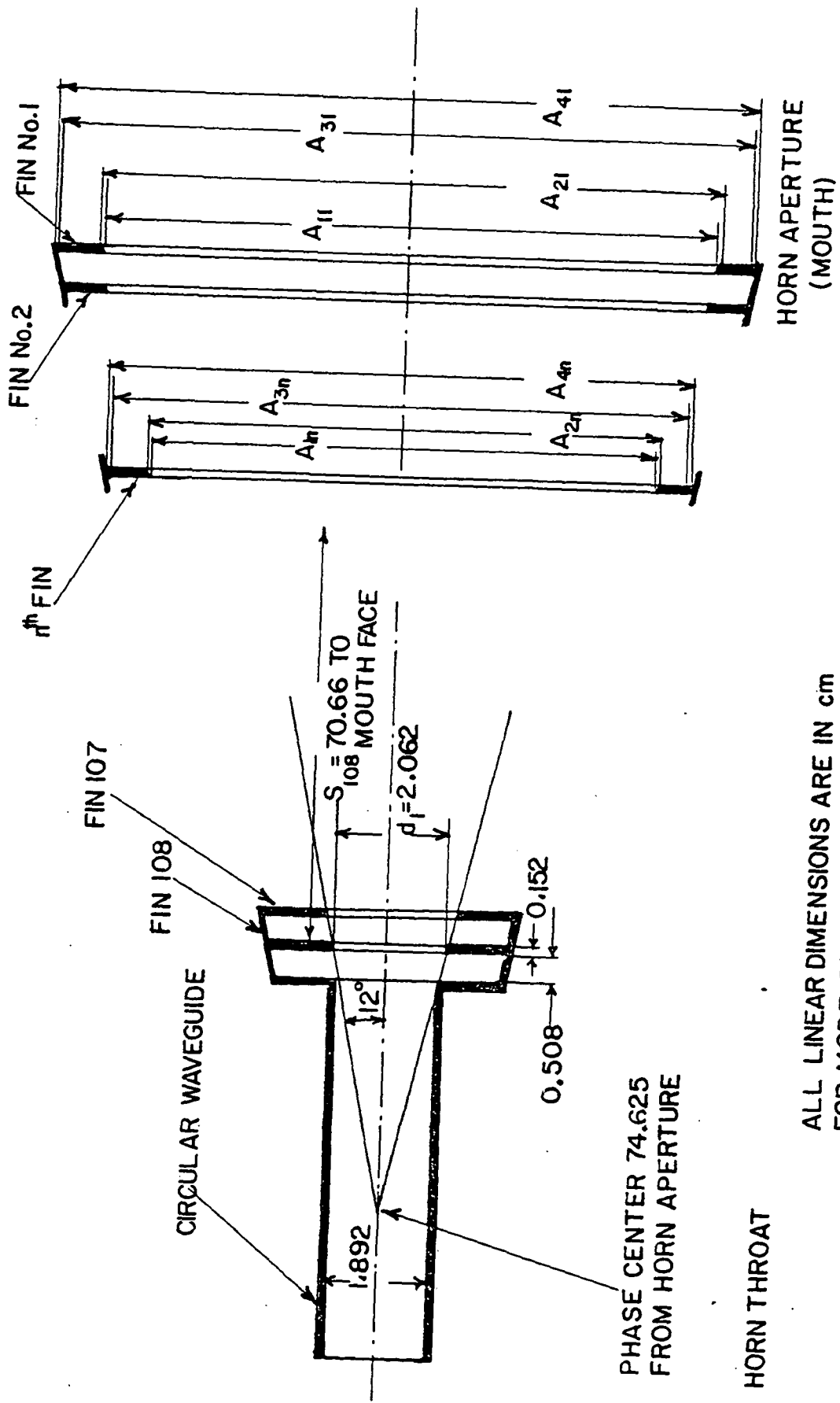


FIG.3.9 CONICAL HORN PHASE CURVE FOR  
76.2 cm LONG HORN



PHASE CENTER 74.625 FROM HORN APERTURE

HORN THROAT

ALL LINEAR DIMENSIONS ARE IN cm FOR MORE DIMENSIONS SEE TABLE 5.1

FIG.3.10 CROSS SECTION OF CORRUGATED CONICAL HORN

TABLE 5.1  
DIMENSIONS--CORRUGATED CONICAL HORN

| Fin No.<br>n             | $S_n$                                  | $A_{1n}$ | $A_{2n}$ | $A_{3n}$ | $A_{4n}$ | $2d_n$ |
|--------------------------|--|----------|----------|----------|----------|--------|
| 1 (Horn<br>mouth)        | 0.0                                    | 32.103   | 32.167   | 33.437   | 33.373   | 1.270  |
| 2                        | 0.660                                  | 31.821   | 31.887   | 33.157   | 33.091   | 1.270  |
| 3                        | 1.321                                  | 31.542   | 31.605   | 32.875   | 32.812   | 1.270  |
| ⋮                        |  |          |          |          |          |        |
|                          | Calculate dimensions from Equation 5.1 |          |          |          |          |        |
| ⋮                        |  |          |          |          |          |        |
| 98                       | 64.059                                 | 4.869    | 4.935    | 6.205    | 6.139    | 1.270  |
| 99                       | 64.719                                 | 4.590    | 4.653    | 6.101    | 5.946    | 1.356  |
| 100                      | 65.380                                 | 4.308    | 4.374    | 5.817    | 5.751    | 1.443  |
| 101                      | 66.040                                 | 4.028    | 4.092    | 5.621    | 5.558    | 1.529  |
| 102                      | 66.700                                 | 3.747    | 3.813    | 5.428    | 5.362    | 1.615  |
| 103                      | 67.361                                 | 3.467    | 3.531    | 5.232    | 5.169    | 1.702  |
| 104                      | 68.021                                 | 3.185    | 3.251    | 5.039    | 4.973    | 1.788  |
| 105                      | 68.682                                 | 2.906    | 2.969    | 4.844    | 4.780    | 1.875  |
| 106                      | 69.342                                 | 2.624    | 2.690    | 4.651    | 4.585    | 1.961  |
| 107                      | 70.002                                 | 2.344    | 2.408    | 4.455    | 4.392    | 2.047  |
| 108                      | 70.663                                 | 2.062    | 2.129    | 4.262    | 4.196    | 2.134  |
| (At wave-<br>guide port) | 71.323                                 |          | 1.892    | 4.026    |          | 2.134  |

Horn semi-flare angle 12 degrees  
Symbols defined in text and FIG. 5.1  
All dimensions in centimeters

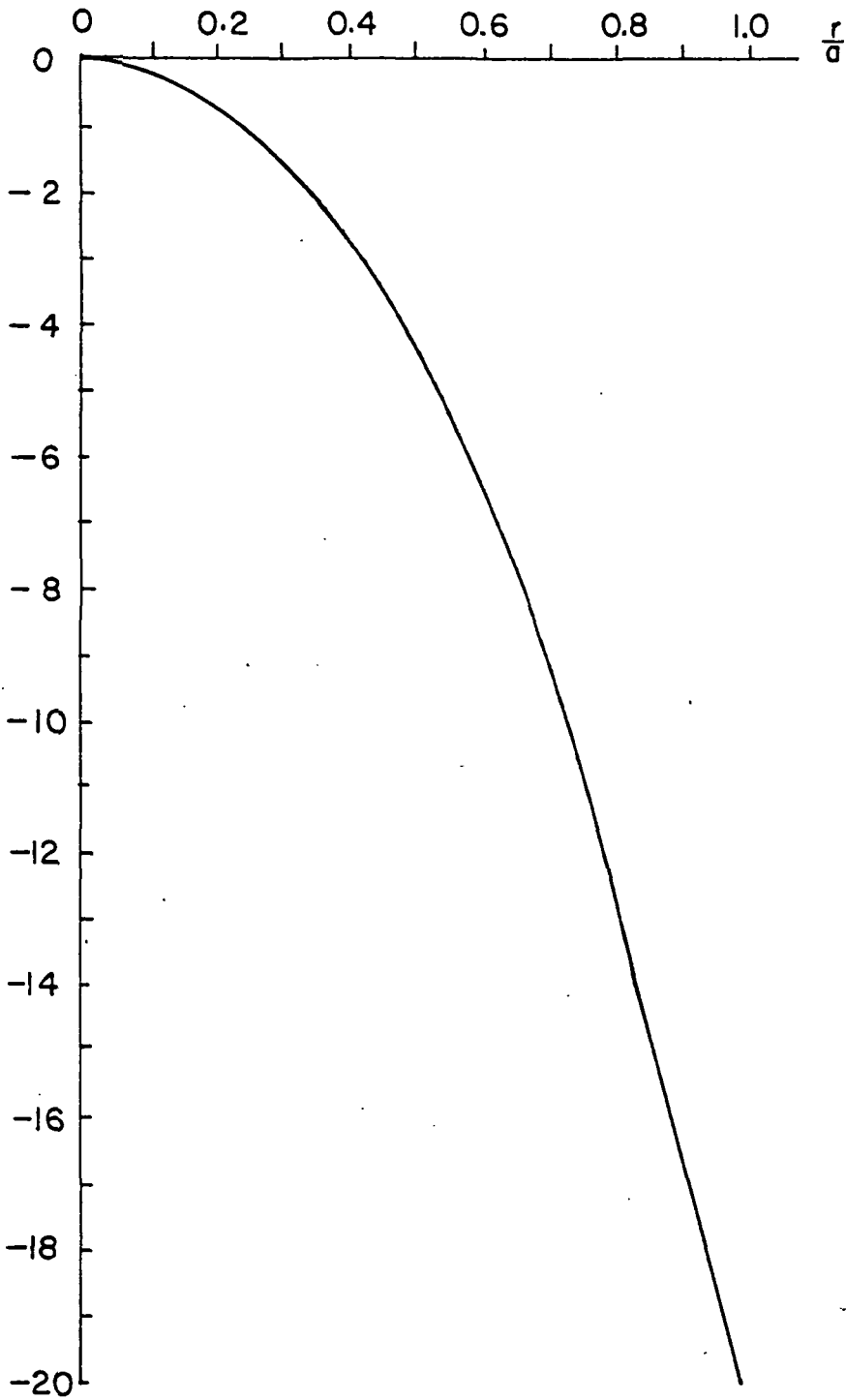


FIG.3.11 ILLUMINATION OF CIRCULAR APERTURE  
BY 76.2 cm LONG CORRUGATED HORN

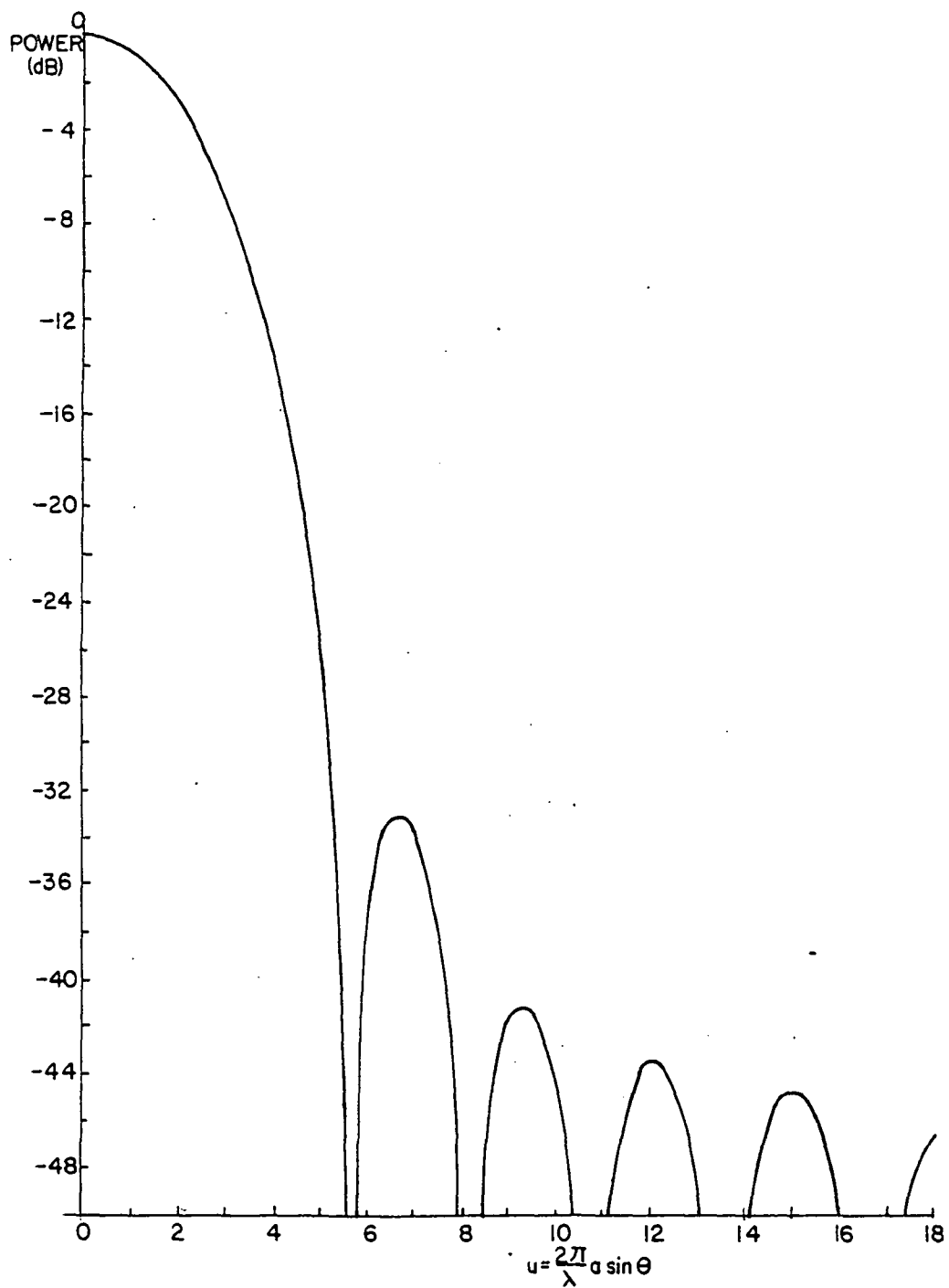


FIG.3.12 DIFFRACTION OF CIRCULAR APERTURE ILLUMINATED BY A 76.2 cm, 12° CORRUGATED HORN- NO PHASE ERROR

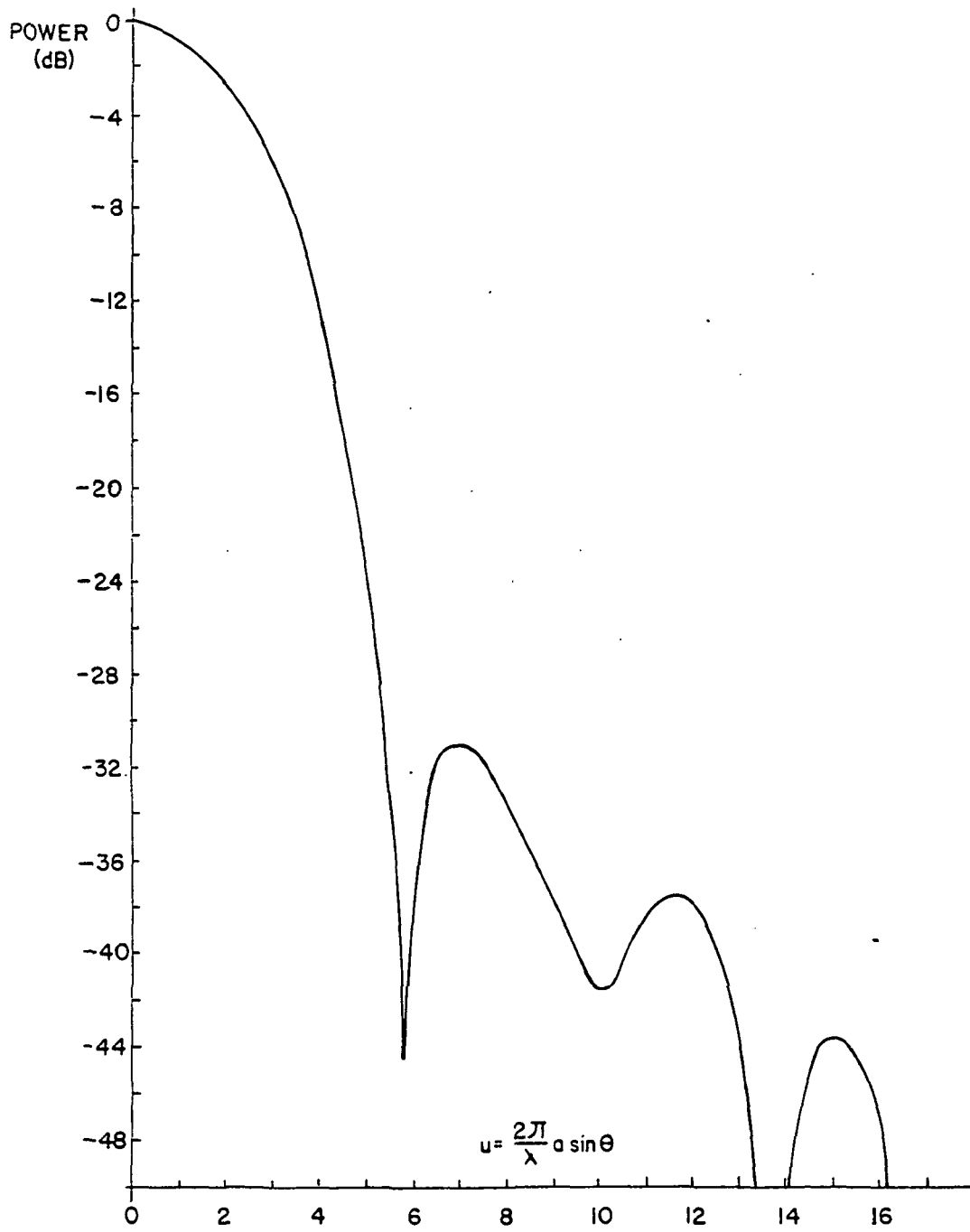


FIG. 3.13 DIFFRACTION PATTERN OF CIRCULAR APERTURE ILLUMINATED BY A 76.2 cm, 12° CORRUGATED HORN; PHASE ERROR INCLUDED

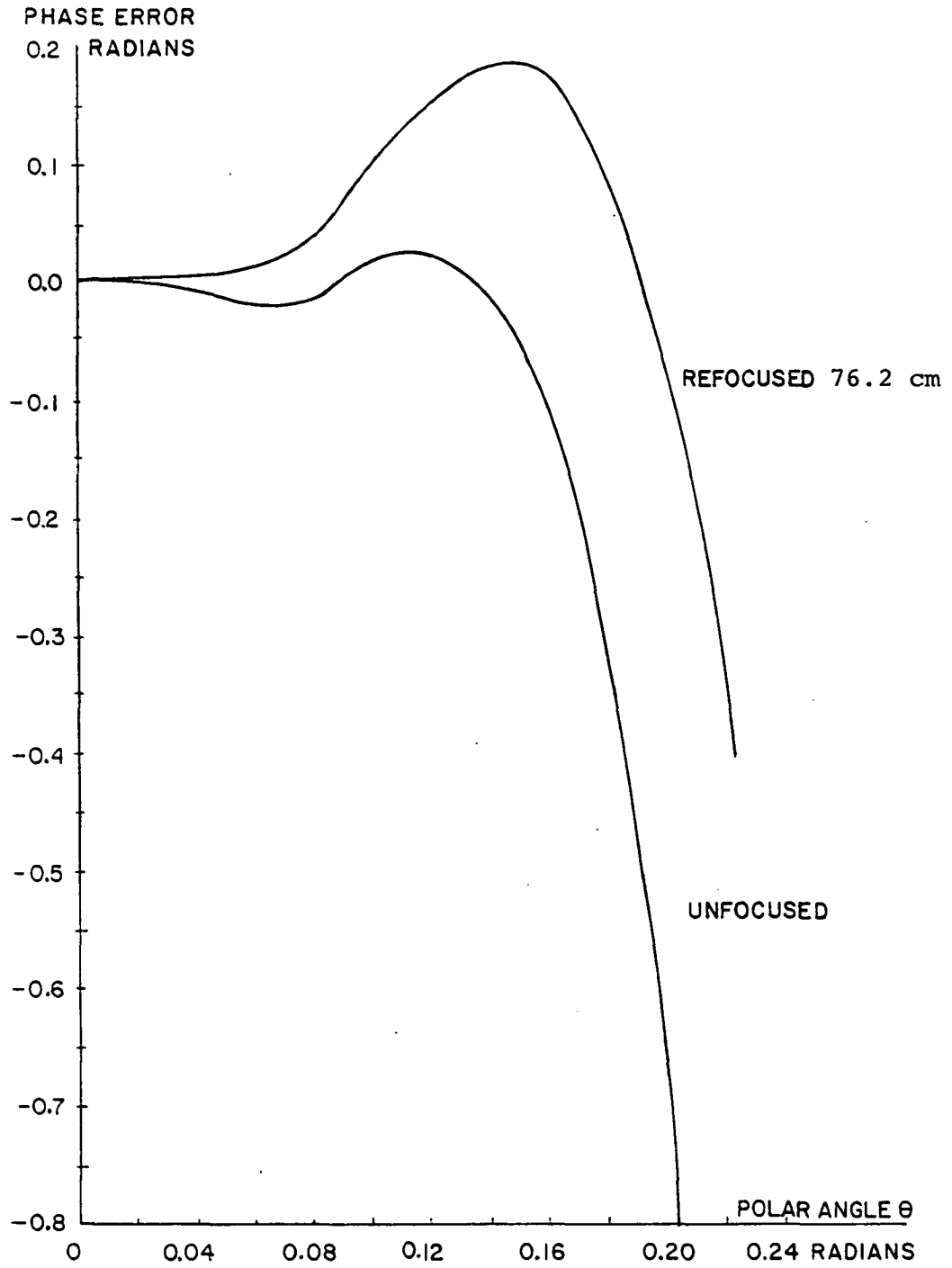


FIG.3. ANALYTIC REFOCUSING TO CORRECT HORN PHASE

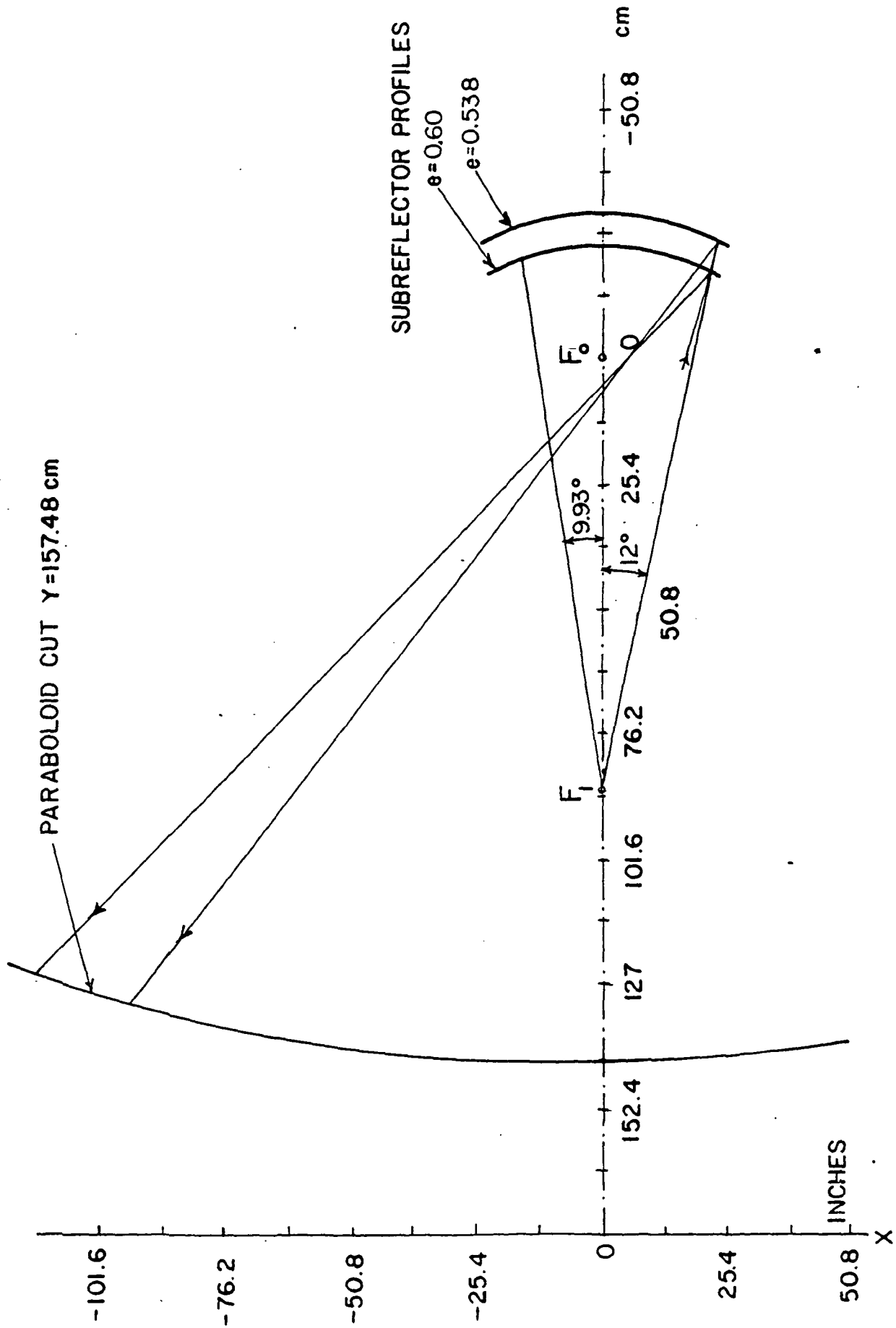


FIG. 3.15 CORRECTING HORN EDGE RAYS BY INCREASING ECCENTRICITY

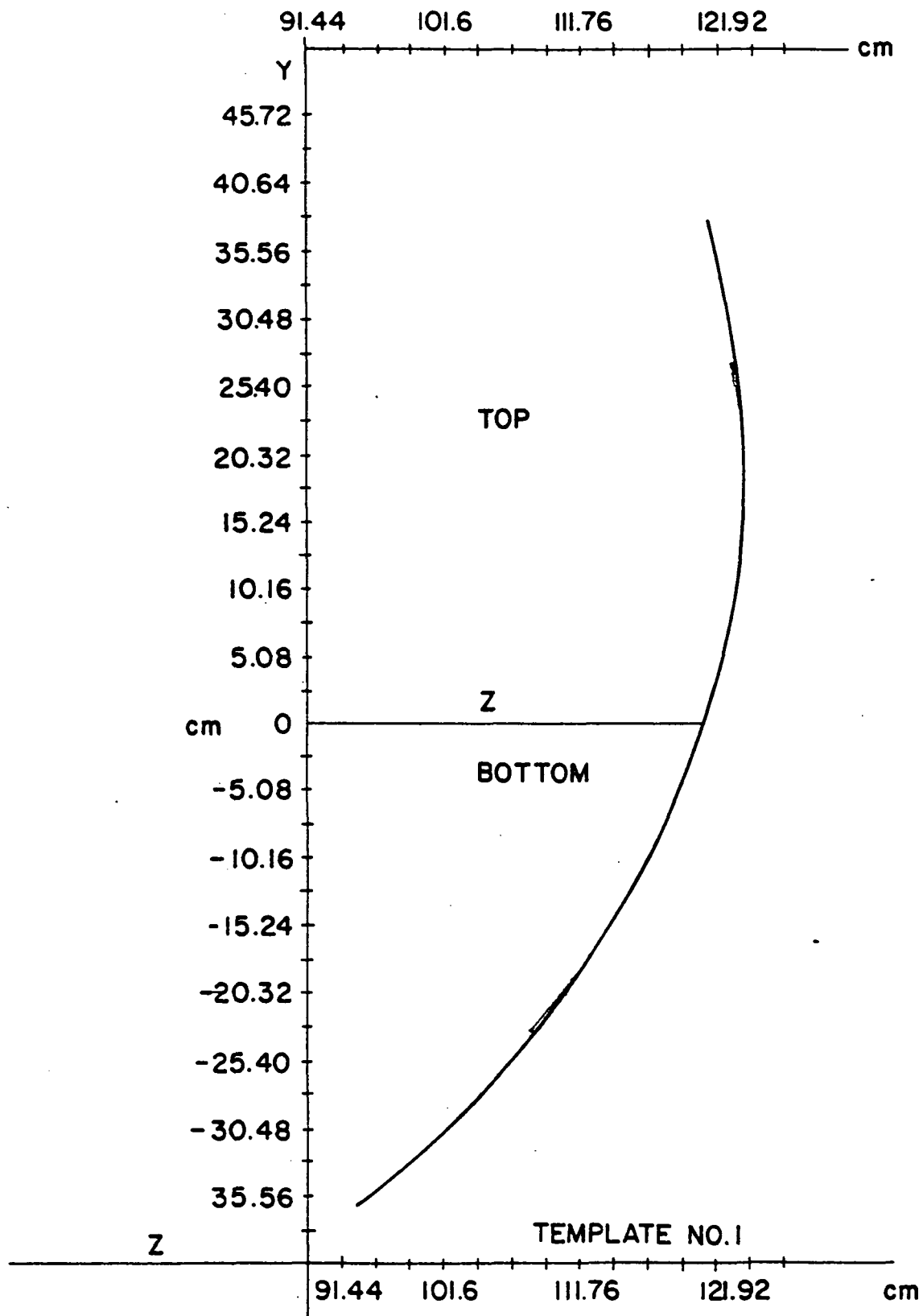


FIG. 3.16 TEMPLATE CONTOUR (Y-CUT) THROUGH MIDDLE OF SHAPED SUBREFLECTOR

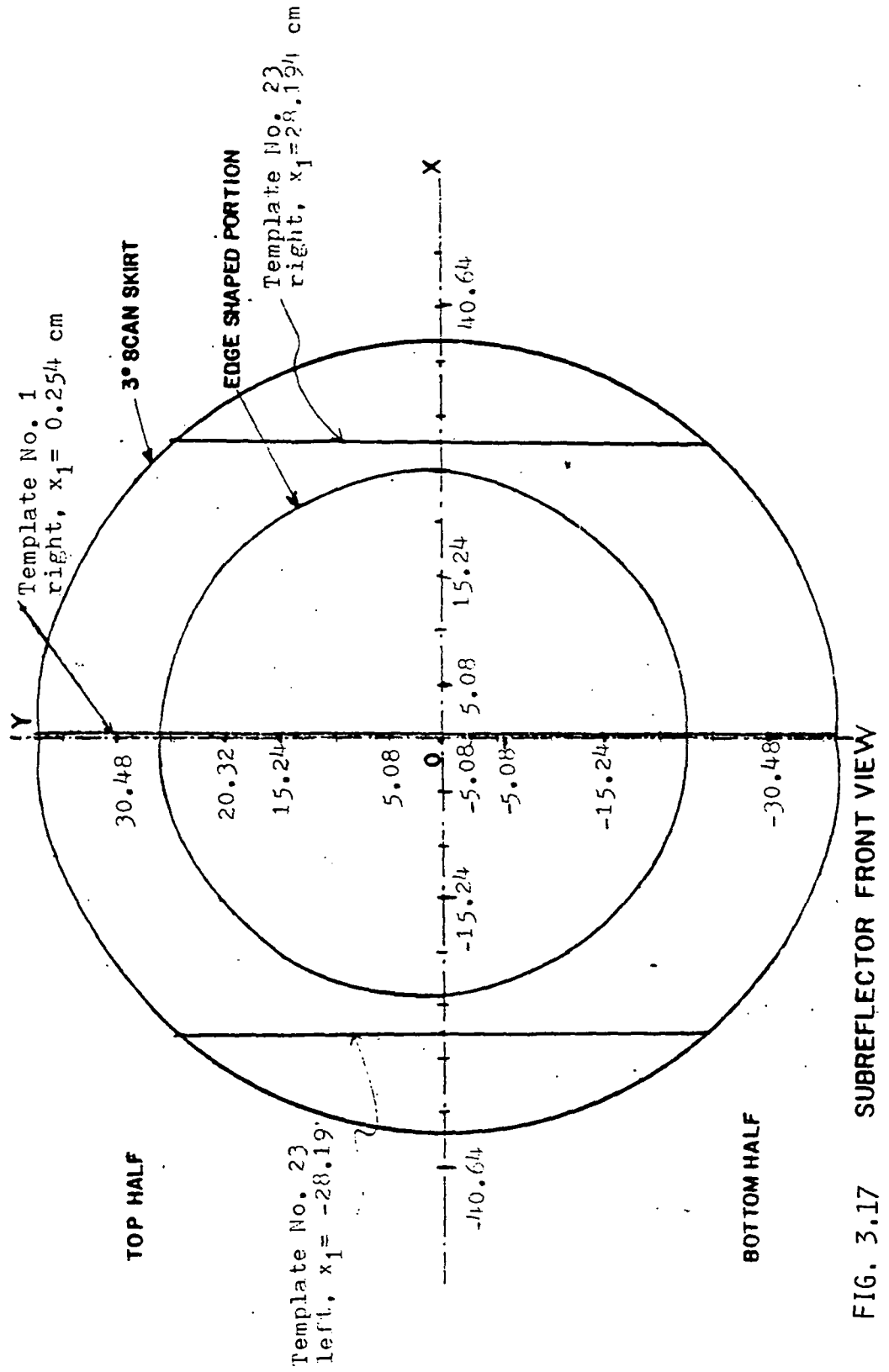


FIG. 3.17 SUBREFLECTOR FRONT VIEW

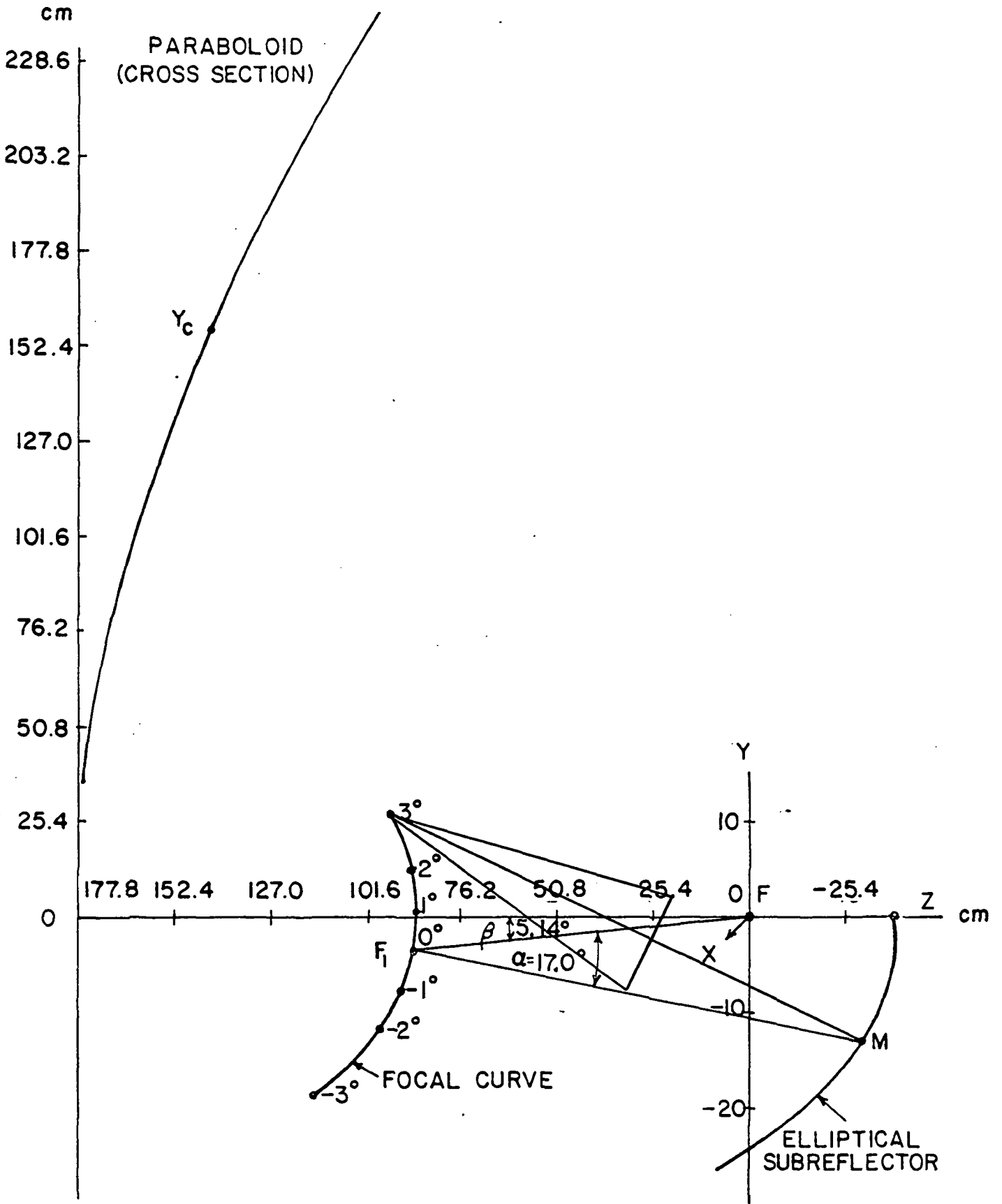


FIG. 3.18 BEST ELEVATION PLANE FOCAL CURVE

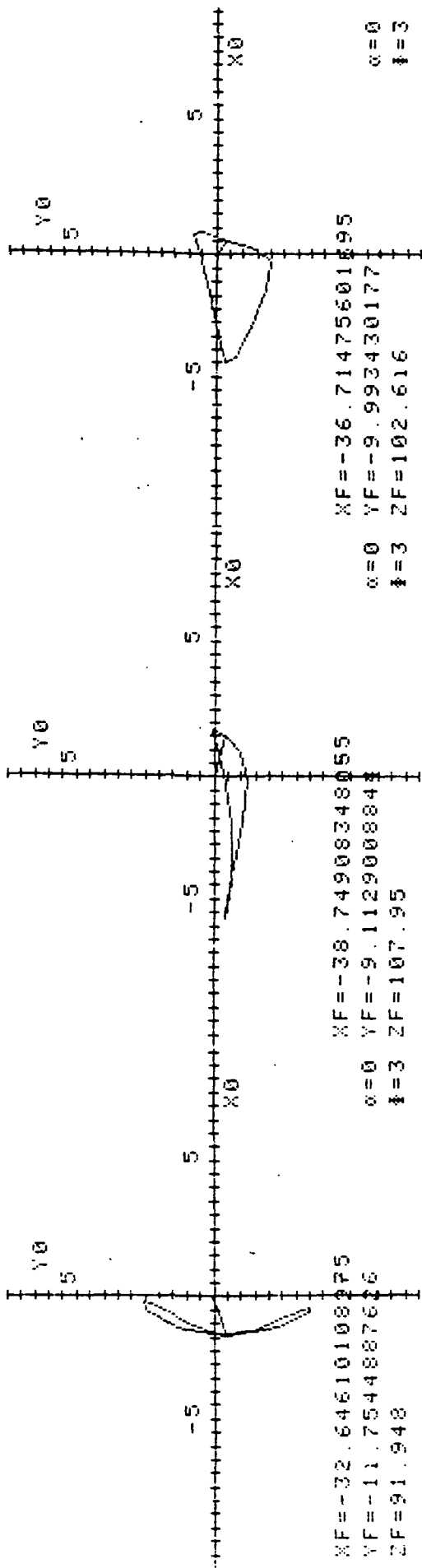


FIG. 3.19A TRACES OF THE DISH RIM RAYS ON THE "SCREEN" FOR AZIMUTH SCAN OF  $3^\circ$

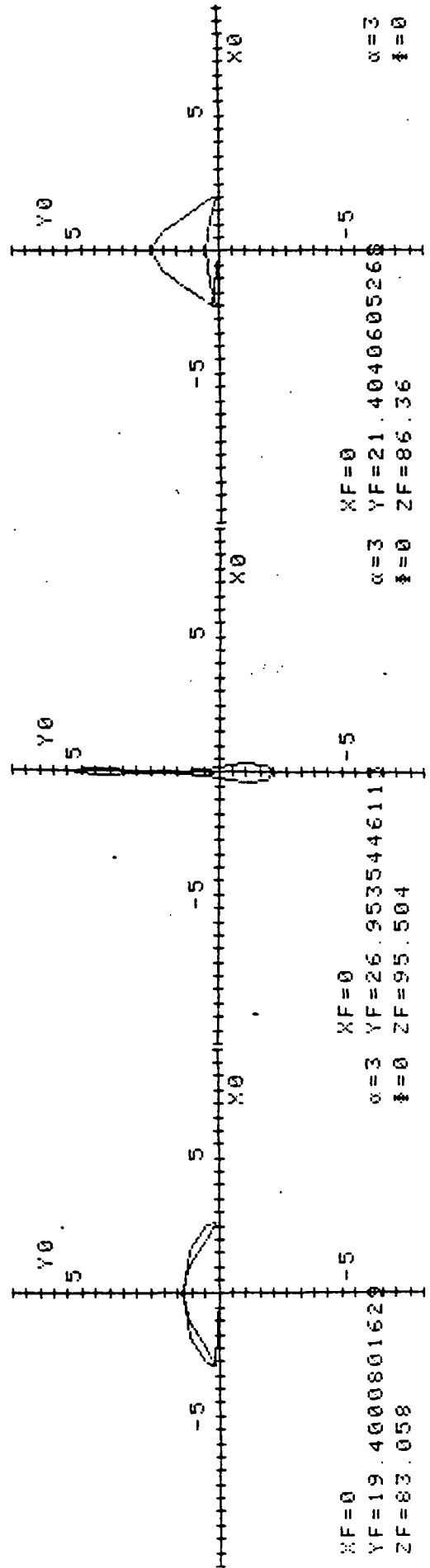


FIG. 3.19B TRACES OF THE DISH RIM RAYS ON THE "SCREEN" FOR ELEVATION SCAN OF  $3^\circ$

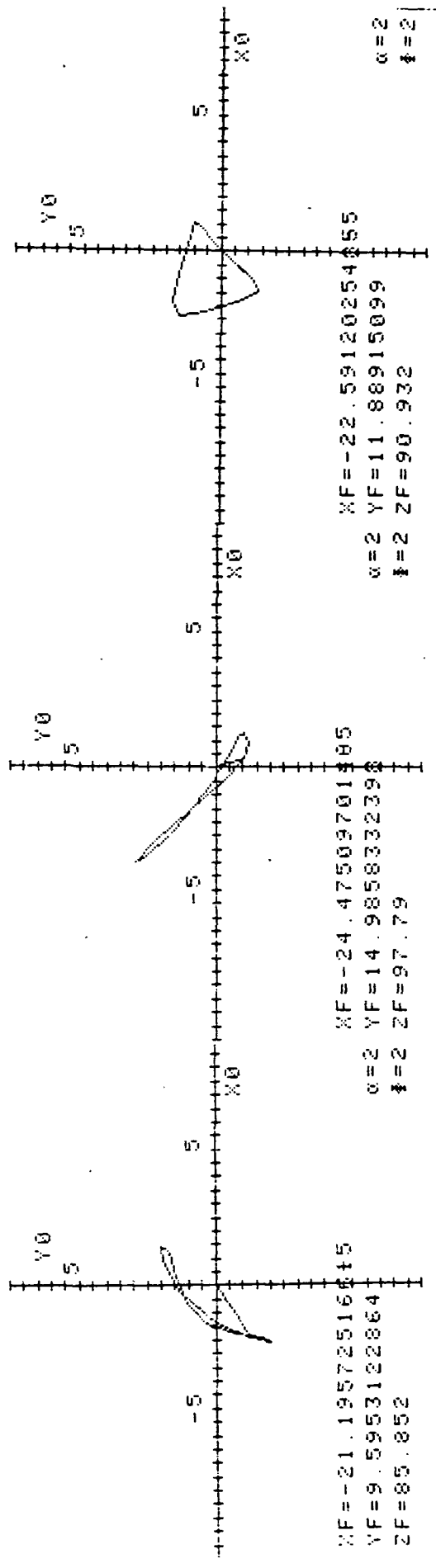


FIG. 3.19C TRACES OF THE DISH RIM RAYS ON THE "SCREEN FOR DIRECTION OF ELEVATION ANGLE 2° AND AZIMUTH ANGLE 2°

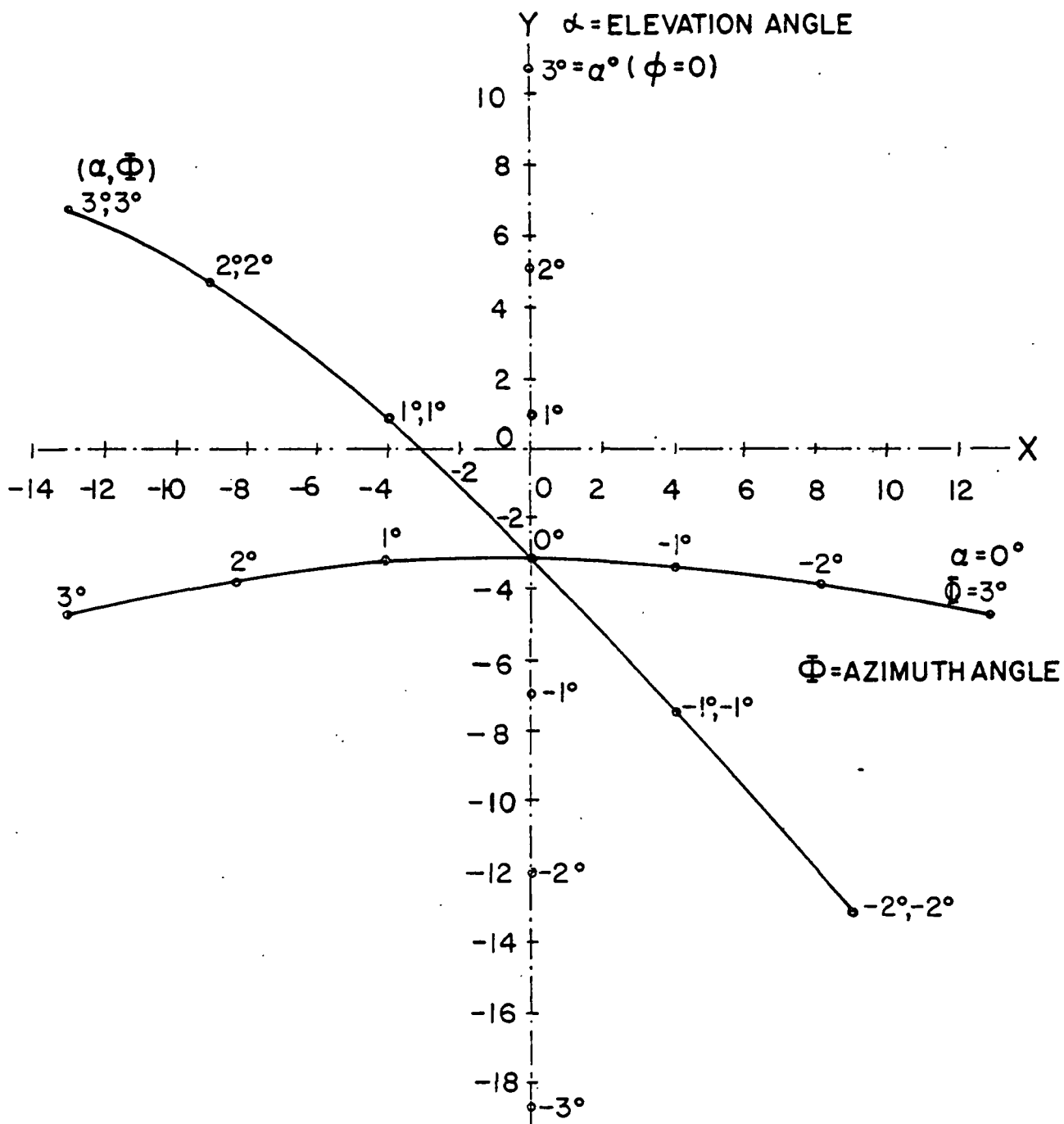


FIG.3.20 FOCAL PLANE X-Y PLOT

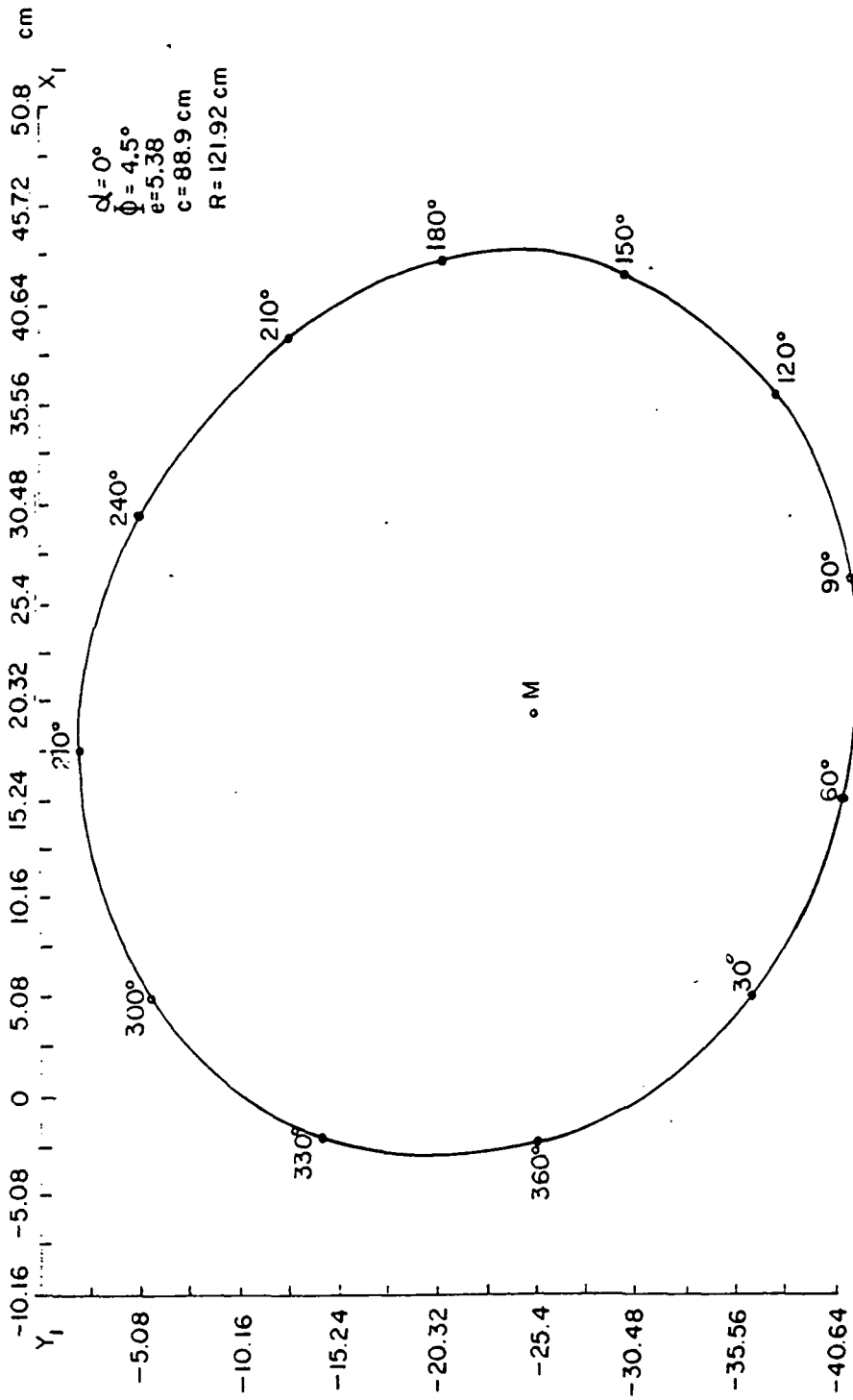


FIG. 3.21 "FOOT PRINT" DISH EDGE ON ELLIPSOID SURFACE

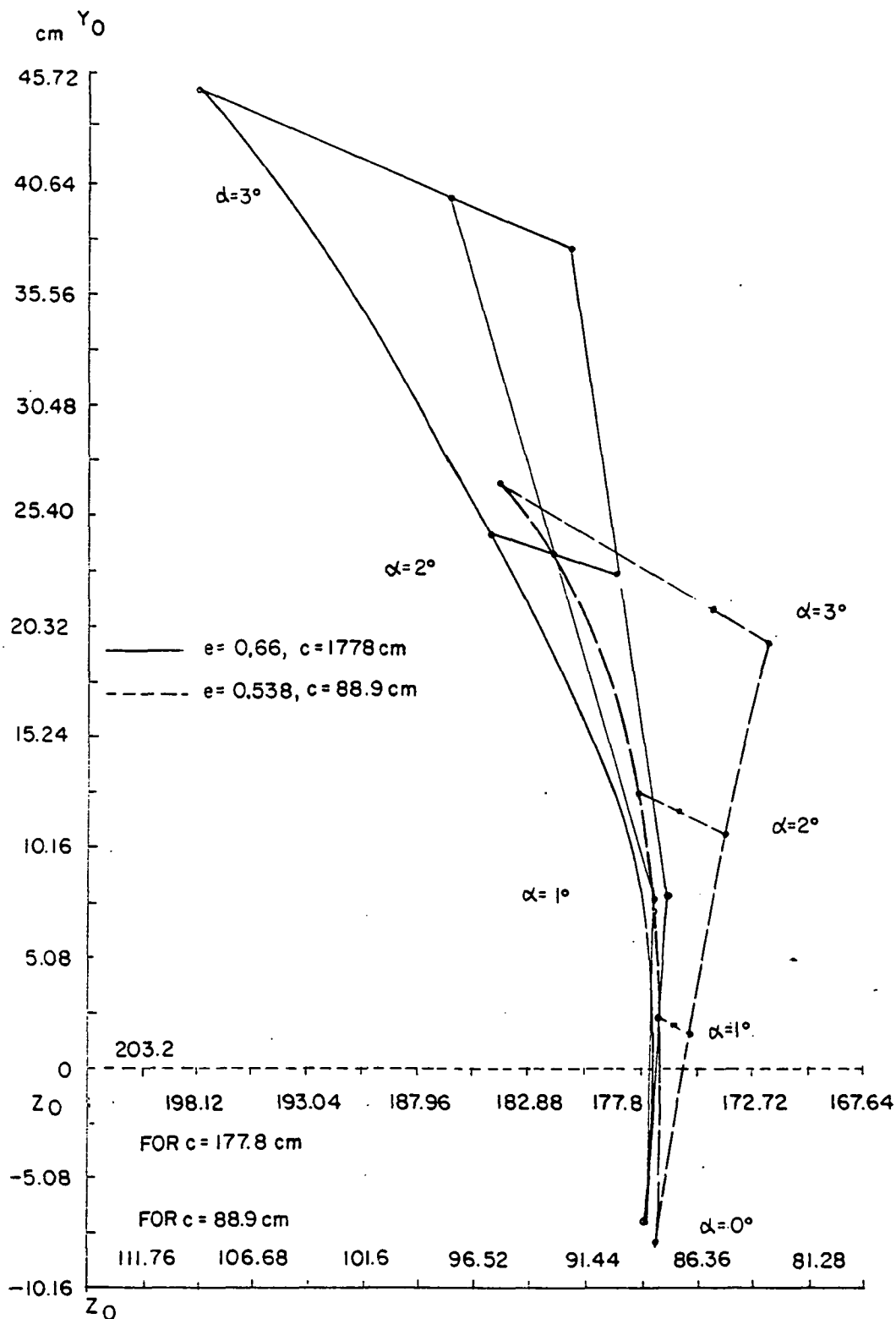


FIG. 3.22 FOCAL REGION COMPARISONS ELEVATION SCAN

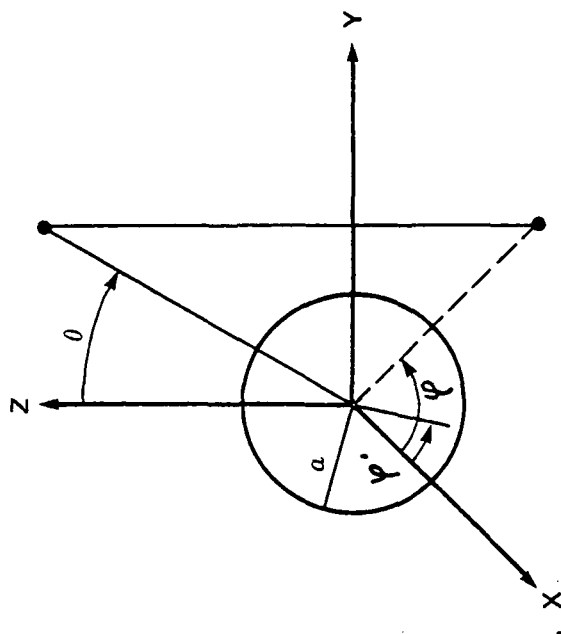


FIG. 3.23 COORDINATE SYSTEM FOR CIRCULAR APERTURE DIFFRACTION PATTERNS

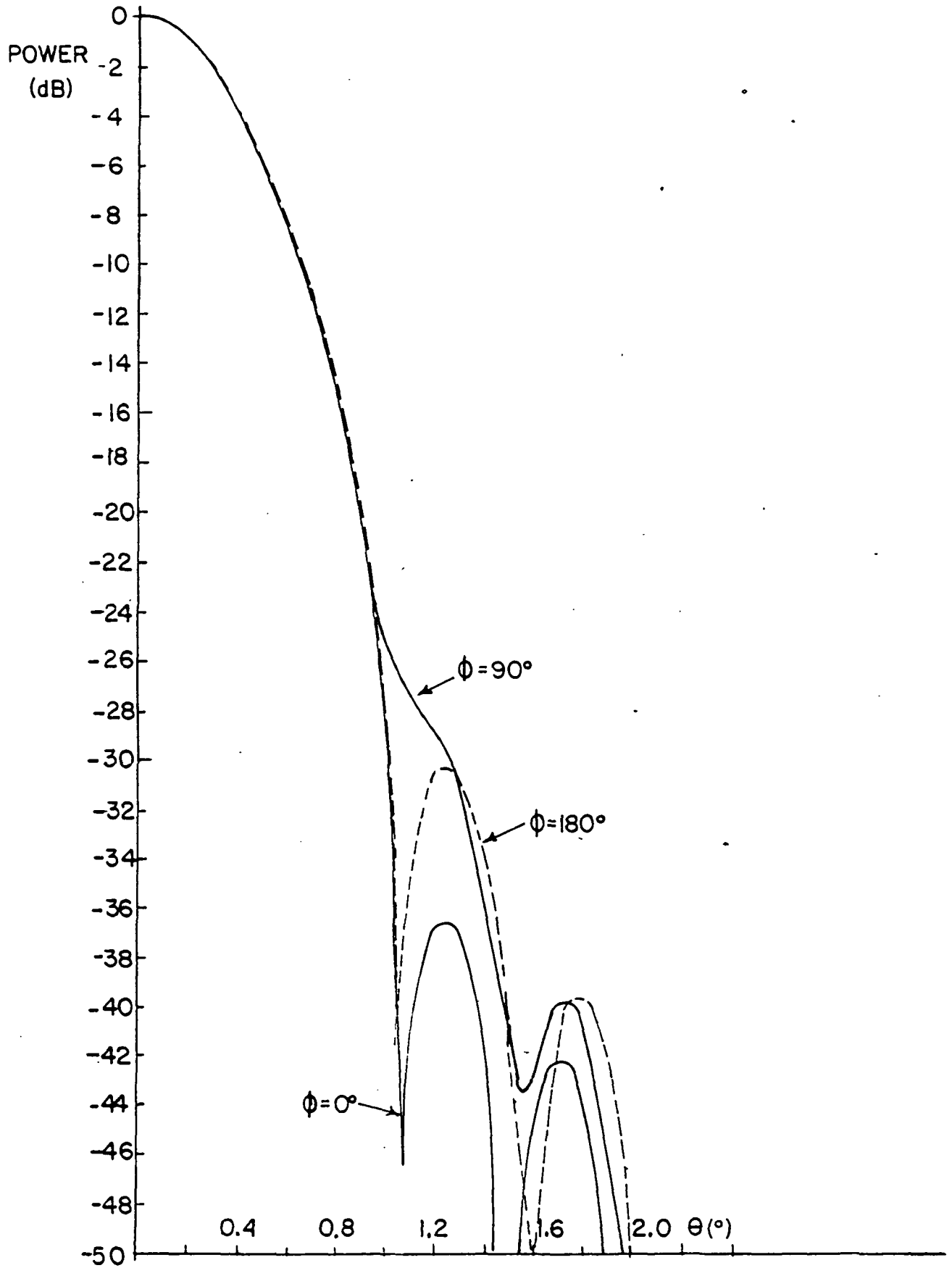


FIG. 3.24 DIFFRACTION PATTERN SCANNED  $3^\circ$  IN AZIMUTH FOCUSED AT BEST AZIMUTH FOCUS

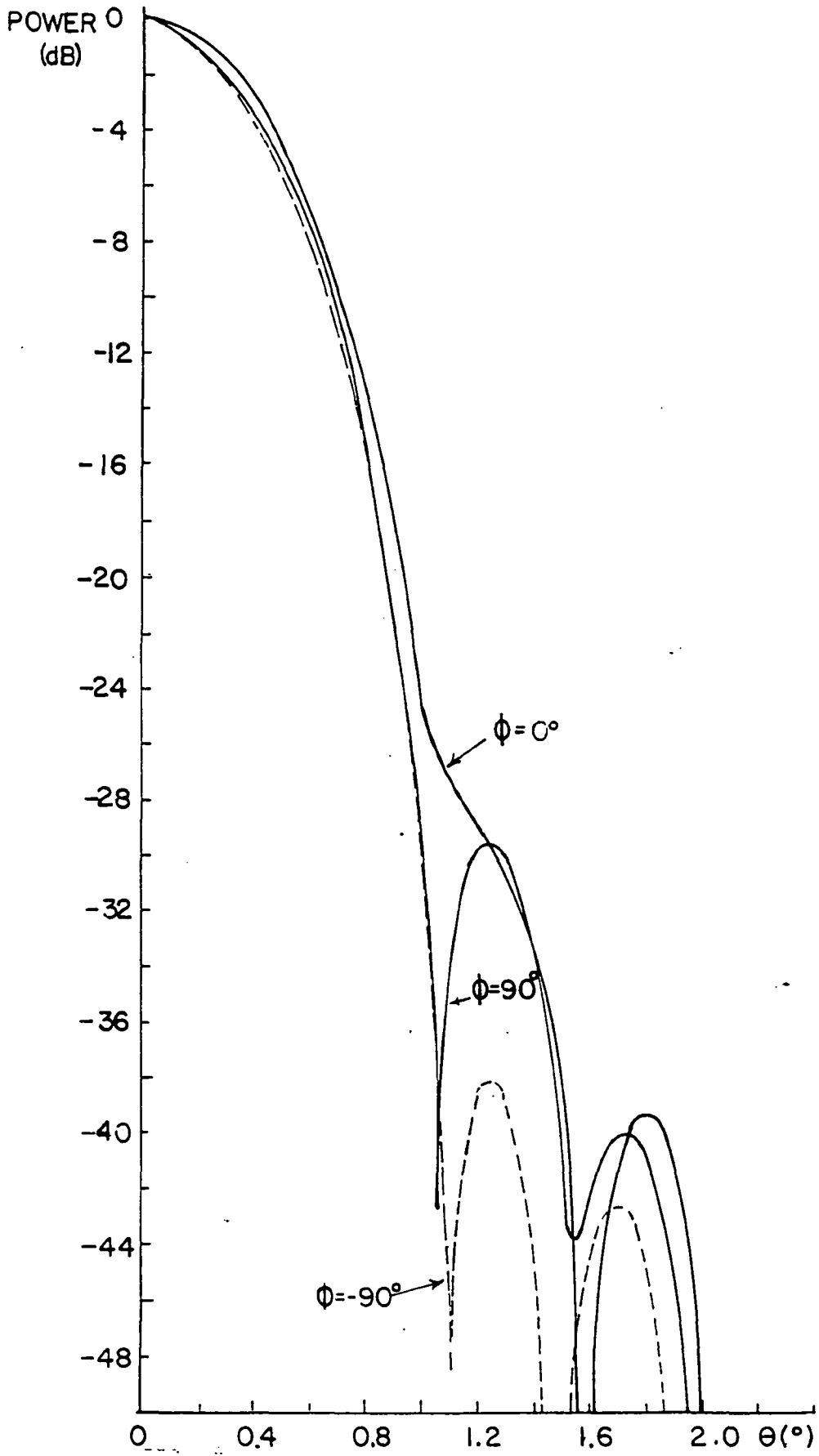


FIG. 3.25 DIFFRACTION PATTERN SCANNED 3° IN ELEVATION, FOCUSED AT BEST ELEVATION FOCUS

TABLE 9.1

## FOCAL PLANE DATA

Antenna parameters:  $f=177.8$  cm,  $y_c=157.48$  cm  
 $c=88.9$  cm,  $e=0.538$

## ELEVATION SCAN

| ELEV.      | AZIM.     | $X_{Faz}$ | $Y_{Faz}$ | $Z_{Faz}$ | $Z_{Fel}$ | $Z_{Fcir}$ | $d/1^\circ$ | OPT         | BW <sub>cir</sub> |
|------------|-----------|-----------|-----------|-----------|-----------|------------|-------------|-------------|-------------------|
| $0^\circ$  | $0^\circ$ | 0 cm      | -7.968    | 88.54     | 88.54     | 88.54      | -           | $0^\circ$   |                   |
| 1          | 0         | 0         | 2.012     | 87.63     | 87.38     | 87.63      | 9.98        | $.02^\circ$ |                   |
| 2          | 0         | 0         | 12.766    | 89.41     | 85.09     | 87.88      | 10.74       | .07         |                   |
| 3          | 0         | 0         | 26.954    | 95.50     | 83.06     | 86.36      | 14.18       | .143        |                   |
| $-1^\circ$ | $0^\circ$ | 0         | -18.293   | 91.95     | 91.44     | 91.44      | 10.32       | $.01^\circ$ |                   |
| -2         | 0         | 0         | -30.531   | 100.08    | 98.04     | 99.06      | 12.49       | .04         |                   |
| -3         | 0         | 0         | -47.907   | 115.57    | 113.28    | 114.30     | 17.37       | .07         |                   |

## AZIMUTH SCAN

|           |           |        |         |       |        |        |       |             |
|-----------|-----------|--------|---------|-------|--------|--------|-------|-------------|
| $0^\circ$ | $0^\circ$ | 0      | -7.968  | 88.54 | 88.54  | 88.54  | -     | $0^\circ$   |
| 0         | 1         | -10.26 | -8.255  | 89.41 | 90.17  | 89.66  | 11.18 | $.02^\circ$ |
| 0         | 2         | -20.93 | -9.550  | 90.17 | 96.52  | 92.71  | 10.67 | .06         |
| 0         | 3         | -32.64 | -11.754 | 91.95 | 107.95 | 102.62 | 11.71 | .19         |
| 0         | 4         | -46.38 | -15.113 | 95.25 | 137.16 | 11.76  | 13.74 | .3          |
| 0         | 5         | -62.61 | -20.244 | 99.06 |        |        | 16    |             |

 $45^\circ$  CUTS

|            |            | $X_{Fcir}$ | $Y_{Fcir}$ |        |        |        |   |             |
|------------|------------|------------|------------|--------|--------|--------|---|-------------|
| $1^\circ$  | $1^\circ$  | -10.44     | 1.762      | 87.12  | 89.41  | 88.39  | - | $.01^\circ$ |
| 2          | 2          | -22.59     | 11.89      | 85.85  | 97.79  | 90.93  | - | .14         |
| 3          | 3          | -32.94     | 16.79      | 83.82  | 121.92 | 92.71  | - | .36         |
| $-1^\circ$ | $-1^\circ$ | 10.35      | -18.82     | 93.47  | 91.95  | 92.96  | - | $.03^\circ$ |
| -2         | -2         | 22.94      | -33.31     | 113.03 | 101.60 | 107.95 | - | .1          |

## COMPARISON: OPTICAL BEAM WIDTHS

$e=0.538$   $c=88.9$  cm

$e=0.66$   $c=177.8$  cm

| ELEV.     | $d/1^\circ$ | BW <sub>az</sub> | BW <sub>cir</sub> | BW <sub>el</sub> | $d/1^\circ$ | BW <sub>az</sub> | BW <sub>cir</sub> | BW <sub>el</sub> |
|-----------|-------------|------------------|-------------------|------------------|-------------|------------------|-------------------|------------------|
| $2^\circ$ | 10.16       | $.12^\circ$      | $.06^\circ$       | $.1^\circ$       | 15.24       | $.06^\circ$      | $.04^\circ$       | $.05^\circ$      |
| 3         | 10.16       | .27              | .2                | .33              | 15.24       | .14              | .08               | .18              |

$X_{Faz}$ ,  $Y_{Faz}$ ,  $Z_{Faz}$  are focal point coordinates for best azimuth plane pattern.

$Z_{Fel}$  etc. are focal point for best elevation plane patterns and

$Z_{Fcir}$  etc. are focal points for circle of least confusion.

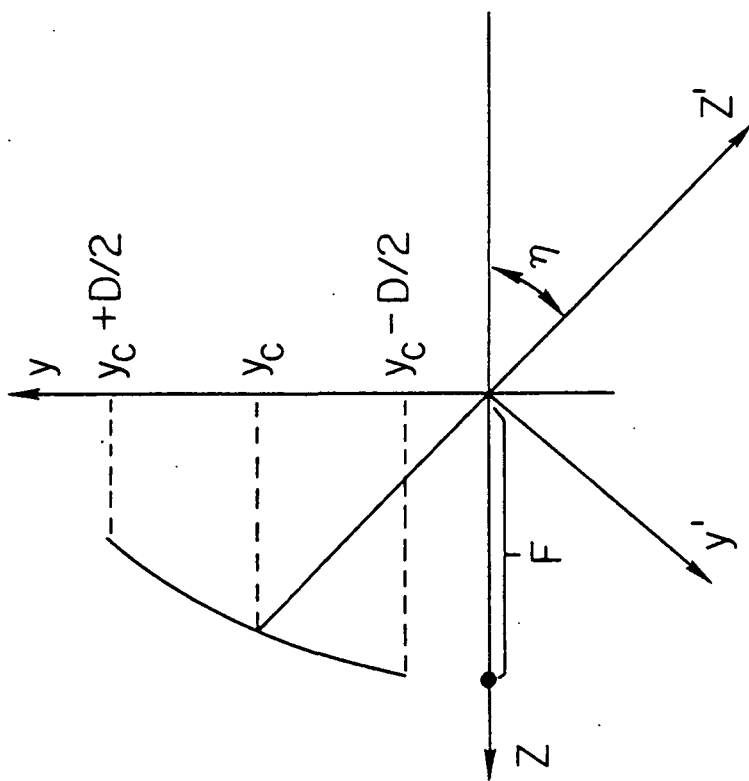


FIG. 3.26 COORDINATE SYSTEMS USED IN DESCRIBING NEAR FIELD DIFFRACTION PATTERNS. THE X-AXIS PROJECTS OUT OF THE PLANE OF THE PAPER

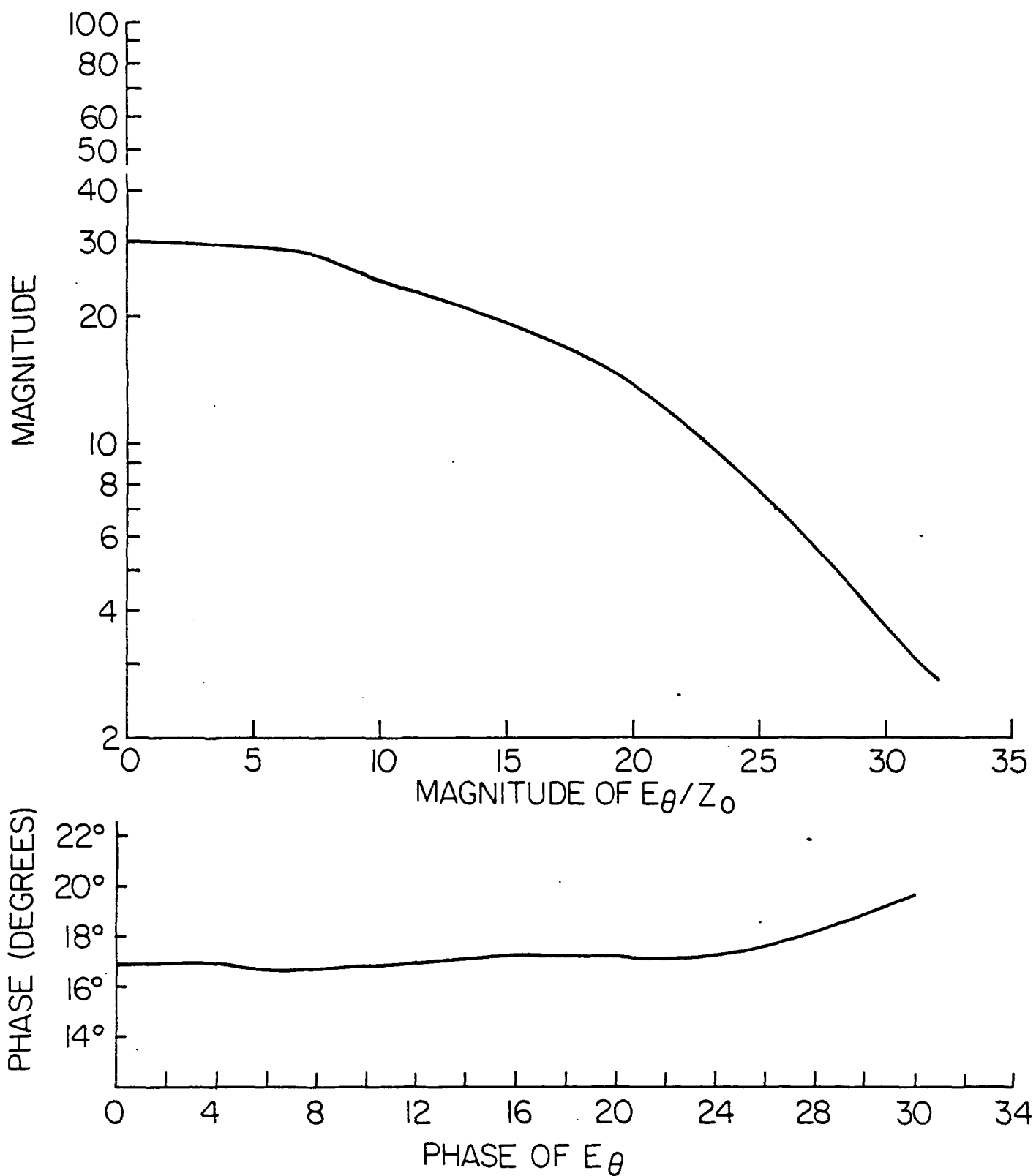
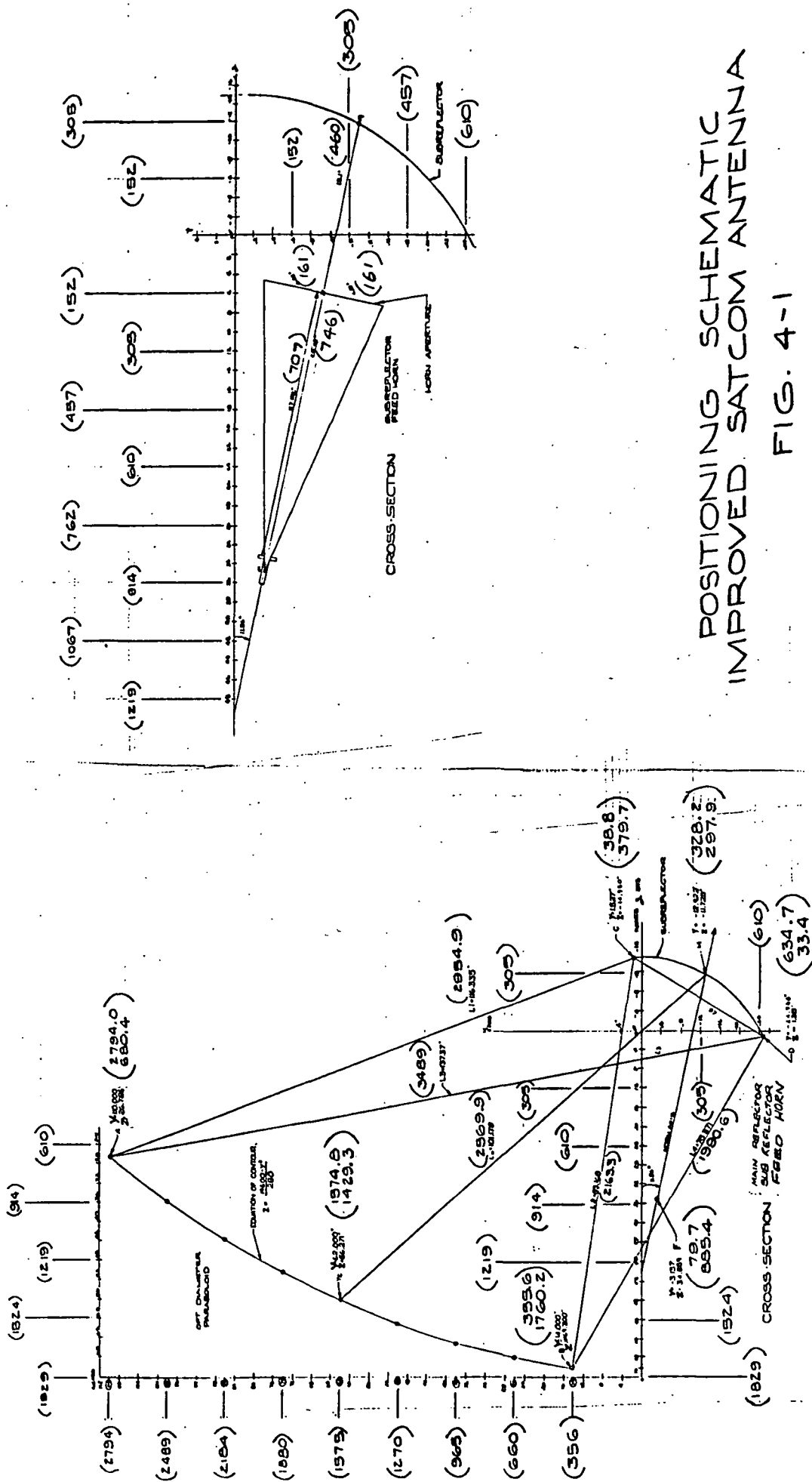


FIG. 3.27 (A,B) AMPLITUDE (TOP) AND PHASE (BOTTOM) FOCAL REGION TANGENTIAL ELECTRIC FIELD FOR A TAPERED PLANE WAVE



POSITIONING SCHEMATIC  
IMPROVED SATCOM ANTENNA  
FIG. 4-1

NUMBERS IN ( ) ARE IN MILLIMETERS

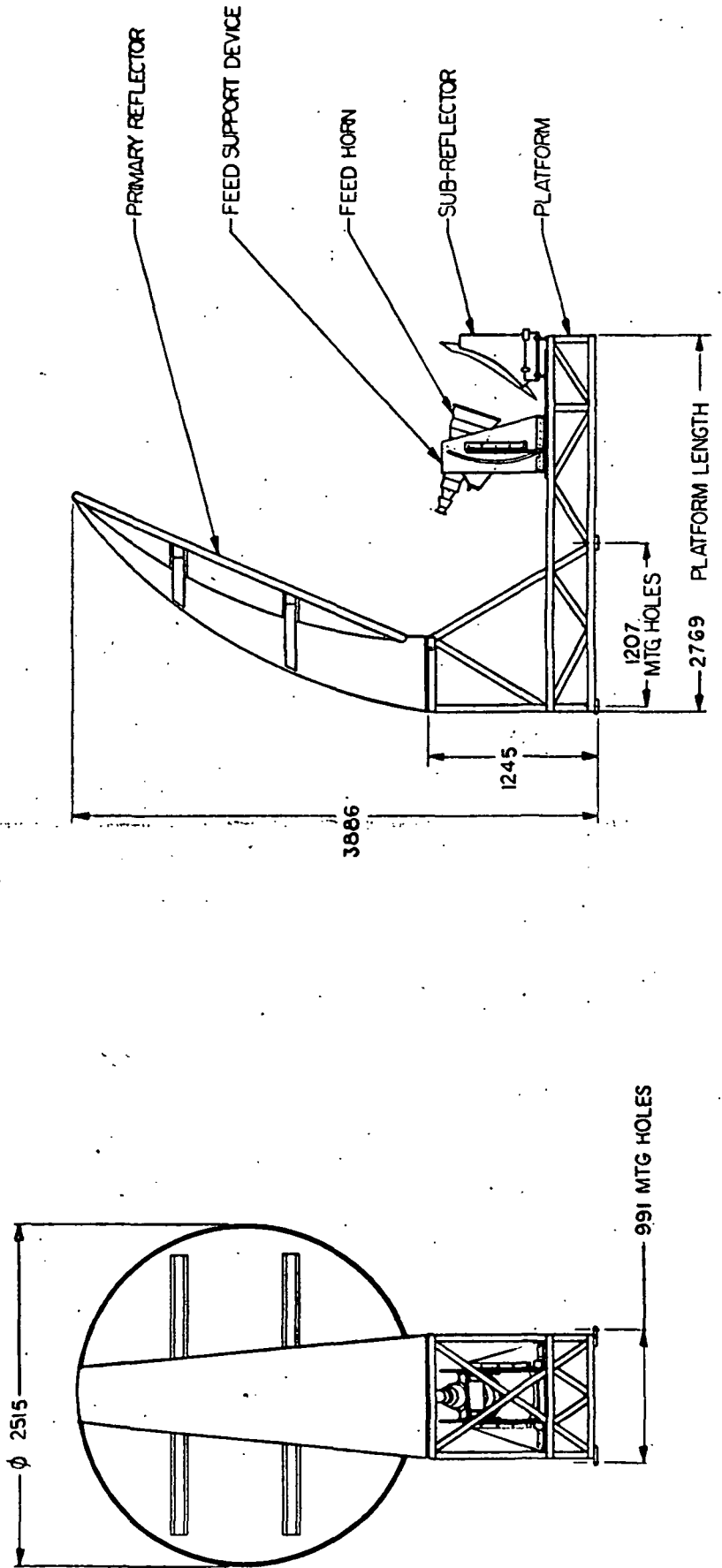
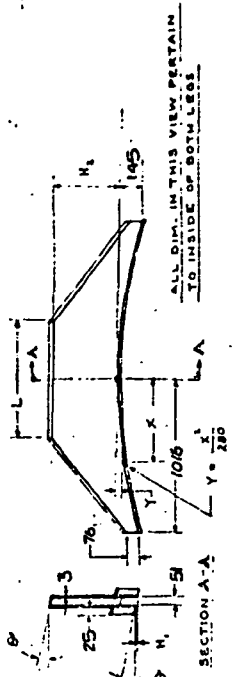
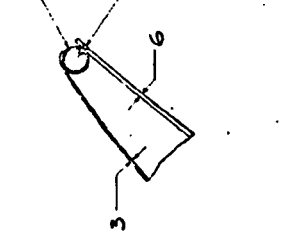


FIG. 4.12

4 3100X 2.0 WALL 2001-T6 ALUM. TUBE  
ROLL INTO  $\phi$  2518 OD RING - WELD ENDS

ALUM. "POP" RIVET  $\phi$  4.0 180° C BUNK. HD.  
USHI CORP. PART NO. AK 6605  
100 RIVETS SPACED APPROX. 76.2



| BEAM  | L   | H  | H <sub>1</sub> | H <sub>2</sub> | C |
|-------|-----|----|----------------|----------------|---|
| UPPER | 610 | 29 | 305            | 29.5           |   |
| LOWER | 762 | 10 | 432            | 18.5           |   |

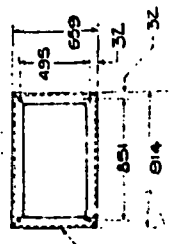
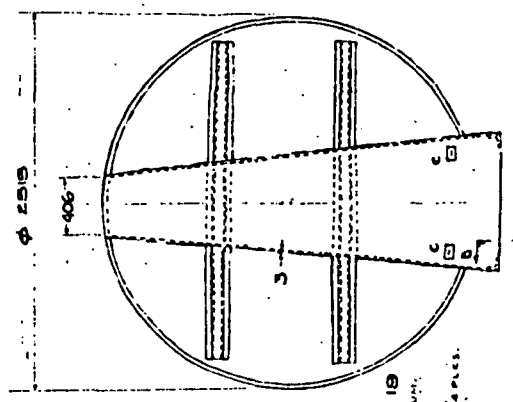
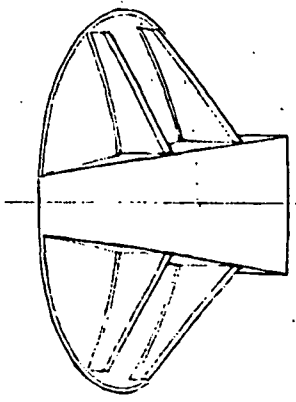
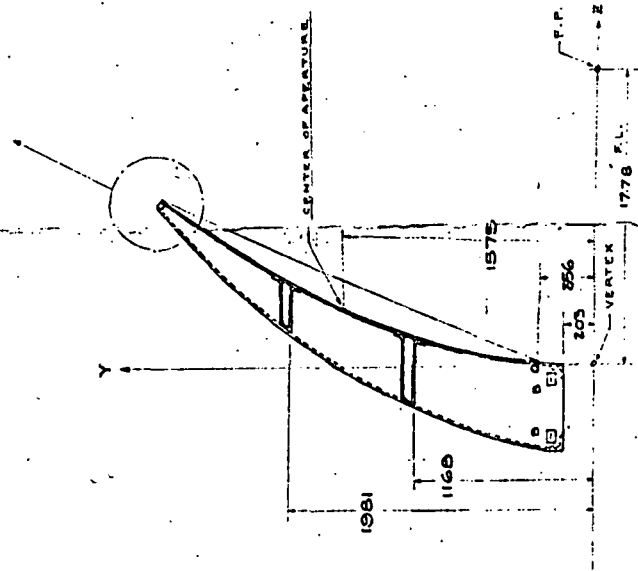
NOTES:

1. REFLECTOR SURFACE TO BE PARABOLOIDAL  $\pm$  .020" RMS.
2. GLASS CLOTH - EPOXY LAMINATE CONSTRUCTION TO BE USED EXCEPT WHERE OTHERWISE NOTED.
3. SECONDARY BONDS TO BE MADE USING EPOXY ADHESIVE.
4. REFLECTIVE SURFACE TO BE RENDERED CONDUCTIVE USING FLAME SPRAYED ALUM.
5. CENTER OF 99" DIA. APERTURE TO BE MARKED ON AN EMBEDDED TARGET THE MARK BEING LOCATED 62.00"  $\pm$  .020 FROM THE FOCAL AXIS. LIKEWISE EMBED 4 OTHER TARGETS NEAR THE RIM OF THE REFLECTOR, 2 ALIGNED ALONG THE Y AXIS, AND 2 ALIGNED ALONG THE X AXIS. PLACE MARKS ON THESE TARGETS THEN MEASURE AND RECORD THE DISTANCE OF THE MARKS FROM THE FOCAL AXIS  $\pm$  .020".

CHU ASSOCIATES INC.  
REFLECTOR ASSY.  
DALLAS, TEXAS

Fig. 4-3

9-10753



76 X 76 X 16 ANER. STD.  
ANGLE - 6061-T6 ALUM.  
41  $\phi$  17 -  
FOR 36-IN. I.D. BEAMS

6. BOND 2" SQ.  $\pm$  1/16" THK. ALUM. PLAQUES MARKED "C" AND "B" IN PLACE APPROX. WHERE SHOWN. SCRIBE LINES MARKED "C" PARALLEL WITH X-X DIRECTION  $\pm$  .005". SCRIBE LINED MARK "B" PARALLEL WITH Z-Z DIRECTION  $\pm$  .005".



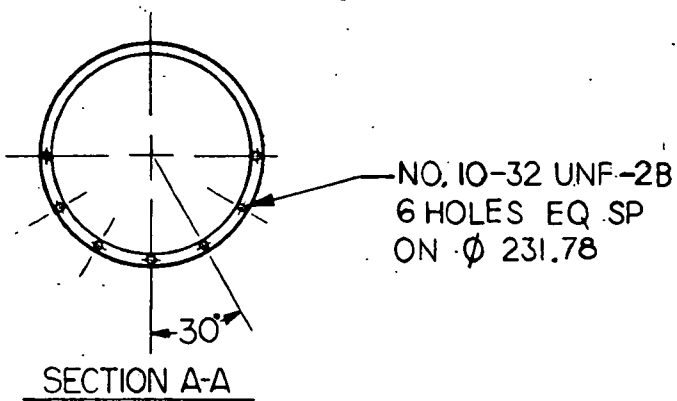
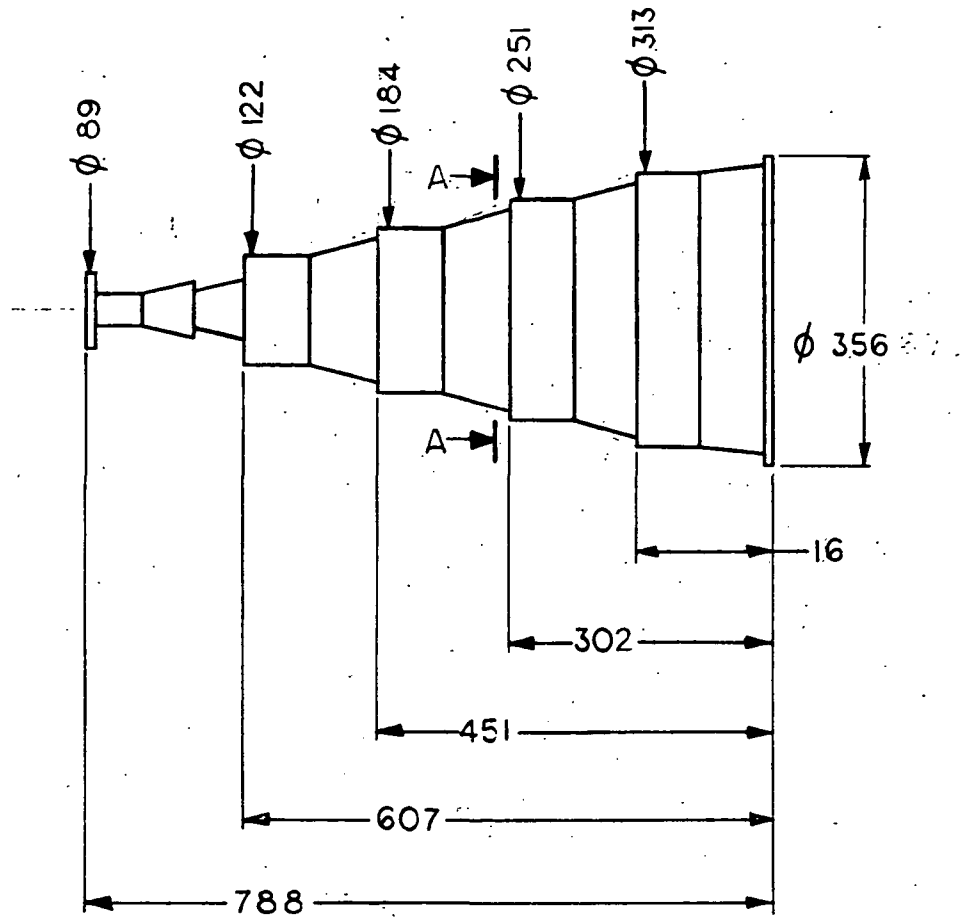


FIG. 4-5

FEED HORN EXTERNAL CONFIGURATION



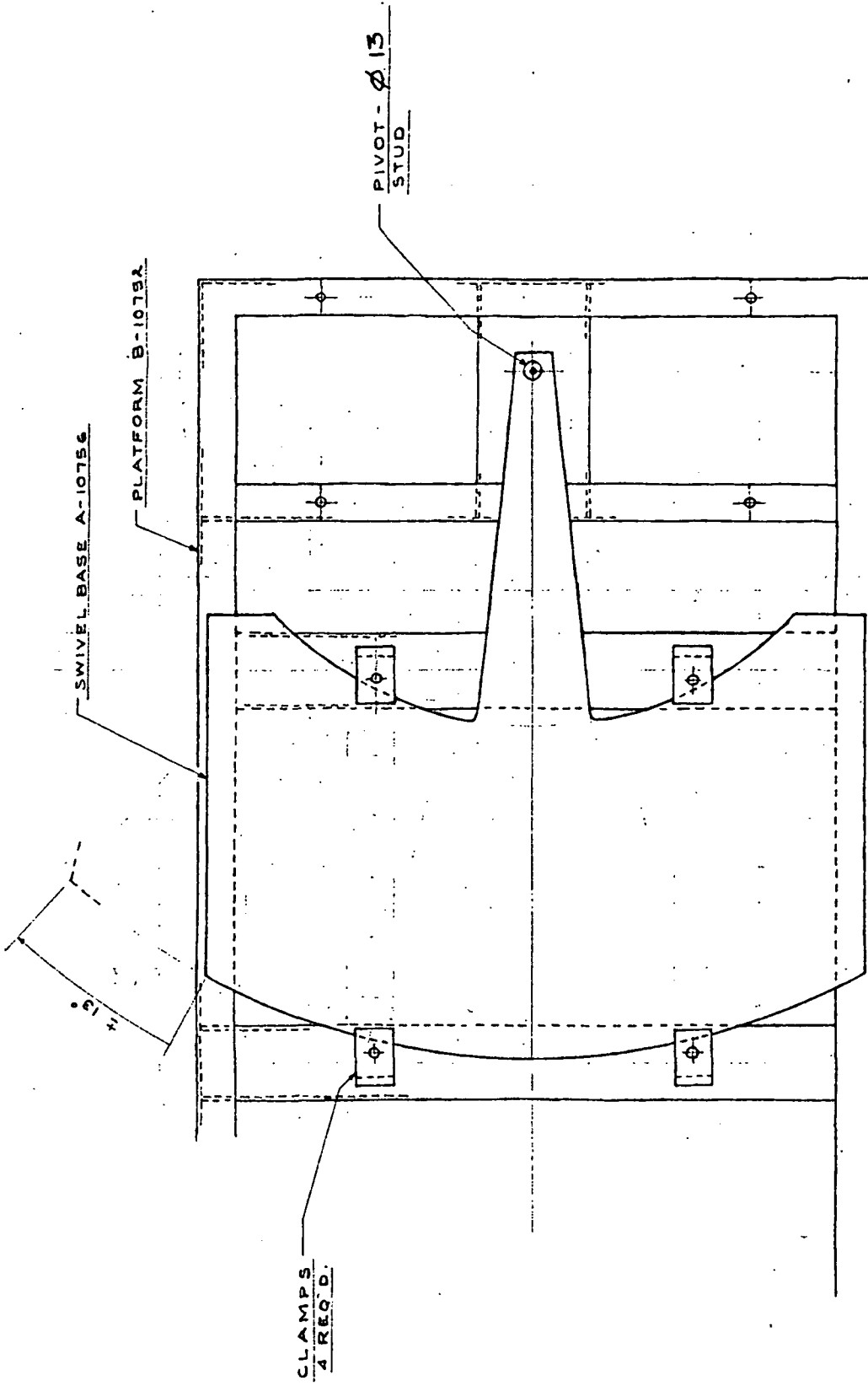
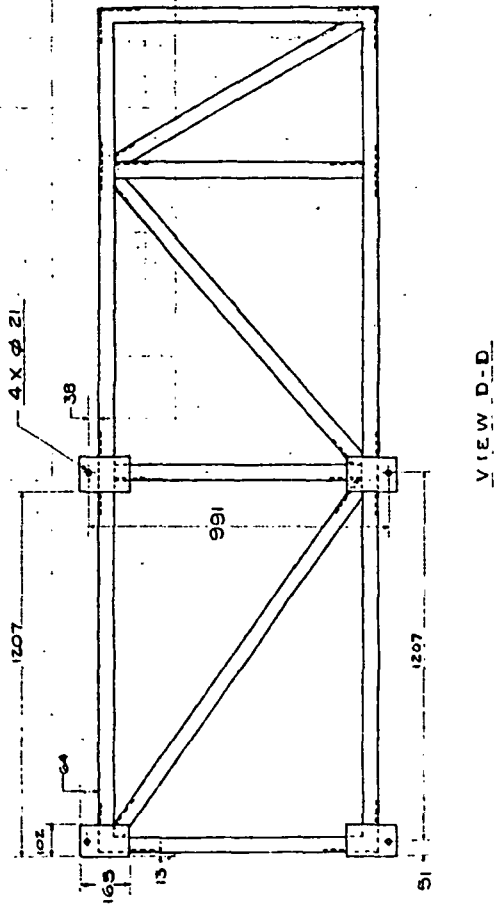
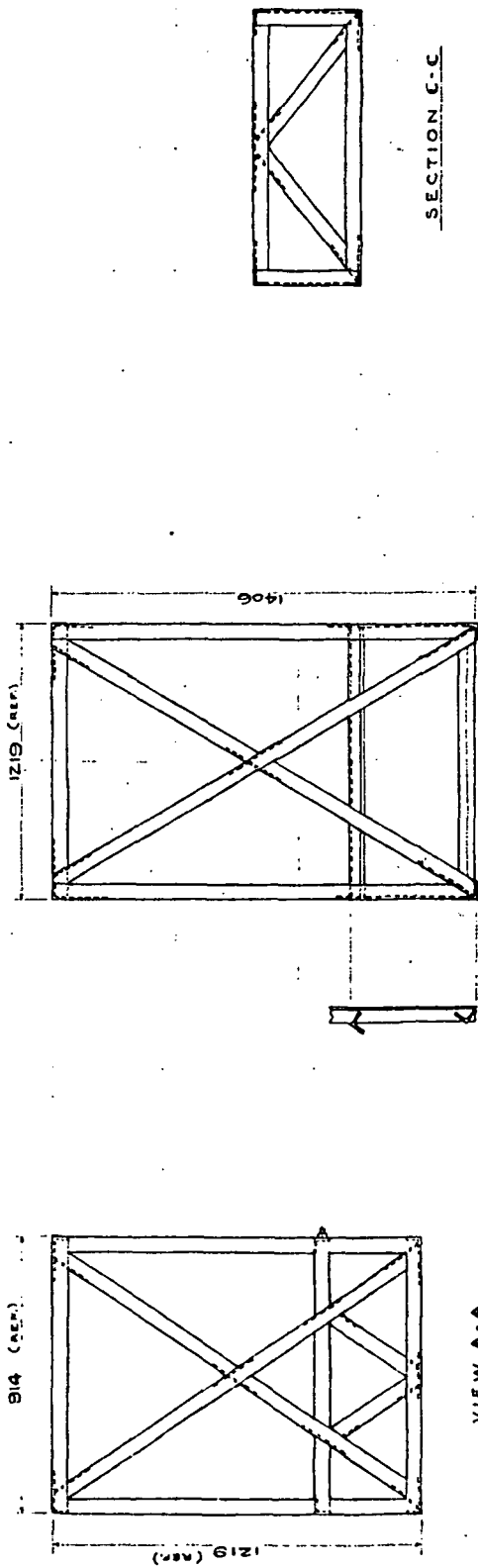
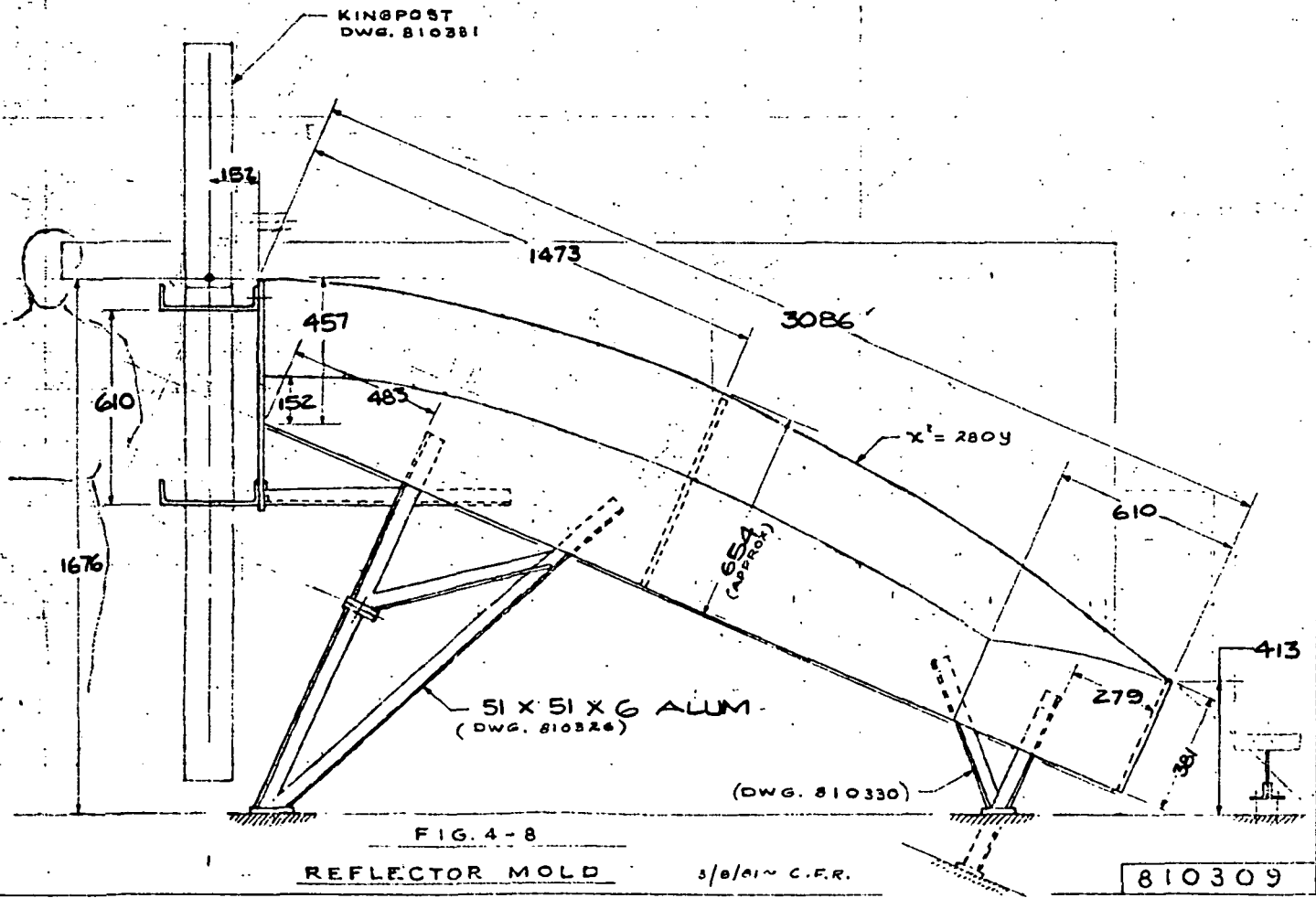
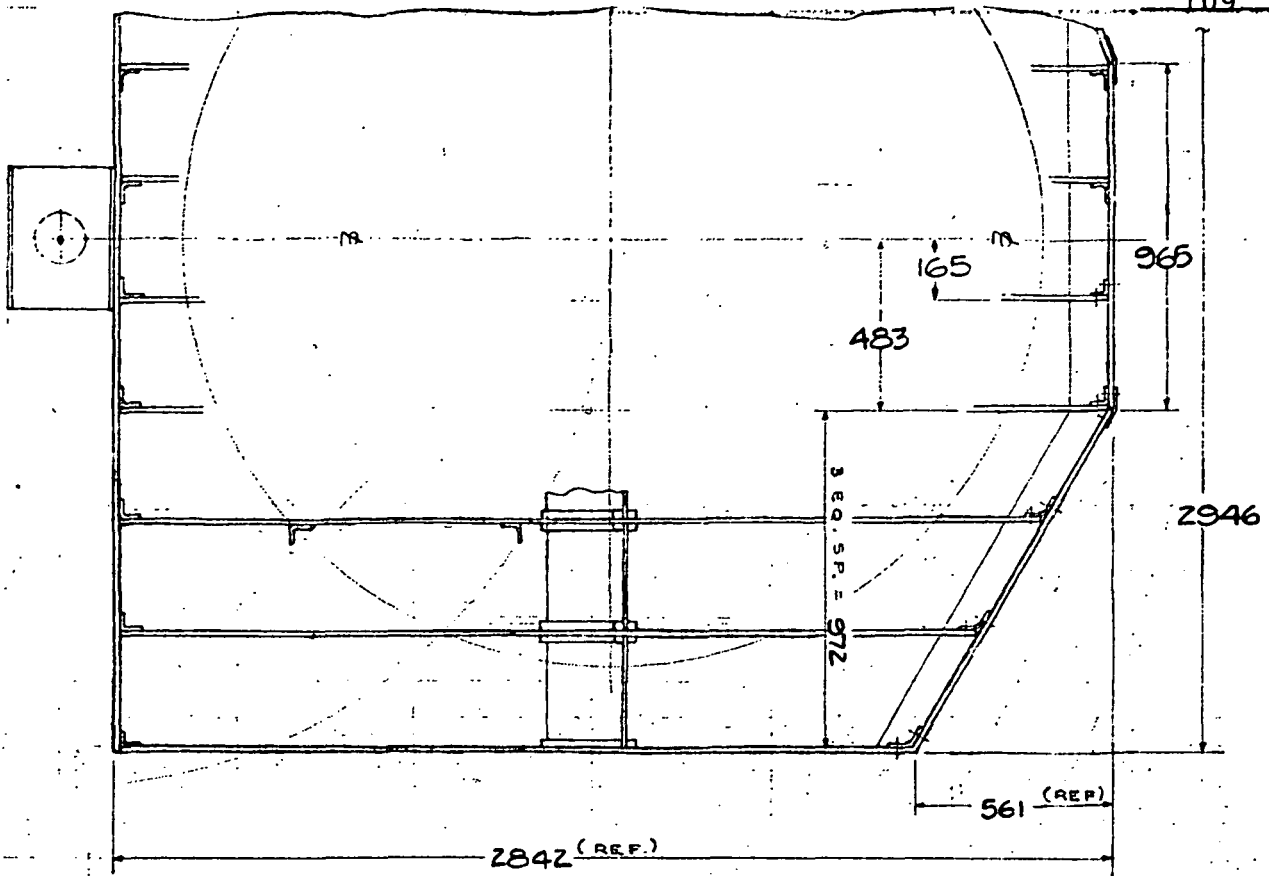


FIG. 4-60.

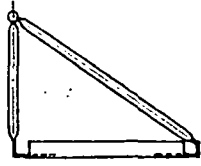
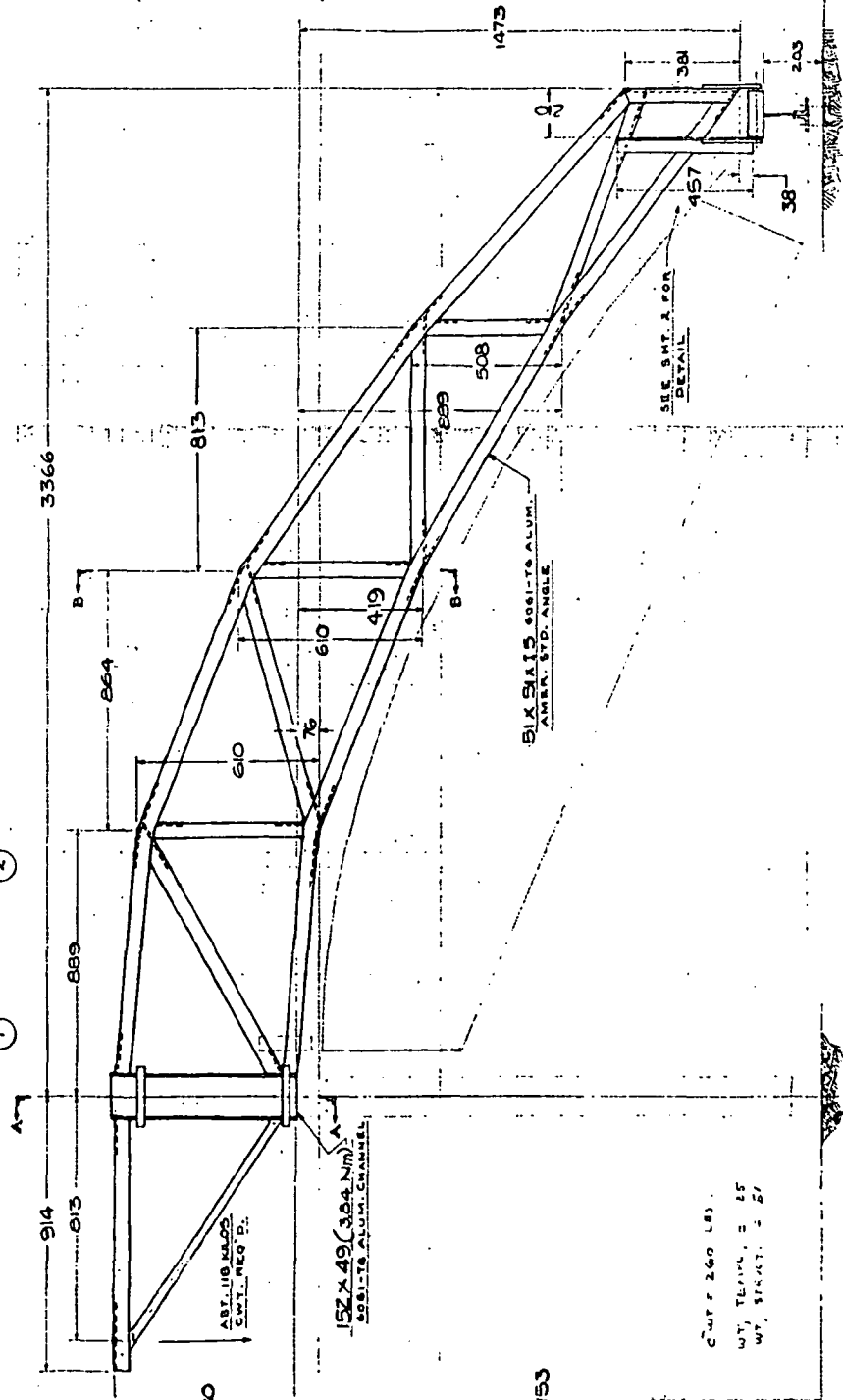
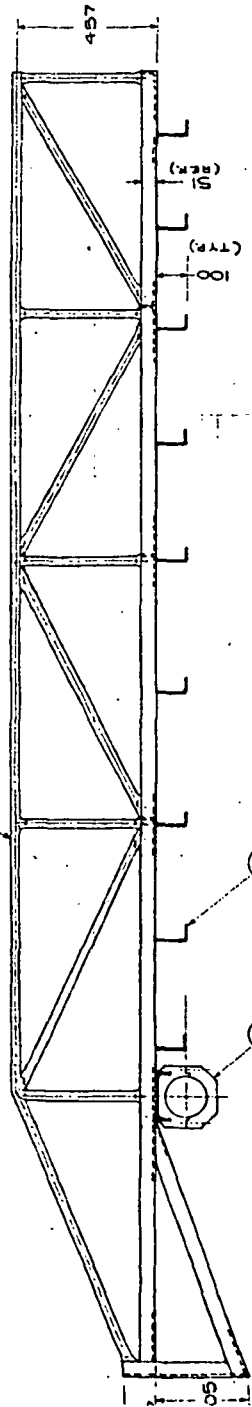


FIG. 4-74

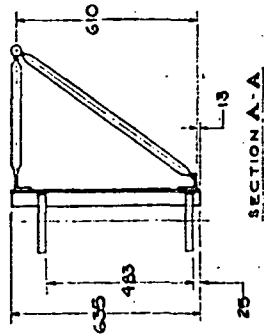




Ø.32 OD X 1.5 WALL  
5081-16 ALUM. TUBING



SECTION B-B  
(TYP. - 4PLCB.)



SECTION A-A

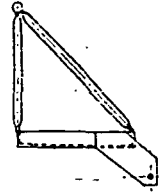


FIG. 4-9a.

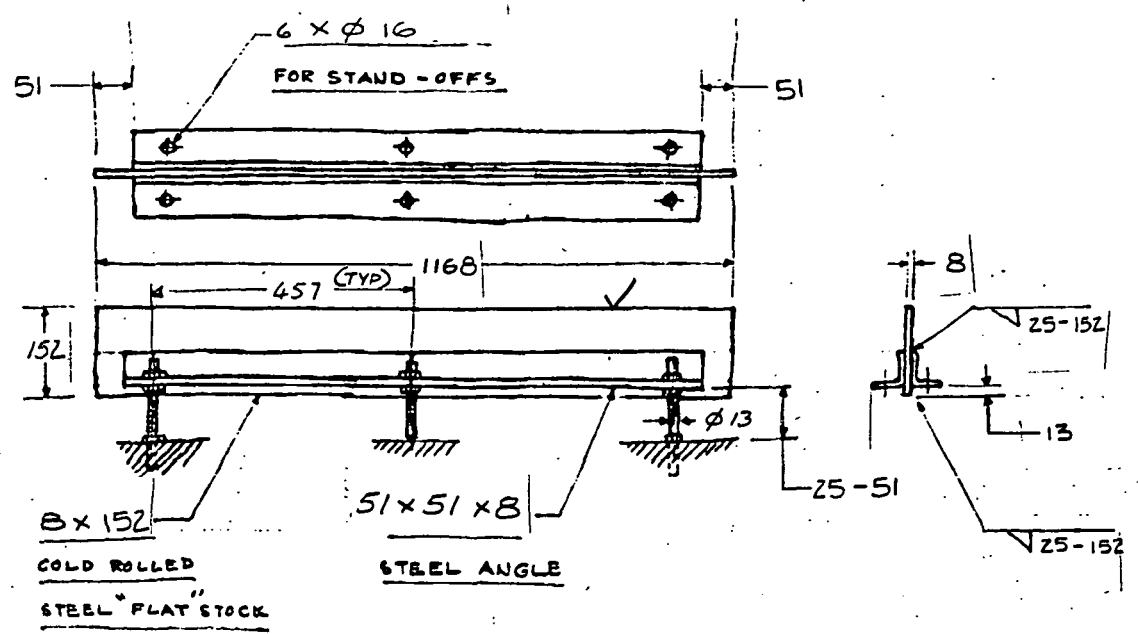
SWEEP ARM

4/19/61 C.P. RICHMAN

81040810

C.W.P. 260 LB.  
WT. TRUSS = 25  
WT. STRUT = 27





NOTES:

- 1.) ORDER 11 PCS. 1676 LG  
8 x 152 COLD ROLLED ST.  
FLATS.
- 2.) ORDER 22 PCS. 51 x 51 x 8  
STL ANGLE
- 3.) NASHUA MACHINE CAN GRIND  
UP TO 1829 ON SURFACE GRINDER.

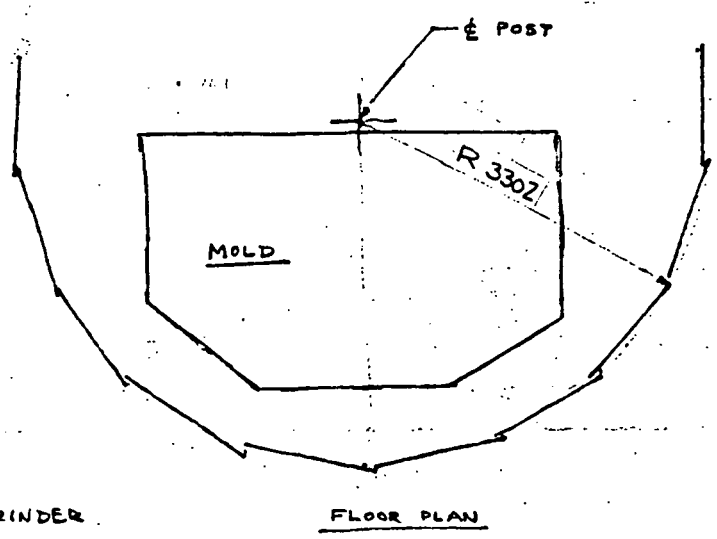
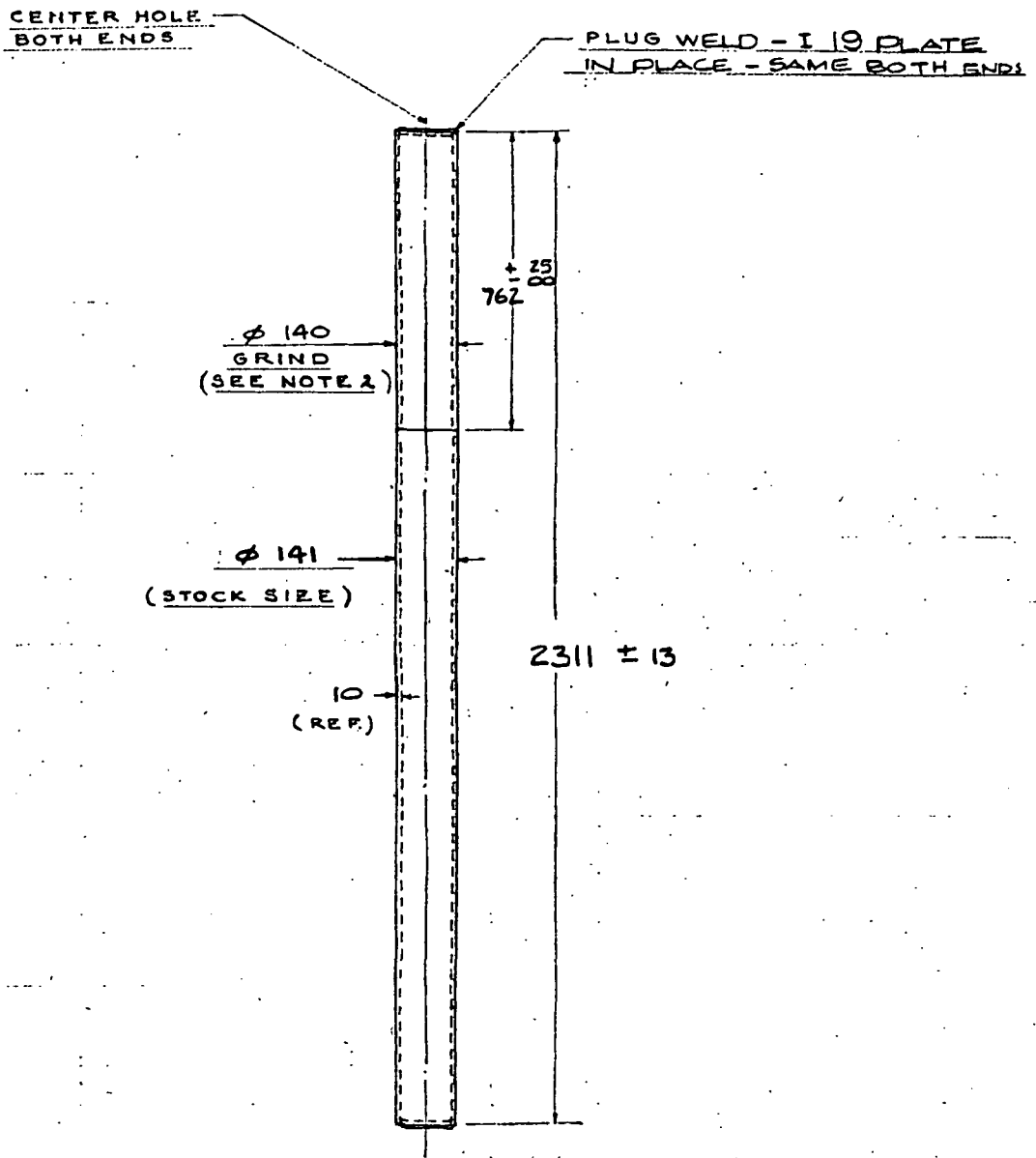


FIG. 4-10  
OUTBOARD SUPPORT  
MOLD - 20C 1271

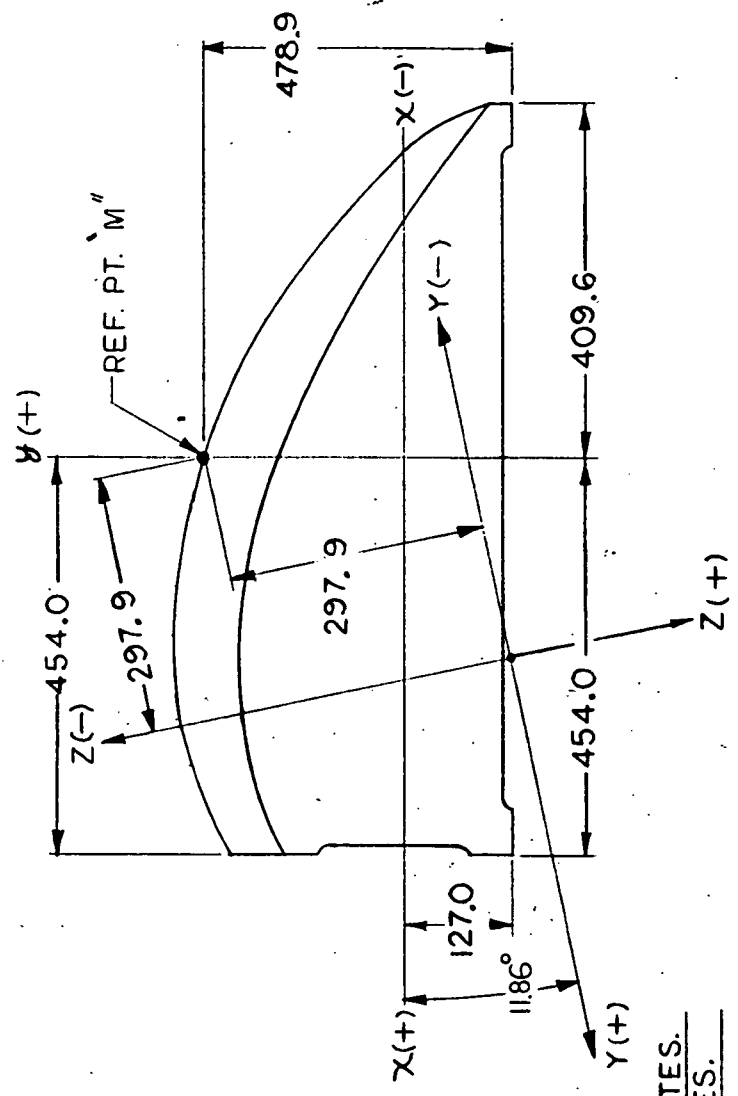
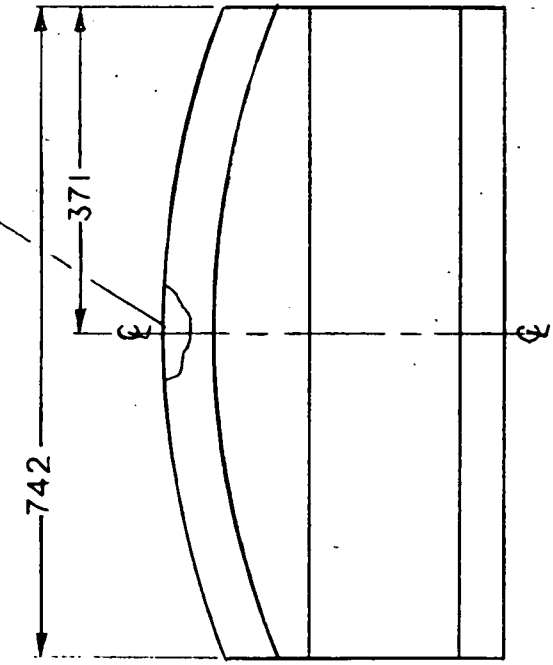
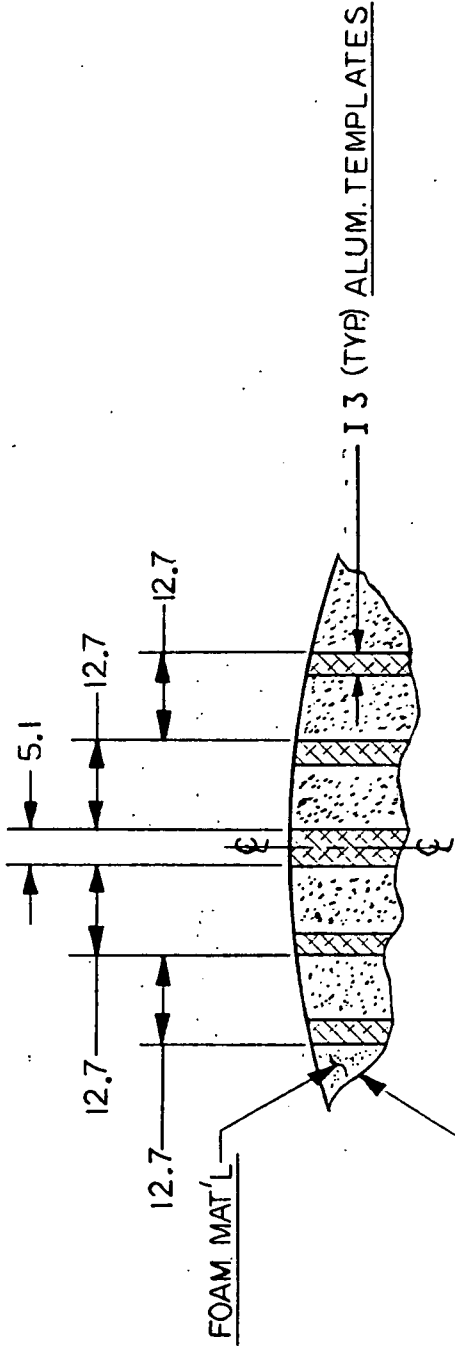


NOTES :

- 1.) MAT'L. 5" SCH. 80 PIPE - A36 STEEL
- 2.) GRIND TO CYLINDRICAL SHAPE - SAME DIA.  
 $\pm .051$  IN 762 LENGTH - DIA. SHOWN IS APPROX.
- 3.) WT. - APPROX. 76 KILOS

FIG. 4-11

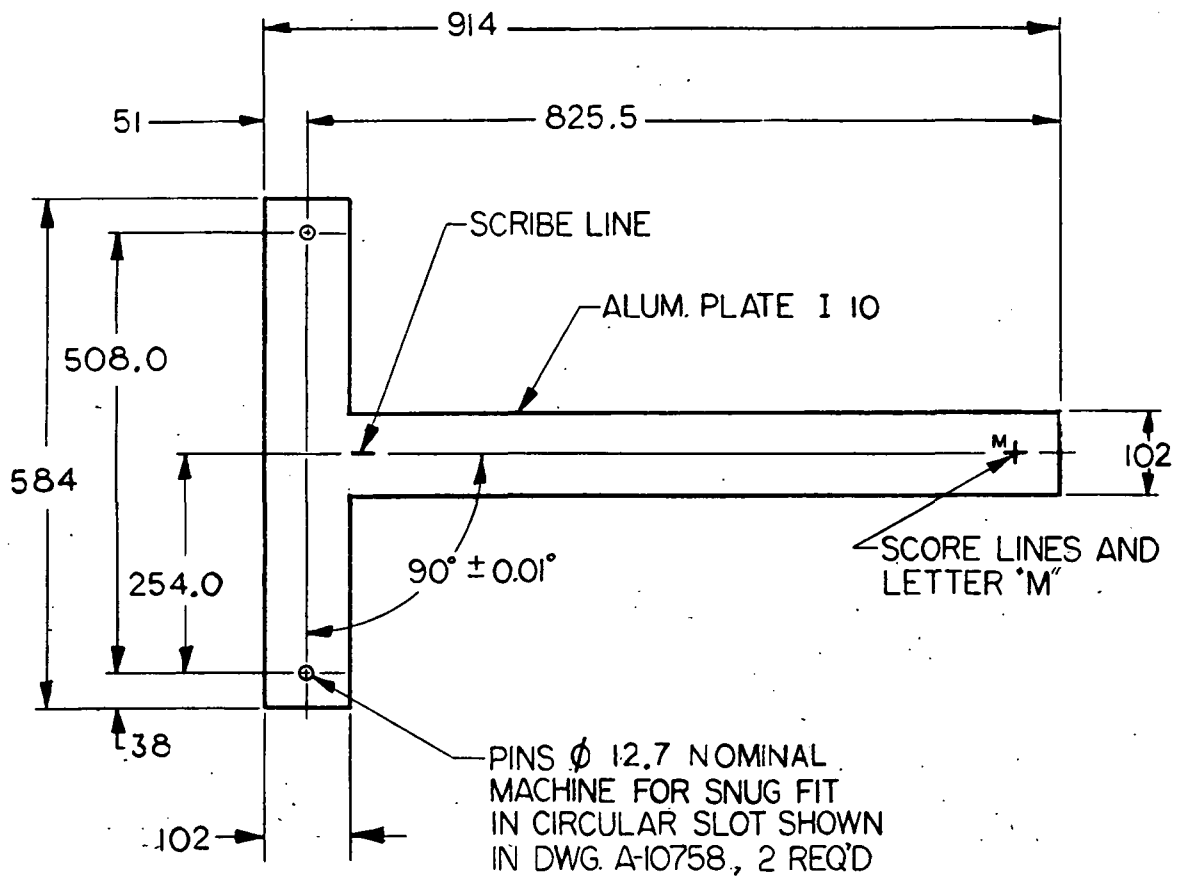
|                         |        |
|-------------------------|--------|
| <u>KINGPOST</u>         |        |
| <u>20C1271 MOLD</u>     |        |
| 5/21/81 - C.F. REICHERT | 810331 |



NOTES

1. X, Y ARE TEMPLATE CUTTING COORDINATES.
2. X, Y, Z ARE GLOBAL SYSTEM COORDINATES.

FIGURE 4-12  
SUB-REFLECTOR MOLD



NOTE: SCRIBE LINES MUST BE SHARP, AND PLACED UNDER GOOD LIGHTING CONDITIONS, USING A JEWELERS LOOP TO ENSURE THE REQUISITE DEGREE OF PRECISION RESULTS

FIG.4-13  
HORN POSITIONING FIXTURE